

Dynamics of driven colloidal systems in one-dimensional potential energy landscapes

Michael P. N. Juniper

Lincoln College
University of Oxford

Supervisor: Dr Roel P. A. Dullens

A thesis submitted for the degree of
Doctor of Philosophy

Hilary Term 2014

Abstract

The dynamics of colloidal particles driven over optical potential energy landscapes is studied. Experiments are conducted using colloids driven by solvent flow or piezo-stage, optical tweezers, magnetic fields, and video-microscopy. Firstly, the properties of optical traps and potential energy landscapes are determined using driven colloidal particles and clusters. The trap stiffness and potential depth of single Gaussian traps are measured directly. It is shown that the nature of optical potential energy landscapes may be fully engineered and predicted using a sum of single Gaussian potentials. Next, the motion of colloidal particles driven by a constant force over a periodic optical potential energy landscape is considered. The average particle velocity is found as a function of the driving velocity, and the wavelength of the optical potential energy landscape, which is found to be sinusoidal at small trap spacings. The critical driving velocity required for a particle to move across the landscape is determined as a function of the wavelength. Brownian motion is found to have a significant effect on the critical driving velocity, but a negligible effect at high driving velocity. Subsequently, the dynamic mode locking caused by adding a modulation to the driving force is studied. This synchronisation manifests as a 'Devil's staircase' in the average particle velocity as a function of driving velocity. The amplitude and frequency dependence of the mode locked steps are studied. Furthermore, particle trajectories are examined, and phase portraits show locked (unlocked) states as closed (open) loops in phase space. A state diagram of mode locked steps is constructed. Finally, driven systems of magnetically interacting colloidal particles are examined in potential energy landscapes. The critical driving velocity of a chain of coupled particles driven by a constant force is found to depend strongly on the chain length and the magnetic field. Secondly, a mobile density wave (kink) in an optically pinned chain of coupled particles is exposed to a constant and modulated drive. The kink is found to behave as a quasi-particle, exhibiting analogous dynamic mode locking behaviour to the single particle case. Finally, the mode locking of a finite mobile chain is considered, and found to be affected by the chain flexibility, which is a function of the magnetic field.

Declaration

This thesis is submitted for the degree of Doctor of Philosophy in Physical and Theoretical Chemistry at the University of Oxford. No part of this thesis has been accepted or is currently being submitted for any degree, diploma, certificate, or other qualification in this University or elsewhere. This thesis is wholly my own work, except where indicated.

Contents

Abstract **i**

Declaration **iii**

1 Introduction **1**

1.1 Colloids 2

1.2 Optical trapping 3

1.3 Scope of this thesis 4

2 Theoretical background and experimental methods **7**

2.1 The Langevin equation 8

2.1.1 Driving Brownian particles 10

2.1.2 Driving 'forces' 11

2.2 Colloidal model systems 12

2.2.1 Characteristic quantities 12

2.2.2 Colloidal interactions 13

2.2.3 Super-paramagnetic colloids 14

2.3 Optical trapping 16

2.3.1 Acousto-optical deflectors 18

2.4 Experimental methods 19

2.4.1 Colloidal model system 19

2.4.2 Sample cells 20
2.4.3 Optical trapping setup 20
2.4.4 Inverted bright field microscope 23
2.4.5 Driving colloidal particles 26
2.4.6 Magnetic fields 27
2.4.7 Software 28

3 Mapping optical potentials using driven colloidal particles 31

3.1 Introduction 32
3.2 Theory 33
3.2.1 Dynamics of particles driven over optical traps 33
3.3 Experimental methods 34
3.3.1 Colloidal model system 34
3.3.2 Experimental setup 35
3.3.3 Equilibrium trap measurements 35
3.3.4 Flow experiments 35
3.3.5 Piezo-driven experiments 35
3.4 Results and discussion 36
3.4.1 Flow experiments 36
3.4.2 Piezo-driven experiments 40
3.5 Conclusions 46

4 Colloidal particles driven across periodic optical potential energy landscapes 47

4.1 Introduction 48
4.2 Theory 49
4.2.1 Sinusoidal landscape: small trap spacing 51
4.2.2 Nearest neighbour landscape: large trap spacing 53
4.2.3 Comparing the approximations 54

4.2.4 The effect of Brownian noise . . . 55
4.3 Experimental methods . . . 56
4.3.1 Colloidal model system . . . 56
4.3.2 Experimental setup and parameters . . . 56
4.3.3 Average velocity experiments . . . 57
4.3.4 Critical velocity experiments . . . 57
4.4 Results and discussion . . . 58
4.4.1 Average particle velocity . . . 58
4.4.2 Critical driving velocity . . . 62
4.4.3 Driving velocity far above the critical driving velocity . . . 63
4.5 Conclusions . . . 64

5 Dynamic mode locking in a driven colloidal system 67

5.1 Introduction . . . 68
5.2 Theory . . . 69
5.2.1 The 'high frequency' regime . . . 70
5.3 Experimental methods . . . 73
5.3.1 Colloidal model system . . . 73
5.3.2 Experimental setup and parameters . . . 73
5.3.3 Average velocity experiments . . . 74
5.3.4 Critical velocity experiments . . . 74
5.4 Results and discussion . . . 76
5.4.1 The 'Devil's staircase' . . . 76
5.4.2 Trajectories and phase portraits . . . 77
5.4.3 Frequency dependence . . . 79
5.4.4 Amplitude dependence . . . 83
5.5 Conclusions . . . 91

6 Coupled colloidal particles driven over periodic optical potential energy landscapes 93

6.1 Introduction 94

6.2 Theory 96

6.3 Experimental methods 98

6.3.1 Colloidal model system 98

6.3.2 Experimental setup 99

6.3.3 Critical velocity experiments 100

6.3.4 Average velocity experiments 100

6.4 Results and discussion 103

6.4.1 Critical velocity of coupled particles driven by a constant velocity 103

6.4.2 Dynamic mode locking of a kink in a static chain 107

6.4.3 Dynamic mode locking of a finite mobile chain 113

6.5 Conclusions 118

Bibliography 120

Publications 135

Acknowledgements 138

Chapter 1

Introduction

In the natural world, little exists in a state of true equilibrium; in fact, most of the physics around us is far from equilibrium [1]. Many materials, such as plastics and glasses, are dynamically arrested [2], equilibrating on time scales longer than the age of the universe. Other systems exist in a constantly evolving but balanced state. Orbiting satellites in constant free-fall, developing weather patterns, and the entropic balance of life, all demonstrate such dynamic processes far from equilibrium [1].

On both macroscopic and microscopic levels, driven systems exhibit behaviour well beyond their equilibrium properties. Therefore the presence of an external drive is vitally important to a diverse range of natural and technological processes, on length and time scales ranging from the tectonic to the electronic, through glacial drift, homoeostasis, and crack propagation [3]. Common to all of these examples is the delicate balance between the external drive and the 'internal' equilibrium behaviour opposing the drive, which leads to the rich and complex dynamical behaviour of driven non-equilibrium systems [1].

In many far from equilibrium phenomena the existence of potential energy landscapes plays a central role. Kinetic friction results from a very literal interpretation of this: the pinning and sliding of a pair of surfaces in contact and driven by opposing lateral forces, depends on the their roughness [4]. On a much smaller scale, charge density waves in layered metallic crystals move charge carried by delocalised electrons through the periodic electrostatic potential energy landscape of the atomic lattice [5]. Another classical example is the motion of vortex lines in type-II superconductors. In this case, chains of interacting vortices move through channels

composed of pinned vortices, which form a static undulating potential energy landscape [6].

The motion of systems driven over potential energy landscapes is an example of non-linear dynamics, which simply means that the output of the system does not depend linearly on the input [7]. One of the most basic examples of a non-linear model is a pendulum, which illustrates both the simplicity and the universality of non-linear dynamics [8]. The equation of motion describing the time evolution of a simple pendulum is a non-linear differential equation. Despite its relative simplicity, this equation of motion is of a form that is found in many other seemingly unrelated systems, such as Josephson junctions, charge density waves, and solitons [8], and indeed Brownian particles on periodic potentials. The non-linearity of Brownian particles driven over a periodic potential manifests in the form of a non-linear relationship between the applied driving force and the average velocity of the particle. By driving the particle far away from equilibrium, an exciting range of non-linear dynamic phenomena may be explored.

1.1 Colloids

In this thesis, a non-linear dynamic system is constructed by driving colloidal particles over an optical potential energy landscape. The versatility of colloidal systems has been crucial to their success as one of the most powerful physical model systems of the past century [9]. With length scales from nanometers (1 nm $\equiv$ 10^{-9} m) to several micrometers (1 μm $\equiv$ 10^{-6} m), colloidal particles are large enough to be easily observed by optical microscopy techniques, making their real-space properties directly accessible [10–12]. Furthermore, the shape of colloidal particles may vary from spheres to high-aspect-ratio rods [13], through anisotropy ranging from dimples [14,15] and bowls [16] to cubes [17], bullets [18], and even dandelion-shaped particles [19]. Colloidal particles are made from a range of materials such as the commonly used silica, or various plastics [20], but their origins may also be metallic, inorganic, or biological.

One of the key properties of colloidal dispersions is the irregular agitation of their particles as they come under constant random bombardment from the solvent molecules, which is commonly known as Brownian motion. When Perrin accepted the Nobel Prize for Physics in 1926, he described Brownian motion as a *'permanent system of a perfectly irregular agitation'* [10]. Despite Robert Brown's extensive description of the (now eponymously named) *'vivid'* motion of particles in a colloidal suspension, he was unable to provide an explanation for the

effect [21]. Einstein and Smoluchowski formalised the theoretical basis, with their work being experimentally tested by Perrin [10]. Right from the beginnings of colloidal science, its potential to address fundamental questions in physics has been recognised. By the time of Perrin's Nobel Prize in 1926, he had already used colloids to prove the existence of molecules, and estimate the Avogadro number [22]. Indeed the thermal fluctuations make colloids sample phase space similarly to molecular and atomic systems, which makes them attractive as large 'model atoms', exhibiting similar phase behaviour [23, 24].

Colloidal systems are not only simple to observe, they are also easy to manipulate, a property that will be exploited in this thesis. Colloidal particles may be manipulated by electric and/or magnetic fields, shear and flow, optical fields, the imposition of confinement, and even the addition of active components [25]. In this thesis, the handles used are optical, magnetic, and flow fields. The tunability of colloidal particles is crucial for these applications as the efficacy of optical trapping depends on a difference in refractive index between the particles and the solvent, and their manipulation by magnetic fields requires some magnetic material to be incorporated within the particles.

1.2 Optical trapping

The potential energy landscapes used in this work are produced using optical tweezers, which use a focused beam of laser light to manipulate matter [26]. The pioneering work of Arthur Ashkin introduced the concept of using light to manipulate micron-sized particles with a refractive index higher than their solvent, which are drawn to the highest intensity part of a laser beam [27, 28]. He demonstrated that not only could particles be driven by the radiation pressure ('photophoresis'), they could also be trapped, by using a pair of counter-propagating laser beams, or by using gravity to oppose the scattering force of the beam. Since this seminal work, optical trapping has been used to trap matter from atoms to biological cells [29].

The possibilities for producing optical potential energy landscapes using optical tweezers are enhanced by using fast beam steering devices. The basic beam steering option is a pair of mirrors, which enable the beam to be directed in a two-dimensional plane. This option may be improved by using a pair of fast galvano-scanning mirrors, allowing a few laser spots to be scanned at up to hundreds of Hertz [30]. A high scanning speed is crucial - for the colloidal

particles to experience a continuous optical potential energy landscape, rather than discrete spots which switch positions, the different positions must be scanned considerably faster than the time taken for the particles to diffuse over a significant distance (for example the particles used in this work diffuse 1% of their diameter in $\sim \frac{1}{50}$ s). A second two-dimensional beam steering option is to pass the beam through a pair of acousto-optical deflectors (AODs) [31], which diffract the light using a tunable 'grating' formed by a standing wave in a crystal. AODs are much faster than scanning mirrors, and are able to time-share trap positions at up to hundreds of *kilo*Hertz, but only transmit up to 60% of the laser light. Extending multi-trap beam steering to three dimensions requires the use of a spatial light modulator (SLM) [32–34]. This is placed in the beam path like a mirror, and uses a high-resolution liquid crystal display to impose a hologram onto the wave front of the laser beam. Beam shaping in this manner may be used to create a wide diversity of trapping geometries. Another method for creating extended two-dimensional arrays of optical traps is to use interfering beams. This technique has been used to make square, hexagonal, and even quasi-periodic arrays [35].

One of the areas where optical trapping has found many applications is in colloid science [36–41]. Applications have included probing the phase behaviour of colloidal monolayers [35,42–46], micro-rheology [47,48], and particle sorting [49–54]. Optical tweezers have also been utilised to measure the strength of magnetic chains [55], cool and heat micro-spheres [56,57], and even to actuate a surface scanning probe [58]. Other recent developments include using a circularly polarised beam to rotate shaped particles [19], and the production of random potential energy landscapes using noise [59,60].

1.3 Scope of this thesis

In this thesis, the dynamic behaviour of colloidal particles, driven in one-dimensional optical potential energy landscapes, is investigated. The dense particles used are natively confined into a quasi-two-dimensional state by gravity, and the optical potential energy landscape further restricts the particles to quasi-one-dimensional trajectories. Studying this simple system offers the dual benefits of increased resolution in both control parameters and observation, yet the system exhibits complex dynamical behaviour. In the following chapters, the complexity of the driven system is built up in stages, from single particles driven by a constant force through

single optical traps, to clusters of interacting particles driven by a modulated driving velocity over periodic optical potential energy landscapes.

The theoretical and experimental background behind the described work is introduced in Chapter 2. The Langevin equation is used to describe the motion of a Brownian colloidal particle driven by external forces over an optical potential energy landscape. The principles of the colloidal model system and the imposed optical and magnetic fields are then laid out, and the optical apparatus and imaging methods are described and illustrated.

Having established the theoretical and technical basis for optical trapping, Chapter 3 describes the mapping of the optical potential energy landscapes using driven colloidal particles. As this thesis considers the dynamics of strongly driven colloidal particles, it is important to fully characterise the optical traps, beyond the harmonic part of the potential. To this end, the colloidal system is driven using two methods - solvent flow drive and piezo stage drive. Single optical traps and extended optical potential energy landscapes are fully mapped using both individual colloidal particles and small rigid clusters of particles.

Using the now well characterised one-dimensional periodic optical potential energy landscape as a basis, Chapter 4 considers the dynamics of colloidal particles driven over such a landscape. The non-linear dependence of the average particle velocity on the driving velocity is studied. The transition from a pinned to a sliding state at the critical driving velocity is examined in detail, and the particle velocity far from the critical driving velocity is probed. The results found are compared to theoretical predictions.

Next, the so far constant driving force is supplemented by a modulated driving force, and the dynamics of driven particles in a sinusoidal optical potential energy landscape are studied (Chapter 5). A synchronisation effect known as 'dynamic mode locking', which results from the coupling between the natural oscillation of the particle velocity, due to the influence of the optical potential energy landscape, and the modulation of the driving velocity, is studied. The amplitude and frequency dependence of the mode locked steps is described in detail. The strong non-linearities found in the average velocity are linked to the microscopic dynamics, using particle trajectories and phase portraits.

Finally, in Chapter 6, the non-linear dynamics of systems of multiple interacting particles are considered. Linear clusters of super-paramagnetic particles are created, using homogeneous

in-plane magnetic fields to induce attractive dipolar interactions. Three experiments are performed exploring different regions of the now vast parameter space. Firstly, the critical driving velocity of weakly pinned chains of particles is studied as a function of the size of the chains, the strength of the inter-particle interactions, and the wavelength of the optical potential energy landscape. Subsequently, a chain of weakly coupled, but strongly optically pinned, particles is studied. A single isolated topological defect is introduced into the chain, which manifests as a local increase in density. This 'kink', when driven, moves through the chain as a density wave, and acts as a quasi-particle exhibiting dynamic mode locking. The final situation examined is the motion of a coupled chain driven past periodic optical potential energy landscapes. The effect of chain flexibility on dynamic mode locking in this coupled system is studied.

Chapter 2

Theoretical background and experimental methods

Abstract

This thesis studies the dynamics of colloidal particles driven over optical potential energy landscapes. In this chapter the theoretical background for the experimental work in this thesis is laid out, and the experimental methods are described. Firstly, a Langevin equation is written for the motion of colloidal particles driven over an optical potential energy landscape, with constant and modulated force. Then colloidal model systems and their interactions are introduced, in particular the dipole-dipole attractions present between super-paramagnetic particles in a magnetic field. Next, the theoretical basis of optical trapping is discussed, and the construction of the experimental setup consisting of two-dimensional time-shared optical tweezers and an inverted bright field microscope is described. Finally, the computer software used to control the setup, perform experiments, and record particle positions is discussed.

2.1 The Langevin equation

The most general way to describe the motion of a particle of mass m moving under the influence of the sum of all external forces, $\Sigma\mathbf{F}$, is Newton's Second Law of Motion, $\Sigma\mathbf{F} = m\mathbf{a}$, where $\mathbf{a}$ is the particle's acceleration. This thesis deals with a system of Brownian colloidal particles dispersed in a solvent, where the constant random bombardment of the particle by solvent molecules leads to a fluctuating force, $\xi(t)$. The inclusion of this stochastic force term in Newton's Second Law of Motion leads to a so-called Langevin equation, which describes the motion of a Brownian particle:

$$m\frac{\mathrm{d}^2\mathbf{r}}{\mathrm{d}t^2} = \xi(t) - \zeta\frac{\mathrm{d}\mathbf{r}}{\mathrm{d}t}, \tag{2.1}$$

where $\mathbf{r}$ is particle position, t is time, and ζ is the friction coefficient. The first term, $m\frac{\mathrm{d}^2\mathbf{r}}{\mathrm{d}t^2}$, includes all of the inertial forces, and the final term, $\zeta\frac{\mathrm{d}\mathbf{r}}{\mathrm{d}t}$, accounts for the viscous forces due to the particle moving through the solvent, which are proportional to the particle velocity, $\frac{\mathrm{d}\mathbf{r}}{\mathrm{d}t}$.

It is pertinent at this juncture to note that the validity of the Langevin equation depends on the assumption of the separation of time scales between the relaxation time of the molecular solvent ($\sim 10^{-14}$ s) and the relaxation time of the much larger Brownian particles ($\sim 10^{-9}$ s) [61]. In this case, it may be assumed that Brownian noise is *delta correlated*; that is the separation of time scales means that it has no memory [40, 62], such that:

$$\langle\xi(t)\xi(t')\rangle = 2\zeta k_\mathrm{B}T\ \delta(t-t'), \tag{2.2}$$

where k_B is Boltzmann's constant, T is temperature, and $\delta(t-t')$ is a Dirac delta function. On the time scale of the motion of solvent molecules this would not be true, but as the relaxation time of the relatively massive Brownian particles is $\sim 10^5$ times longer, there is no correlation in the noise term. In this case, $\xi(t)$ is assumed to be Gaussian white noise, such that $\langle\xi(t)\rangle = 0$.

Now the viscous force term, $\zeta\frac{\mathrm{d}\mathbf{r}}{\mathrm{d}t}$, in equation 2.1 is considered. According to Stokes' law, the friction coefficient for a sphere of radius a translating in a fluid of dynamic viscosity η is: $\zeta_\mathrm{Stokes} = 6\pi\eta a$ [9]. It is clear from experiment, however, that this expression is not valid when particles are close to a wall, where higher friction is observed [63]. This can be accounted for by using the correction due to Faxén [64], which states that the friction coefficient of a sphere

translating in the vicinity of a plane wall can be described by:

$$\zeta = \frac{\zeta_{\text{Stokes}}}{1 - \frac{9}{16}\left(\frac{s}{a}\right) + \frac{1}{8}\left(\frac{s}{a}\right)^3 - \frac{45}{256}\left(\frac{s}{a}\right)^4 - \frac{1}{16}\left(\frac{s}{a}\right)^5}, \tag{2.3}$$

where s is the distance between the particle and the wall. This solution has been confirmed to two orders in experiment [65]. It is, however, also possible to experimentally determine the friction coefficient directly from the particle trajectories, by determining the two-dimensional mean squared displacement, $\langle r(t)^2 \rangle = 4Dt$, where $D = k_{\text{B}}T/\zeta$ is the diffusion coefficient.

Finally, the inertial term in equation 2.1, $m\frac{\mathrm{d}^2\mathbf{r}}{\mathrm{d}t^2}$ is considered. In many experimental systems, particularly on the colloidal length-scale, this term may be neglected. The relevance of the inertial term is quantified using the Reynolds' number, which is the ratio between the inertial contribution due to the density of the solvent, $\rho v^2/a$, and the viscous contribution due to the viscosity of the solvent, $\eta v/a^2$ [22]:

$$\text{Re} = \frac{\left(\rho\frac{v^2}{a}\right)}{\left(\eta\frac{v}{a^2}\right)} = \rho\frac{va}{\eta}. \tag{2.4}$$

In this formulation, both contributions act per volume displaced. For a system of colloidal particles of radius $a \approx 1.5$ μm moving at a velocity of $v \approx 10$ μm s^{-1} in a solvent of density $\rho \approx 1 \times 10^3$ kg m^{-3} and dynamic viscosity of $\eta \approx 1.5 \times 10^{-3}$ Pa s, the Reynolds' number is on the order of $\text{Re} \approx 1 \times 10^{-5}$. This means that such a system is always at very low Reynolds' number, implying that viscous forces are much greater than inertial forces, which may be neglected. In other words, the particle's motion is over-damped, and the solvent is at equilibrium, so that equation 2.1 may be simplified as:

$$\zeta\frac{\mathrm{d}\mathbf{r}}{\mathrm{d}t} = \xi(t), \tag{2.5}$$

which is the equation of motion for a Brownian particle in suspension.

2.1.1 Driving Brownian particles

During the experiments in this thesis, particles are driven in one dimension. Therefore, vector notation will be dropped, and scalar notation will be adopted; the particle position will be denoted by x, such that $\mathbf{r} = x\,\hat{\mathbf{r}}$, where $\hat{\mathbf{r}}$ is the unit vector pointing along the direction of drive. Positive values of the velocity, $v = \frac{\mathrm{d}x}{\mathrm{d}t}$ therefore correspond to particle motion in the same direction as the driving force, and negative values correspond to motion counter to the driving force. In order to account for the effects of external forces, such as an imposed drive, on the motion, the Langevin equation in the over-damped limit (equation 2.5) is expanded to include a deterministic force term, $F(x,t)$:

$$\zeta\frac{\mathrm{d}x}{\mathrm{d}t} = F(x,t) + \xi(t). \tag{2.6}$$

The deterministic force may be composed of multiple contributions, which in this thesis will consist of a position dependent force due to a spatial optical trapping potential, $F_{\mathrm{T}}(x)$, a constant force, F_{DC}, and a time dependent modulated force, $F_{\mathrm{mod}}(t)$. This modulated force has an amplitude of F_{AC} and an angular frequency of $\omega = 2\pi\nu$, where ν is the applied driving frequency:

$$F_{\mathrm{mod}}(t) = F_{\mathrm{AC}}\cos(\omega t) \tag{2.7}$$

Note that 'AC' and 'DC' here refer to the constant and periodic time-varying nature of the forces, not to electric current. Including these external forces in equation 2.6 leads to the equation of motion for a Brownian particle driven by constant and time dependent forces over a static force landscape:

$$\zeta\frac{\mathrm{d}x}{\mathrm{d}t} = F_{\mathrm{DC}} + F_{\mathrm{mod}}(t) + F_{\mathrm{T}}(x) + \xi(t). \tag{2.8}$$

This Langevin equation is central to the work described in this thesis, and will be referred to throughout.

The relative importance of the deterministic and stochastic parts of equation 2.8 may be quantified using the Péclet number. This is defined as the ratio of the time taken for the particle to diffuse over its own radius (the 'Brownian time', $\tau_{\mathrm{B}} = a^2\zeta/k_{\mathrm{B}}T$, see section 2.2.1) and the

time taken for the particle to be driven over its own radius, $\tau_{DC} = a/v_{DC}$, where a is the particle radius, and v_{DC} is the velocity at which it is driven. It may also be equivalently defined as the ratio of the driving force, $F_{DC} = \zeta v_{DC}$, and a diffusive force, $k_B T/a$, [22]:

$$\mathrm{Pe} = \frac{\tau_B}{\tau_{DC}} \equiv \frac{F_{DC}}{\frac{k_B T}{a}} = \frac{\zeta\ v_{DC}\ a}{k_B T} \tag{2.9}$$

When $\mathrm{Pe} \gg 1$, the effect of diffusion is negligible relative to the driving force, but as $\mathrm{Pe} \to 1$, diffusion becomes more important. For a system of particles of radius $a \approx 1.5$ μm driven at a velocity of $v_{DC} \approx 10$ μm s^{-1} ($\zeta \approx 1 \times 10^{-7}$ kg s^{-1}), the Péclet number is $\mathrm{Pe} \approx 350$, making Brownian motion negligible relative to the driving velocity. As the driving velocity decreases, however, so does the Péclet number: at relatively modest driving velocities of $v_{DC} \approx 1$ μm s^{-1}, the Péclet number becomes $\mathrm{Pe} \approx 35$, and at smaller velocities of $v_{DC} \approx 0.1$ μm s^{-1}, $\mathrm{Pe} \approx 3.5$. Some of the results in this thesis relate to the behaviour of particles as v_{DC} moves from zero to small finite values, making the low Péclet number regime, where diffusion is on the same order as advection, important.

2.1.2 Driving 'forces'

In the experiments in this work, the particles are either driven by solvent flow (driven by a pump) or by a piezo stage. A particle driven using either method has a net velocity, v_p, relative to the lab frame, which is the sum of its velocity with respect to the solvent, v_p', and of the solvent with respect to the lab frame, v_s. The lab frame is defined by the stationary optical potential energy landscape. The Langevin equation in the solvent frame is:

$$\zeta v_p' = F_T + \xi(t). \tag{2.10}$$

As the particle always moves *with* the solvent, there is in fact no average net force on the particle in the absence of trapping forces, as $\langle \xi(t) \rangle = 0$. In this case, the velocity of the particle in the lab frame is simply equal to v_s. In the presence of optical forces, however, the particle's velocity with respect to the solvent is $v_p' = (F_T + \xi(t))/\zeta$. As $v_p = v_p' + v_s$, it is mathematically equivalent to treat ζv_s as a constant driving force, F_{DC}, such that $v_p = \frac{dx}{dt} = \frac{1}{\zeta}\left(F_{DC} + F_{mod}(t) + F_T + \xi(t)\right)$. This is equivalent to equation 2.8, expressed in terms of the experimental observable, which is the particle position in the lab frame.

2.2 Colloidal model systems

2.2.1 Characteristic quantities

The versatility of colloidal model systems is conveniently illustrated by considering their characteristic quantities. The first of these is the colloidal length scale inherent in their definition. With length scales from nanometers (1 nm $\equiv 10^{-9}$ m) to micrometers (1 μm $\equiv 10^{-6}$ m), colloidal particles are large enough to be easily observed by optical microscopy techniques, making their real-space properties directly accessible, but also small enough that they remain dispersed in solvent, exhibiting analogous phase behaviour to atomic and molecular systems [23].

The length scale of colloidal particles leads directly to their characteristic time scale. The Brownian time, τ_B, is defined as the time taken for a particle to diffuse over its own radius, a. This is defined in terms of the diffusion coefficient, D, and the friction coefficient, ζ:

$$\tau_B = \frac{a^2}{D}, \quad \text{where} \quad D = \frac{k_B T}{\zeta}, \tag{2.11}$$

The dependence of the Brownian time on thermal energy, $k_B T$, demonstrates the importance of thermal effects on the properties of colloidal model systems. Another place where thermal energy is vital is in the gravitational length of the colloidal particles. Gravitational length, l_g, is defined as the distance by which a particle may move against gravity due to $k_B T$:

$$l_g = \frac{3}{4\pi a^3 \Delta\rho} \frac{k_B T}{g}, \tag{2.12}$$

where $\Delta\rho$ is the difference between particle density and solvent density, such that $\frac{4}{3}\pi a^3 \Delta\rho$ is the buoyant mass of a particle, and g is the acceleration due to gravity.

The final important quantity is the Young's modulus, E, of the system, which defines the softness of materials. This is defined as the ratio of stress to strain, which is equivalent to the energy per volume in the system:

$$E = \frac{\text{stress}}{\text{strain}} = \frac{F/A}{\Delta l/l} = \frac{\text{energy}}{\text{volume}}. \tag{2.13}$$

In atomic systems, with volumes of Å^3, and energies on the order of electron volts, eV, the

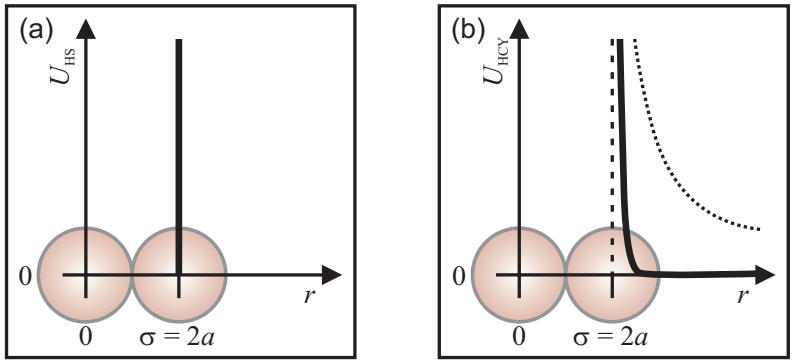


Figure 2.1: Interactions between colloidal particles. (a) Hard sphere repulsion: the interaction energy is infinite below the particle diameter, $\sigma = 2a$, and zero elsewhere. (b) Hard core screened Coulomb, or hard core Yukawa, potential. Dotted line shows Coulomb repulsion. (Not to scale).

Young's modulus is found to be $E \approx 100$ GPa. In colloidal particles, with volumes on the order of μm^3, and energies on the order of $k_B T$, the Young's modulus is found to be $E \approx 10$ mPa [66–69]. This huge difference of some thirteen orders of magnitude explains why colloidal systems are so easy to manipulate, by for example electric and/or magnetic fields [70], shear and flow [71], optical fields [59], the imposition of confinement [72], and even the addition of active components [73].

2.2.2 Colloidal interactions

The simplest inter-particle interaction in colloidal model systems is the hard sphere repulsion [24]. Hard spheres have an infinitely strong repulsion below the particle diameter, σ, and zero repulsion elsewhere (see figure 2.1a). This may be expressed as:

$$U_{\mathrm{HS}}(r) = \begin{cases} \infty, & \text{if } |r| < \sigma; \\ 0, & \text{if } |r| \geq \sigma, \end{cases} \tag{2.14}$$

where r is the particle separation. However, many colloidal particles are dispersed in water, which usually makes them slightly charged due to the partial dissociation of surface groups. This causes a small electrical double-layer to build up, whereby negatively charged groups on the particle surface will attract positively charged ions in solution. The result is that the particles interact with each other through a short-range screened repulsive Coulomb potential, or Yukawa potential [9, 74]. The hard core Yukawa potential is expressed for regions analogous to the hard

sphere repulsion [74]:

$$\frac{U_{\mathrm{HCY}}(r)}{k_{\mathrm{B}}T} = \begin{cases} \infty, & \text{if } |r| < \sigma; \\ Z^2\lambda_{\mathrm{B}}\left(\frac{\exp[\kappa\sigma]}{1+\kappa\sigma}\right)^2 \frac{\exp[-\kappa r]}{r}, & \text{if } |r| \geq \sigma, \end{cases} \tag{2.15}$$

where Z is the effective charge number of the spheres, λ_{B} is the Bjerrum length, and κ^{-1} is the Debye length. The Bjerrum length is the thermal separation for unit charges, and in water $\lambda_{\mathrm{B}} = 0.714$ nm [74]. The short ranged repulsion prevents aggregation due to attractive van der Waals forces. This clearly has no part to play in single particle processes, but when multiple particles coupled by magnetic interactions are used (see section 2.2.3), it does prevent irreversible aggregation.

2.2.3 Super-paramagnetic colloids

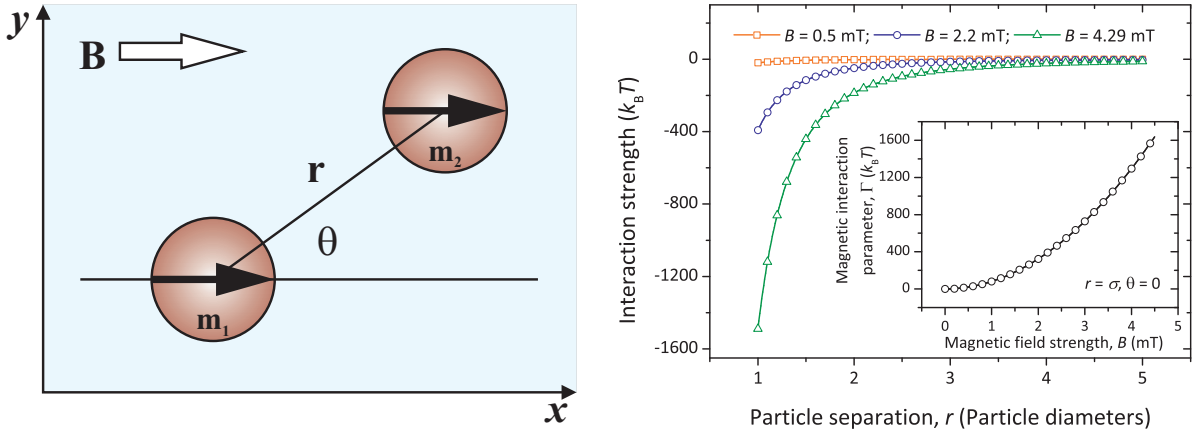
The particles used throughout this thesis are super-paramagnetic colloidal spheres, which possess a magnetic dipole moment in the presence of a magnetic field. In the absence of an external magnetic field, the single domain magnetic nano-particles embedded in the particles rapidly attain thermal anisotropy, and the particles have no magnetic dipole moment. However, when an external magnetic field is applied, the domains align, and a magnetic moment is generated. For small magnetic field strengths, the magnetic moment of the particle is directly proportional to the applied field. The magnetic interaction energy of a pair of magnetic dipoles depends on the local magnetic field strength, $\mathbf{B}_j$, and their magnetic moments, $\mathbf{m}_j$, which lie in the same direction as the imposed field (see figure 2.2a):

$$U_{12} = -\mathbf{m}_2 \cdot \mathbf{B}_1 = -\mathbf{m}_1 \cdot \mathbf{B}_2. \tag{2.16}$$

The local magnetic field strength, $\mathbf{B}_j$, may be written in terms of the magnetic moments of the particles, $\mathbf{m}_j$, and the vector between them, $\mathbf{r}$ [75] (see figure 2.2a):

$$\mathbf{B}_j = \frac{\mu_0}{4\pi}\frac{1}{r^3}\left[3(\mathbf{m}_j \cdot \hat{\mathbf{r}})\hat{\mathbf{r}} - \mathbf{m}_j\right], \tag{2.17}$$

where $\mu_0 = 4\pi \times 10^{-7}$ N A^{-2} is the permeability of free space, r is the magnitude of the vector $\mathbf{r}$, and $\hat{\mathbf{r}}$ is the unit vector between the particles. Inserted into equation 2.16, this yields an expression for the magnetic interaction energy as a function of the magnetic moments of the



(a) (b)

Figure 2.2: (a) The dipolar interaction between a pair of super-paramagnetic spheres of magnetic moments $\mathbf{m}_j$, separated by a vector $\mathbf{r}$, at an angle θ from the magnetic field vector, $\mathbf{B}$. (b) The strength of the dipolar interaction between a pair of super-paramagnetic spheres at an angle of $\theta = 0$, for varying trap separation and magnetic field. Inset: the interaction strength at contact as a function of magnetic field strength (equation 2.21).

particles:

$$U_{12} = \frac{\mu_0}{4\pi}\frac{1}{r^3}\left[\mathbf{m}_1 \cdot \mathbf{m}_2 - 3(\mathbf{m}_1 \cdot \hat{\mathbf{r}})(\mathbf{m}_2 \cdot \hat{\mathbf{r}})\right] \tag{2.18}$$

In this work the particles are identical, such that $\mathbf{m}_1 = \mathbf{m}_2 = \mathbf{m}$, so equation 2.18 becomes [76]:

$$U_{12} = \frac{\mu_0}{4\pi}\frac{1}{r^5}\left[r^2 m^2 - 3(\mathbf{m} \cdot \mathbf{r})^2\right] = \frac{\mu_0}{4\pi}\frac{m^2}{r^3}\left[1 - 3\cos^2\theta\right], \tag{2.19}$$

where m is the magnitude of the magnetic moment, and θ is the angle between $\mathbf{B}_j$ and $\mathbf{r}$ (see figure 2.2a). The magnitude of the magnetic moment, m, is related to the magnitude of the magnetic field strength, B, through the magnetic susceptibility, χ, such that $m = \chi B$. In the systems studied in this thesis, $\theta \equiv 0°$, so equation 2.19 simplifies (see figure 2.2b):

$$U_{12} = -2\frac{\mu_0}{4\pi}\frac{m^2}{r^3} = -\frac{\mu_0}{2\pi}\frac{\chi^2 B^2}{r^3} \tag{2.20}$$

The strength of the dipolar inter-particle attraction is often expressed as a dimensionless interaction parameter Γ, which gives the interaction energy at contact of a pair of particles of diameter σ (see figure 2.2b, inset):

$$\Gamma \equiv -\frac{U_{12}(r = \sigma, \theta = 0°)}{k_B T} = \frac{\mu_0}{2\pi}\frac{\chi^2 B^2}{\sigma^3 k_B T} \tag{2.21}$$

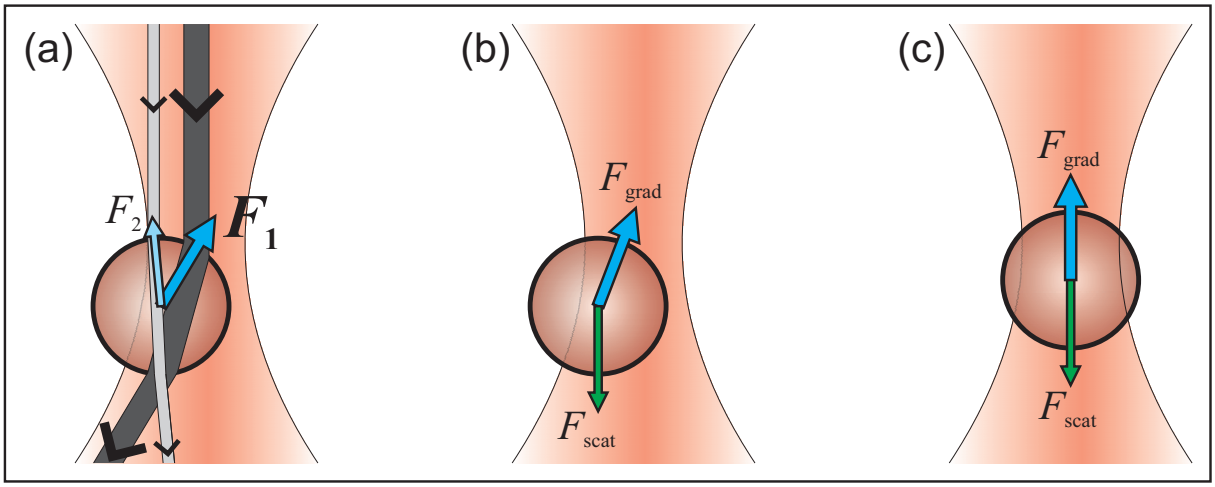


Figure 2.3: The ray optics explanation of optical trapping. (a) A particle away from the axis of the optical trap experiences a different effect from different parts of the beam, resulting in a net force up the light intensity gradient. (b) The particle in panel (a) experiences a net 'gradient' force towards the focus of the beam, and a 'scattering' force in the direction of propagation of the light. (c) A particle in the centre of the beam has balanced gradient and scattering forces, such that it sits slightly below the laser focus.

2.3 Optical trapping

Optical trapping is the effect whereby material with a different refractive index to its surroundings experiences a force when it encounters an optical gradient. Here, we consider the trapping of a sphere with a higher refractive index than the solvent in which it is dispersed. A general description of optical trapping is complex, and involves solving Maxwell's equations. The Mie solution to Maxwell's equations is the most appropriate approach for the case of a spherically trapped particle with a radius similar to the wavelength of the trapping light ($a \approx \lambda$), but this requires hugely involved calculations, which would shed little light on the way optical trapping is used in this thesis. Two approximations to Mie's solution exist, when particles are either much smaller than, or much larger than, the wavelength of the trapping light. Although these situations do not strictly apply to the situation here, they can provide some instructive qualitative insights on optical trapping.

The first of these approximations, ray optics, is valid if the particle size is much larger than the wavelength of the light ($a \gg \lambda$). This case allows for a simple and intuitive explanation of the optical trapping forces. Figure 2.3a shows a colloidal sphere, positioned off the propagation axis of, and away from the focus of, a focused laser beam. As the light from the laser beam passes through the sphere it is refracted due to the difference in refractive indices. The change in

the direction of the light results in a change in its momentum. In order to conserve momentum, the momentum of the particle must change, and it therefore experiences a force. The Gaussian intensity profile of the beam results in an intensity gradient across the particle. The two rays shown in the figure each impart a force on the particle. The central (high intensity) ray causes a larger force (F_1) than the off-centre (low intensity) ray (F_2). Figure 2.3b shows the resultant gradient force, F_{grad}. This force is partially countered by the scattering force, F_{scat}, which acts in the direction of propagation of the beam. Figure 2.3c shows a particle in the centre of the beam, slightly displaced from the centre of the focus by the scattering force, balanced by the gradient force towards the focus.

The second approximation is the Rayleigh regime, which is valid when the particle may be viewed as a point-like dipole, by virtue of having a radius significantly smaller than the wavelength of the trapping beam ($a \ll \lambda$). In this case the laser light incident on the particle is assumed to be completely absorbed, and elastically re-emitted, such that a force is exerted on the particle in the direction of the propagation of the beam. This is the scattering force, and may be expressed as [77]:

$$F_{\text{scat}} = \frac{158\pi a^6}{3\lambda^4}\left(\frac{m^2-1}{m^2+2}\right)^2 \frac{nI_0}{c}, \tag{2.22}$$

where n is the refractive index of the solvent, m is the ratio of the refractive indices of the particle and the solvent, I_0 is the laser intensity, and c is the speed of light. Note that the scattering force is proportional to intensity, and strongly dependent on particle size.

In the Rayleigh regime [78], placing the point-like dipole in the intensity gradient of the focused beam gives a 'gradient' force, which may be expressed as [77]:

$$F_{\text{grad}} = 2\pi a^3\left(\frac{m^2-1}{m^2+2}\right)\frac{n\nabla I_0}{c}, \tag{2.23}$$

where ∇I_0 is the gradient of light intensity. For a typical colloidal particle with a radius of $a \approx 1.5$ μm, and a refractive index of $n_{\text{p}} \approx 1.5$, in a solvent of refractive index $n \approx 1.33$, a 1 mW incident laser beam with a wavelength of 1064 nm, and a beam of waist $w_0 \approx 1$ μm, this corresponds to a gradient force of $F_{\text{grad}} \approx 1$ pN. The gradient force is also proportional to the laser intensity, but depends much less strongly on the particle size than the scattering force, changing as a^3, rather than a^6.

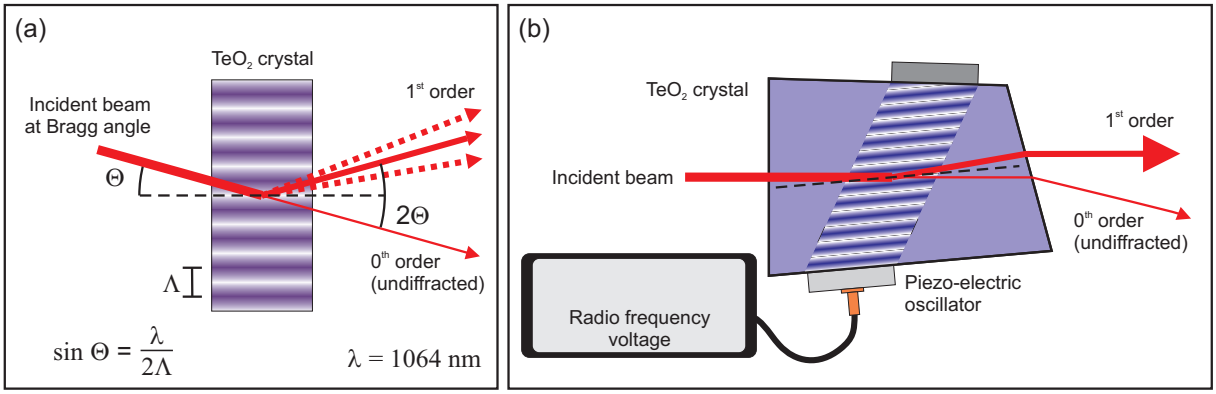


Figure 2.4: Acousto-optical deflectors. (a) The basic principle: incident light is diffracted on passing through a 'grating' formed by a phonon in a TeO_2 crystal. (b) Practical implementation: the crystal shape is designed to allow the 1st order beam to propagate collinear to the incident beam.

For stable three-dimensional trapping, $F_{\mathrm{grad}} > F_{\mathrm{scat}}$, but in this thesis, a focused 1064 nm laser beam is used to trap colloidal particles in a two-dimensional layer adjacent to the glass wall of a sample cell. Because the laser beam propagates in the direction of gravity, the scattering force is opposed by the repulsion between the particle and the wall of the cell, and therefore does not play a significant role. This allows the use of a low numerical aperture trapping objective. The laser wavelength is selected to minimise (although not eliminate) absorption and consequent heating of the particle, which may induce convection flow.

2.3.1 Acousto-optical deflectors

There are many ways to steer a laser beam. Acousto-optical deflectors (AODs) steer the beam by diffraction, due to a standing density wave generated in the TeO_2 crystal using a piezo-electric transducer (see figure 2.4a). By feeding the transducer with a radio-frequency oscillating voltage, an ultrasonic wave is propagated through the crystal, which effectively forms an adjustable micro-scale grating. Because there are two perpendicular AODs, there are four laser spots: the (0,0) order (undiffracted beam), the (1,0) and (0,1) beams (diffracted by only one AOD each), and the two-dimensionally steered (1,1) beam. Each of the AODs has a maximum efficiency of 80%. Conveniently, in most commercially available AODs the crystal and the radio-frequency wave are angled such that the (1,1) beam is collinear with the optical axis (see figure 2.4b). The AODs allow time sharing of the beam at rates of up to 100 kHz. This means that the position of the laser spot in the sample can be changed 100,000 times a second, allowing many optical traps to exist simultaneously on the time scale of the particles.

2.4 Experimental methods

2.4.1 Colloidal model system

The colloidal particles used throughout this thesis are Dynabeads® M-270 Carboxylic Acid (Lot H45501, 2011-02), which are highly monodisperse cross-linked polystyrene spheres with an advertised diameter of 2.8 μm [79], which is found to increase to 3.0 μm in the solvent used in this work. The particles are dispersed in a 20% $EtOH_{(aq)}$ solution, which prevents the growth of bacteria. This solvent mixture has a density of 970.9 kg m^{-3}, and a viscosity of 1.5963 × 10^{-3} Pa s [80]. The particles have a density of 1600 kg m^{-3} and a Brownian time of 50 s. The friction coefficient, ζ, is determined by measuring the mean squared displacement, as described in section 2.1. The small gravitational length in this system (l_g = 0.04 μm) means that the particles rapidly sediment, forming a quasi-two-dimensional layer. The characteristic quantities of the colloidal model system are summarised in table 2.1.

The particles are functionalised with CO_2H groups, giving them a small negative charge in solution, inhibiting aggregation without the need for added surfactant [79]. The super-paramagnetic properties stem from iron oxide distributed throughout the polystyrene, as γFe_2O_3 and Fe_3O_4, the iron content being 14% by mass [79,81]. The iron oxides are in the form of single domain nano-particles, which are free to rotate, but cannot escape the polystyrene [79]. Each nano-particle is ferromagnetic, but the thermal isotropy of the nano-particles within the colloidal particles make the particles as a whole super-paramagnetic: they have no magnetic moment in the absence of a magnetic field, but a magnetic moment is generated on the application of a field [82]. This magnetic moment is fully and rapidly (< 1 s) reversible on removal of the field. At the magnetic fields used in this work, the strength of the magnetic moment is

Quantity	Symbol	Value
Radius	a	1.5 μm
Density	ρ_p	1600 kg m^{-3}
Friction coefficient	ζ	9.19×10^{-8} kg s^{-1}
Brownian time	τ_B	50 s
Gravitational length	l_g	0.04 μm
Magnetic susceptibility	χ	6.7×10^{-12} A m^2 T^{-1}

Table 2.1: Properties associated with the colloidal model system.

directly proportional to the applied field, through the magnetic susceptibility, χ [82, 83], which is measured using SQUID magnetometry [84].

The effective two-dimensional optical trapping (see section 2.3) and the small gravitational height of the particles (see table 2.1) mean that the added suppression caused by the incident laser beam is small. The friction coefficient in the absence of a laser has been found from mean squared displacement measurement to be 9.19 $\times 10^{-8}$ kg s^{-1}. In an optical trap with $\sim$ 0.75 mW of laser power at the sample, the friction has been found to be 1.07 $\times 10^{-7}$ kg s^{-1}. Because this is such a small difference, it is not necessary to compensate the friction coefficient for the effect of different light intensities across the sample.

2.4.2 Sample cells

The basic sample cell used is a custom made quartz glass cell (Hellma, see figure 2.5) with an internal height of 200 μm, a width of 9 mm and an internal length of 20 mm. Before every experiment the cell is cleaned using a 2% Hellmanex solution at 40°C, rinsed with 20% $EtOH_{(aq)}$, dried on a hotplate at 80°C for 15 minutes, and treated with oxygen plasma. The plasma cleaning process has the dual effect of breaking down any remaining organic contaminants, and making the surface slightly negatively charged, helping to prevent the adhesion of particles to the cell wall. Cells are sealed at the ports using Blue-tac to prevent evaporation of the solvent. For the flow experiments, the cell is adapted from the basic Hellma cell by using a pair of home-made connectors. One end of each connector slots snugly over one of the glass in-/out-lets of the cell, and the other end accommodates a flexible wide-walled microfluidics tube.

2.4.3 Optical trapping setup

The optical trapping setup used to conduct the experiments in this thesis is shown as a schematic in figure 2.5, and photographs of the setup are shown in figures 2.7 and 2.8. Table 2.2 gives details of the specific components used. The apparatus consists of optical tweezers coupled to an inverted bright field optical microscope. The system is built on a damped optical table, supported on air-filled legs, to eliminate vibrations. All cables which connect to apparatus on the table are damped with foam blocks to further eliminate outside vibration. Air conditioning is used to maintain the lab air temperature at 25°C.

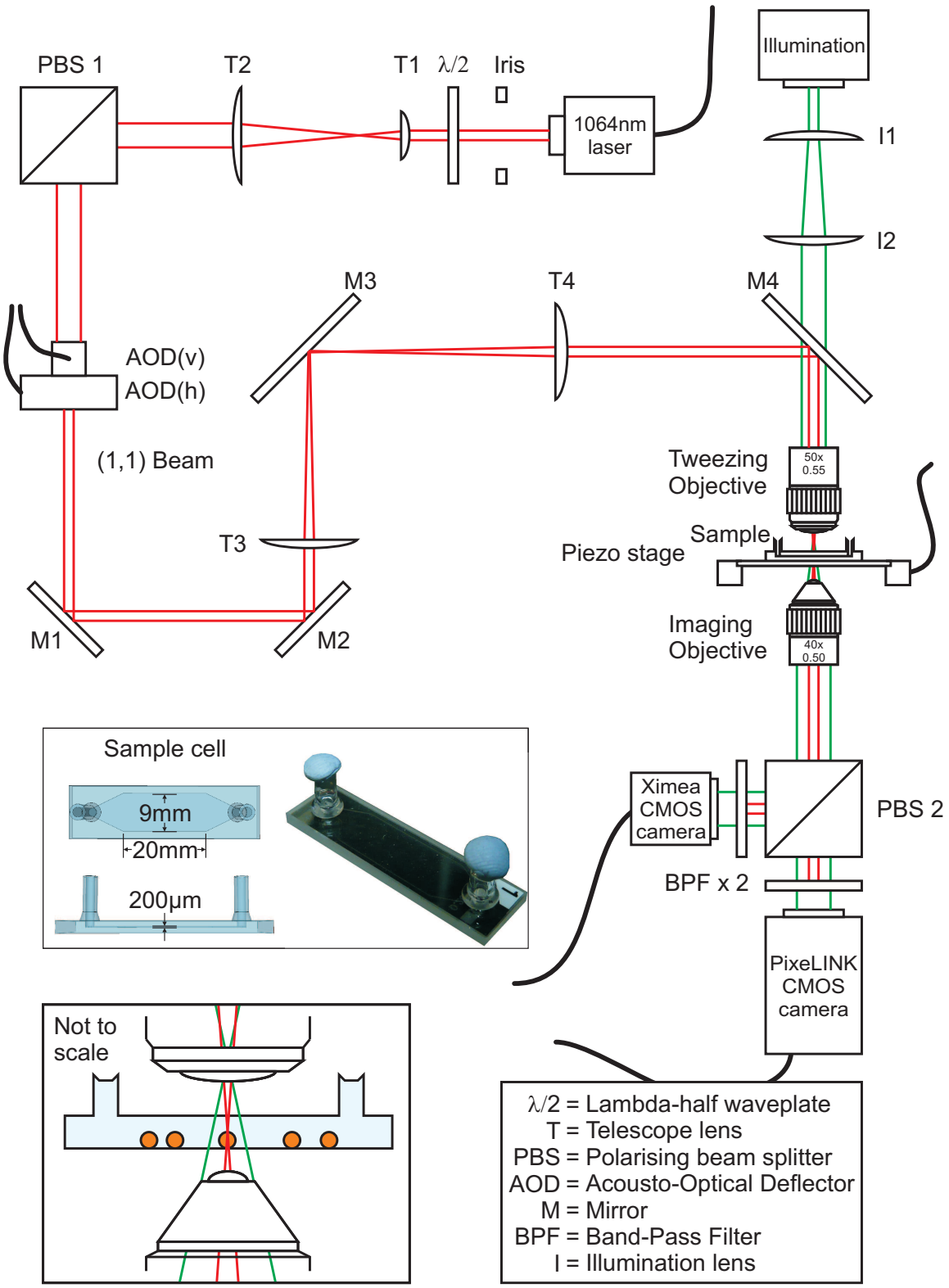


Figure 2.5: Diagram of the optical setup consisting of an inverted microscope and optical tweezers. The beam is expanded (T1,T2) to overfill the aperture of the AODs. The (1,1) beam from the AODs is directed through a periscope (M2-M4), and a 1× telescope (T3-T4), so that it enters the back of the tweezing objective, and is focused into the sample cell. Illumination also passes through the tweezing objective, and the image is focused onto two cameras using the imaging objective. The Hellma sample cell is also shown.

Item	Make/model	Details
Optical table	Newport RS4000	4 × PL-2000 legs.
Laser	Coherent Compass 1064-4000M	Diode pumped cw laser, max. power 4 W. Gain medium: Neodymium:Vanadate. λ = 1064 nm.
AODs	AA Opto-Electronic DTSXY-250-1064	TeO_2 crystals.
Beam steering controller	Aresis	Time-sharing at up to 100 kHz.
Fiber Illuminator	Thor Labs OSL1-EC	
Trapping objective	Leica 50×, NA=0.55	Long working-distance. Mounted on ThorLabs SM1Z.
Imaging objective	Zeiss 40×, NA=0.50	Long working distance. Mounted on Thor Labs SM1ZM.
Camera	PixeLink PLB-741U	CMOS, 1280 × 1024 pixels, USB 2.0. Required for AOD calibration.
Camera	Ximea MQ013MG-E2	CMOS, 1280 × 2048 pixels, USB 3.0.

Table 2.2: Components of the optical trapping setup.

A 1064 nm laser is used to provide the optical trapping beam. The laser light passes through a lambda-half waveplate ($\lambda/2$) which can be used to reduce the intensity of the beam after the first polarising beam splitter (PBS 1). The laser beam is expanded by ~ 10× through the first telescope (T1, T2), before reflecting from the beam splitter (PBS 1). The expanded beam overfills the aperture of a pair of acousto-optical deflectors (see section 2.3.1), which are used for beam steering. The large area of the trapping region (up to 150 μm square) requires a large range of diffraction angles. The AODs are not equally efficient over this range, and for experiments requiring large optical potential energy landscapes, the AOD output is flattened using the Tweez software and a photo-diode. This results in equal laser power throughout the trapping region (see figure 2.6).

The (1,1) beam from the AODs is selected by mirror M1, and directed via mirrors M2-M4 through a second telescope (T3-T4, 1× magnification), which ensures that the deflected beam from the AODs is projected into the back aperture of the trapping objective. The objective is mounted on a translation mount, which allows very tight focusing, and is also very stable, such that the focus remains in the same two-dimensional plane over long periods of time. The beam waist radius, $w_0 = \frac{\lambda}{\pi\theta} = 0.79$ μm, where $\lambda = 1064$ nm is the wavelength of the light. The opening angle is $\theta = \arcsin\left[\frac{\mathrm{NA}}{n}\right]$, where NA is the numerical aperture of the objective, and $n = 1.33$ is the refractive index of the solvent. This corresponds to a spot size of $2w_0 = 1.58$ μm. The sample

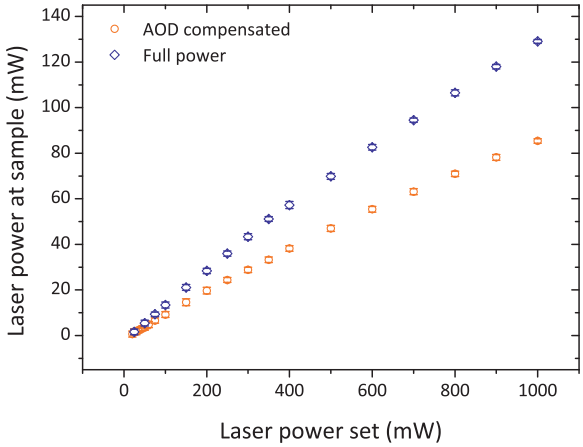


Figure 2.6: Typical laser power calibration for full power beam and AOD field flattening.

cell (see section 2.4.2) is mounted below the trapping objective, either on a plastic support (for flow experiments) or on the piezo stage (see section 2.4.5).

2.4.4 Inverted bright field microscope

An inverted bright field microscope is coupled into the optical trapping setup at mirror M4 (see figures 2.5 and 2.7). The illumination is expanded and de-focused into the back of the trapping objective. It is necessary to defocus the light so that the imaging area is large and the bundle of fibers is not focused onto the image plane. Imaging is done via a second microscope objective, mounted below the sample on a mechanical focusing ring. Although this mount precesses slightly when focused, it is very stable once set. A polarising beam splitter allows dual imaging on the two cameras (PixeLink and Ximea). The PixeLink camera is used to record movies and take snapshots of the system. The Ximea camera is much faster and gives more stable frame rates, and is therefore used for live particle tracking. The advantage of having both cameras is that the live feed from the tracking camera can be switched off (to improve frame rate stability), while keeping the other camera on to watch the system on the screen. Both cameras are protected from the trapping laser with infra-red bandpass filters.

All three of the microscope modules (trapping objective, sample stage, and imaging module) are mounted on Owis x-y translation stages. The only z-translation is at the two objectives, as z-translation for the whole modules is found to cause the focus to drift over time. Stability is incredibly important in the experiments in this thesis, where the consistency of the trapping focus must be maintained over many hours.

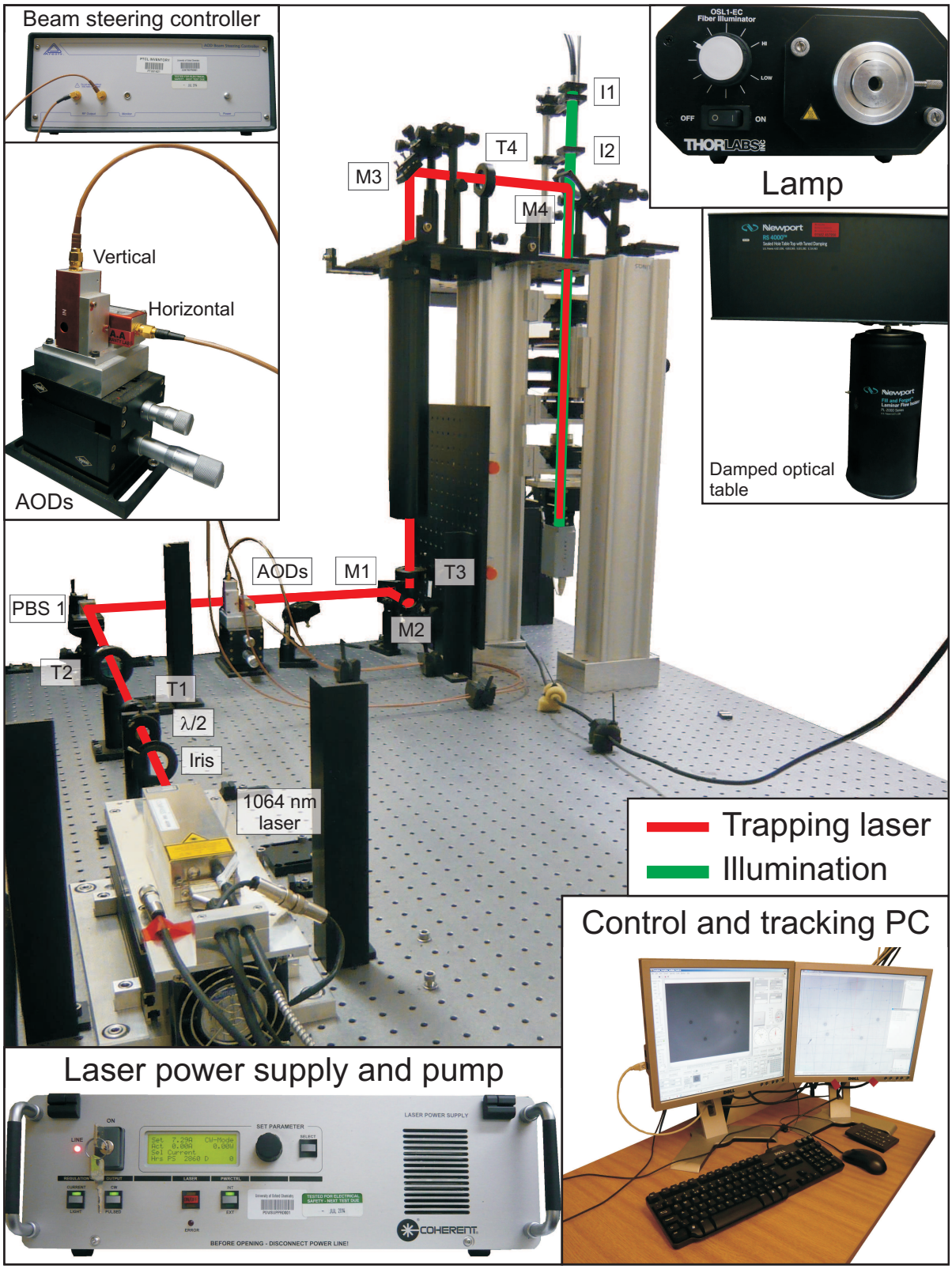


Figure 2.7: Photograph of the experimental setup shown in figure 2.5, mounted on the damped optical table. The laser head is fed by a diode pump in the power supply unit. The AODs are controlled by the beam steering controller. The illumination is provided by a lamp connected to the top of the inverted microscope by a fiber. The laser, AODs, cameras, and piezo stage are addressed by the LabView control software.

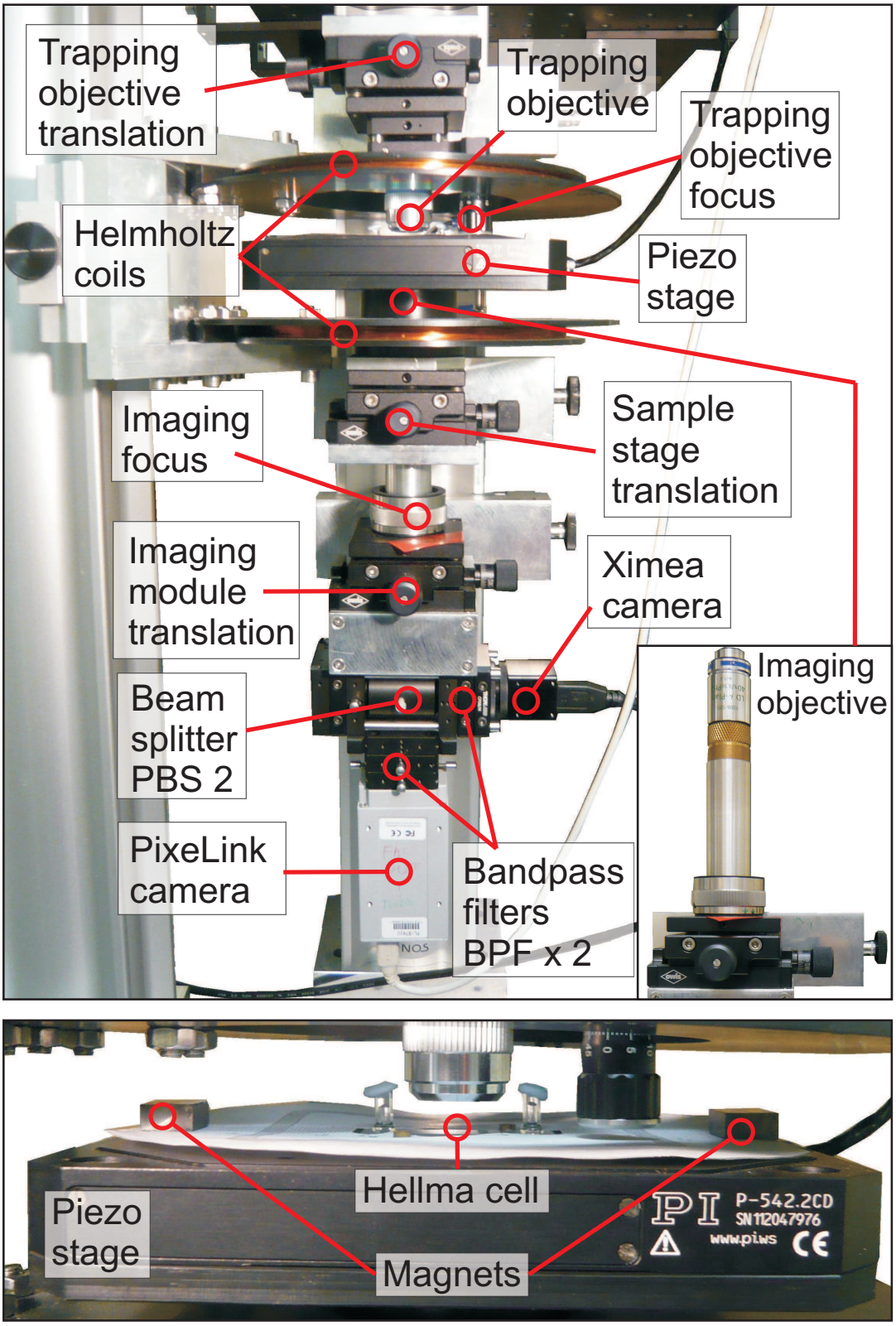


Figure 2.8: The inverted microscope section of the optical setup shown in figure 2.5. Laser light and bright-field illumination enter the back of the trapping (upper) objective. Laser light is focused in the image (particle) plane, illumination is focused away from the image plane. The sample cell is held on the piezo stage, between the objectives. The imaging (lower) objective focuses the image onto two cameras, via a beam splitter. The cameras are protected by bandpass filters.

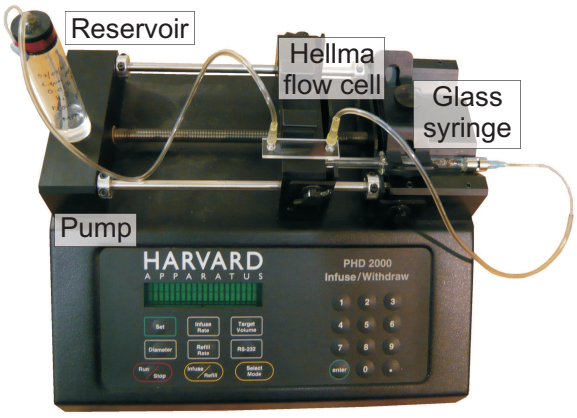


Figure 2.9: Example flow system. The micro-fluidics pump drives a glass syringe, connected via micro-fluidics tubing to the Hellma cell. A reservoir is connected to the other opening of the Hellma cell.

2.4.5 Driving colloidal particles

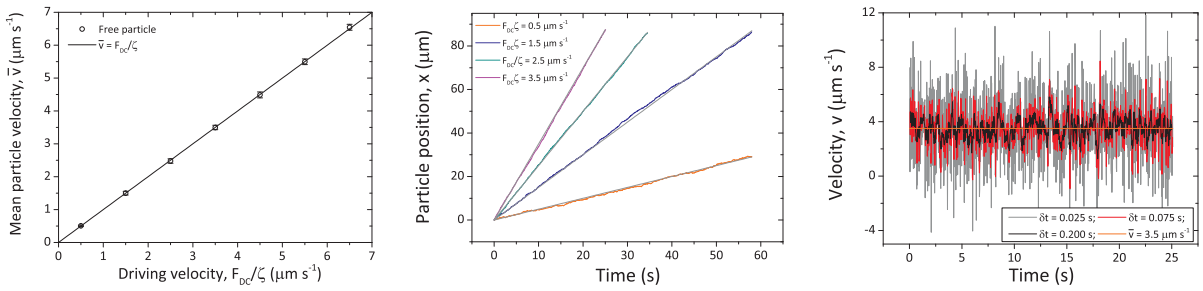
Two methods of driving colloidal particles on optical potential energy landscapes have been used in this work: solvent flow from a micro-fluidics pump, and a piezo stage.

Flow

A semi-open flow system is assembled as shown in figure 2.9. The micro-fluidics pump (Harvard PhD2000) drives a glass syringe with a ground glass plunger, which minimises flow rate fluctuations and hysteresis when reversing the pumping direction. The syringe needle is connected to the inlet of the cell described in section 2.4.2 by micro-fluidics tubing. The outlet of the cell is inserted into a reservoir of the suspension in use, and submerged under the surface to prevent the introduction of air bubbles. The reservoir is fitted with a lid designed to equalise air pressure between the reservoir and the lab, while minimising evaporation.

Piezo-stage

A piezo-electric microscope stage (PI-542.2CD) is used to drive the entire sample cell (see figure 2.8). The stage has has a total travel of 200 µm, and a precision of 0.4 nm in closed-loop mode. The stage position is controlled by instructions sent from the LabView control interface via a control unit (E-625), which also passes back the actual position of the stage. The sample cell is mounted in the piezo-stage aperture via a custom-made insert.



(a) (b) (c)

Figure 2.10: Trajectories of a Brownian particle driven by the piezo stage. (a) The mean velocity, $\overline{v}$, of a particle driven across the field of view by driving velocity F_{DC}. Error bars represent the standard deviation of the repeats. The line has a gradient of 1. (b) Individual particle trajectories for various driving velocities. Solid lines have gradients of 0.5, 1.5, 2.5, and 3.5. (c) Typical velocity fluctuations obtained from the F_{DC} = 3.5 μm s^{-1} trajectory in panel (b).

The driving velocity provided by the piezo-stage is calibrated by driving at velocities from 0.5 μm s^{-1} to 6.5 μm s^{-1} in steps of 1 μm s^{-1}, each point being repeated ten times. Figure 2.10a shows that in the absence of an optical landscape the average particle velocity is equal to the driving velocity of the stage (see section 2.1.1). The instantaneous particle velocity fluctuates due to Brownian motion. Figure 2.10b shows particle trajectories for four different driving velocities, and it is clear that although the average velocity is the same as the driving velocity, the gradient of the particle trajectory, $x(t)$, is not constant. Figure 2.10c shows the particle velocity calculated from the trajectory for F_{DC} = 3.5 μm s^{-1} from figure 2.10b, finding the derivative over varying time steps. This shows that the level of fluctuations depends on difference in time between position measurements, so this time difference must be kept constant.

2.4.6 Magnetic fields

Magnetic fields are introduced using a pair of identical permanent magnets, equally spaced from the centre of the optical axis of the microscope (see figure 2.8). The spacing is sufficient that the magnetic field is homogeneous within the experimental field of view. Figure 2.11a shows how the strength of the magnetic field depends on the spacing between the magnets (measured as the spacing of each from the centre). The measured points are fitted with a function of r_{m}^{-2}, which works well while the spacing $r_{\mathrm{m}} \geq 30$ mm. Figure 2.11b plots the magnetic field strength against the inverse of the squared distance, such that the plot should be linear. It is found to be linear for $r_{\mathrm{m}} \geq 30$, but at smaller separations the field is slightly enhanced, due to the presence of the microscope objectives, which act as iron cores.

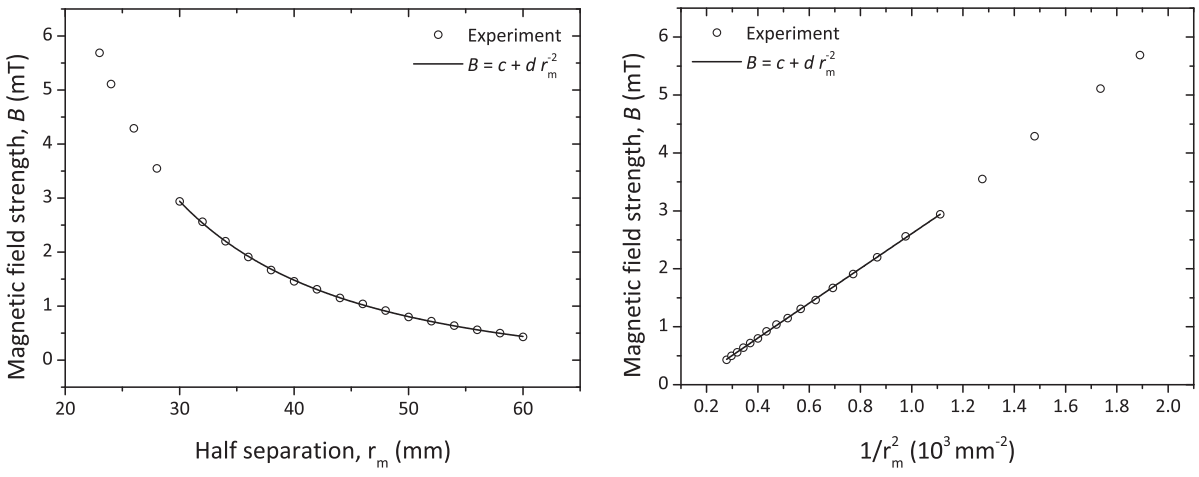


Figure 2.11: The magnetic field found at the sample position as a function of magnet separation from the centre. Field strength increases more steeply than expected when separation is small, as the microscope objectives slightly enhance the field.

2.4.7 Software

LabView control software

The laser, AODs, piezo-stage and imaging/tracking camera are all brought together by control software constructed in LabView. The first great advantage of using one piece of control software is that the timings of the various components may be synchronised. The second is that particles may be tracked live, saving a huge amount of time and processing power over recording movies, decomposing movies to images, and processing those images to find particles.

The main structure of the code is simple: a start-up section initialises and checks all of the hardware; three separate and simultaneous timed loops control the trapping, stage motion, and imaging/tracking; a shut-down procedure closes down the hardware and outputs particle co-ordinates. Each of the three timed loops is run on a dedicated processor core, such that they do not interfere with each other, and may be run at consistent rates.

Laser: The laser is controlled via a LabView VISA connection, allowing control of power.

AODs: The AODs are controlled via a TCP/IP connection to the Aresis Tweez software (supplied with the Aresis beam steering controller), which acts as a server. Thus, static and dynamic trapping patterns designed in LabView may be applied in real time.

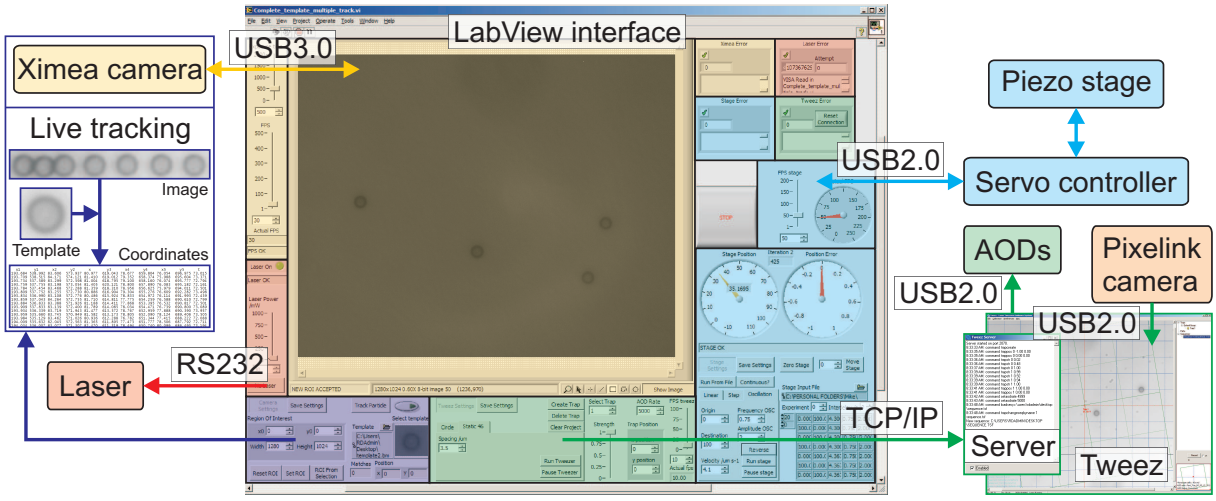


Figure 2.12: Diagram showing how the LabView interface connects with the various parts of the system, including the Ximea camera used for live particle tracking, and the Tweez software, through which the AODs are controlled.

Piezo stage: The piezo stage is controlled via proprietary sub-VIs provided by the manufacturers, PI. Self-written LabView code calculates real-time positions for linear and oscillating paths, and applies them in real time.

Imaging: The Ximea CMOS camera image is streamed live to a LabView Imaq environment, allowing manipulation of frame rate, exposure time, and field of view.

Tracking: Implementation of Imaq template tracking allows a template particle to be selected from the live image, which is then used to identify particles in the image. The number of particles expected is set to improve consistency of results. It is possible to locate over 20 particles via this method without any loss of speed.

IDL tracking code

When experimental movies are recorded using the PixeLink camera, post-processing is required to assign particle positions and identities. The first stage is to decompose the 24-bit .avi movies into stacks of 8-bit .tif images, using ImageJ. This process can require a large amount of memory and processing time. Particle positions are then identified in the image stack using Interactive Data Language (IDL) routines developed by Crocker and Grier, and improved by Weeks [85,86]. To find particle positions, first a numerical bandpass filter is applied to minimise noise in the background, then Gaussian shaped 'features' of the size of the particles are identified. The range

of features found is then cut down by brightness, radius, and ellipticity, such that only particles remain. The positions from a time-series of images are then tracked, to assign particle identities and find trajectories.

Acknowledgements

The group of Clemens Bechinger at the University of Stuttgart are thanked for the original optical tweezer design. Arran Curran is thanked for his assistance with optics. Thomas Skinner is thanked for practical assistance. The PTCL mechanical workshops are thanked for interpreting and constructing the author's designs.

Chapter 3

Mapping optical potentials using driven colloidal particles

Abstract

In this chapter the properties of single optical traps and optical potential energy landscapes are determined using colloidal particles driven by solvent-flow and a piezo-stage. Single traps are found to have a Gaussian potential, and the magnitude of the trapping stiffness is found to be linearly proportional to the laser power, I_0, consistent with thermal equilibrium methods. The depth of the optical trap, which is not accessible using thermal equilibrium methods, is also found to be directly proportional to I_0. These measurements are then extended to more complex periodic and aperiodic potentials, and it is shown that the exact nature of optical potential energy landscapes may be fully controlled, engineered and predicted using a sum of single Gaussian potentials. Finally, periodic optical potential energy landscapes are mapped using small linear clusters of particles, and it is shown that the potential extracted is the same as that for single particles, even though the cluster velocity differs from that of a single particle on the same potential landscape.

3.1 Introduction

Undulating potential energy landscapes appear in a vast range of physical systems, from the surfaces of atomic crystals [87] to Josephson junctions in superconductors [88]. Modelling such landscapes has become an important challenge in science and engineering as many devices and electronic systems become smaller and their features become more difficult to probe directly [89]. Model potential energy landscapes have been created with a wide range of techniques. These vary from directly structuring surfaces using lithographic techniques [90–92] to selectively adsorbing nano-particles or colloidal particles to surfaces [93, 94].

Laser light has also been used to create optical potential energy landscapes [35, 60] (see chapters 1 and 2), which have been utilised to address problems ranging from particle sorting [49–52, 54], phase behaviour [42] and Kramer's hopping [60, 95–97] to nanotribology [35, 44]. For all of these applications a detailed knowledge of the potential energy landscape is crucial. In laser based particle sorting techniques for instance, the efficiency depends sensitively on the deflection angle, whose optimum may be predicted from the details of the landscapes [49, 51, 52, 54].

Optical potential energy landscapes, $U(x)$, are generally characterized as a function of position, x, by inverting the probability distribution, $P(x)$, of Brownian particles in the landscape using Boltzmann's factor $P(x) \propto \exp\left[-\beta U(x)\right]$, where $\beta = (k_{\mathrm{B}}T)^{-1}$ with k_{B} Boltzmann's constant and T the absolute temperature [29, 42, 60, 96–98]. However, with thermal fluctuations being the motive force, this approach is typically limited to optical potentials with a depth, V_0, of a few $k_{\mathrm{B}}T$. Also, characterizing single optical traps by this method leads to the restoring force, $F_{\mathrm{T}} = -kx$, of a harmonic optical potential [29, 98], where k is the trapping stiffness and x the displacement of a particle from the center of the trap. This linear regime is generally sufficient in the limit of small fluctuations, but breaks down for larger displacements [99–101]. This is particularly important for non-equilibrium optical trapping applications such as active micro-rheology [47, 48]; during the dragging of a trapped particle though a viscoelastic medium the particle is likely to sample the non-linear regions of an optical trap.

To characterize the full potential energy of single optical traps and deeper potential energy landscapes with wells of tens of $k_{\mathrm{B}}T$, driving forces up to typically a pico-Newton are required. Piezoelectric stages [99, 100] and a dual-beam optical trap [101] have been used to drive single

trapped particles away from the trap center, and a stiffening of the optical trap has been observed. In the case of extended potential energy landscapes Arzola et al. reported a study of a particle on an inclined plane, passing an optical washboard potential created by interference fringes [102]. This approach uses various particles on the order of 10 μm in diameter, such that gravity is a sufficient driving force for particles to escape individual traps. Further studies report particle sorting using the solvent driven flow of colloidal particles over optical landscapes created using interference patterns [51], spatial light modulators (SLMs) [39, 49, 50, 54] and acousto-optical deflectors (AODs) [52].

In this chapter, acousto-optically generated 'one dimensional' (1D) optical potential energy landscapes are combined with driven colloidal particles to quantitatively characterize the full optical potential energy landscape. Firstly, the drive is provided using a well-defined solvent flow, and secondly using a piezo-electric microscope stage. The particles are driven along an axis through the centers of the 2D circularly symmetric optical traps, resulting in a 1D potential measurement. The driving force given by solvent flow or piezo-electric drive is on the order of pico-Newtons to tens of pico-Newtons. Using the Langevin equation (see section 2.1.1, equation 2.8) [54, 102], it is possible to simultaneously measure the trapping stiffness, k, and the depth, V_0, of the traps constituting the optical landscape.

3.2 Theory

3.2.1 Dynamics of particles driven over optical traps

As discussed in chapter 2, the force on a driven Brownian particle in an optical potential energy landscape is given by the Langevin equation (equation 2.8). At low Reynolds numbers (Re) and high Péclet numbers (Pe), a deterministic version of the Langevin equation may be used, such that the stochastic force, $\xi(t)$, is neglected. Particles driven at a velocity v_{DC} experience a driving force $F_{\mathrm{DC}} = \zeta\, v_{\mathrm{DC}}$. The presence of an optical potential energy landscape introduces an additional force, $F_{\mathrm{T}}(x)$, which depends on the position coordinate, x, and causes perturbations to the velocity of the particle. Thus, the deterministic equation of motion is given by:

$$\frac{\mathrm{d}x}{\mathrm{d}t} = v_{\mathrm{DC}} + \frac{F_{\mathrm{T}}(x)}{\zeta} = \frac{1}{\zeta}\left(F_{\mathrm{DC}} + F_{\mathrm{T}}\right). \tag{3.1}$$

Measuring this instantaneous velocity as a function of the position of the particle, x, thus provides a direct measure for the optical forces and hence the potential energy landscape.

Following previous work, we model a single optical trap as a Gaussian well [50, 54, 103]:

$$V(x) = -V_0 \exp\left[-\frac{k(x-x_0)^2}{2V_0}\right], \tag{3.2}$$

with x_0 the position of the center of the trap, k the trapping stiffness, and V_0 the depth of the optical potential well. The optical landscape produced through the combination of M single optical traps may be described by a sum of the potentials of the individual traps [54]:

$$U_T(x) = -\sum_{i=1}^{M} V_{0,i} \exp\left[-\frac{k_i(x-x_i)^2}{2V_{0,i}}\right]. \tag{3.3}$$

The optical force is then easily obtained, as $F_\mathrm{T} = -\frac{\mathrm{d}U_T(x)}{\mathrm{d}x}$, which is substituted into equation 3.1 to obtain the instantaneous velocity of a particle travelling across the potential energy landscape:

$$v(x) = \frac{1}{\zeta}\left(F_\mathrm{DC} - \sum_{i=1}^{M} k_i(x-x_i) \exp\left[-\frac{k_i(x-x_i)^2}{2V_{0,i}}\right]\right). \tag{3.4}$$

Hence, fitting velocity profiles, $v(x)$, with this equation directly leads to the fundamental features of the optical landscape, k_i, $V_{0,i}$ and x_i.

3.3 Experimental methods

3.3.1 Colloidal model system

As described in section 2.4.1, the particles used in this chapter are Dynabeads M-270 Carboxylic Acid, dispersed in 20% $\mathrm{EtOH_{(aq)}}$, where they are found to be of diameter 3.0 μm. They are contained within a Hellma cell, as described in section 2.4.2, at a dilution such that it is possible to have only a single particle within the field of view. The friction coefficient is found experimentally to be $\zeta = 9.19 \times 10^{-8}$ kg s^{-1}.

3.3.2 Experimental setup

The experimental setup is described in section 2.4, and consists of an infra-red (1064 nm) laser, controlled using a pair of perpendicular AODs, and focused using a 50x, NA=0.55 microscope objective. Single optical traps and landscapes are generated in Aresis Tweez software, which may be instructed from the LabView interface. Images are made on two cameras using a 40x, NA=0.5 microscope objective.

3.3.3 Equilibrium trap measurements

One traditional method for finding the stiffness of an optical trap is to take a long time series of the position of a Brownian particle held by the trap [29]. As such, a particle is held in the optical trap used for the flow experiments, and images recorded at 2 fps for up to an hour. A probability distribution of particle co-ordinates is obtained, which may be analysed by taking the Boltzmann factor, because $P(x) \propto \exp[-U/k_{\mathrm{B}}T]$. Assuming a parabolic potential for the centre of the trap, such that $U = \frac{1}{2}kx^2$, this may be rewritten as $-\ln[P(x)] \propto U/k_{\mathrm{B}}T = kx^2/2k_{\mathrm{B}}T$. As the particle will only thermally explore the trap up to $\sim 6\ k_{\mathrm{B}}T$, this method consistently underestimates trap stiffness, as the outer portions of the trap, where stiffening has previously been noted [99–101], cannot be measured.

3.3.4 Flow experiments

Particles are held within a Hellma flow cell, connected to a Harvard PhD2000 pump and a reservoir, as described in section 2.4.5. Movies are recorded at 50 frames per second using the PixeLink camera, decomposed to a sequence of 8-bit images using ImageJ, and particle positions found using the IDL tracking procedure described in section 2.4.7.

3.3.5 Piezo-driven experiments

Particles are held within a closed Hellma cell, securely held on a PI-542.2CD piezo-stage, controlled using the LabView interface. Image positions are recorded live at 40 Hz from the Ximea camera image, using the tracking procedure described in section 2.4.7.

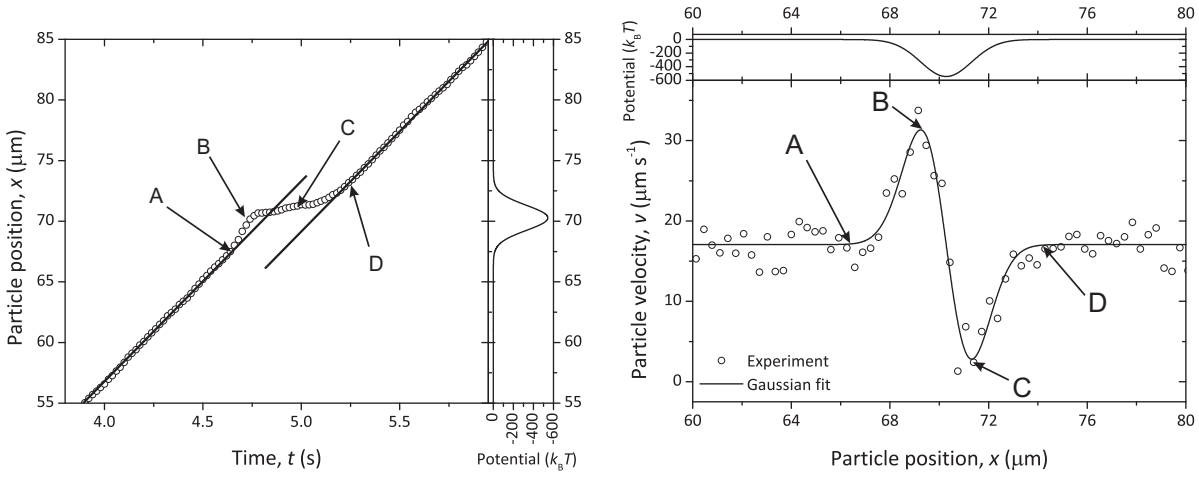


Figure 3.1: Typical experimental data as obtained from flow experiments for single optical traps. Points A-D show the extent of the optical trap, and are described in detail in the text. (a) The particle position as a function of time: ○ experimental data; solid lines are linear fits of equal gradient, indicating that the particle velocity equals the flow velocity before and after the optical trap. The right panel shows the corresponding potential, $U(x)$. (b) The particle velocity $v(x)$ as a function of the position: ○ experimental data; the solid line is a fit based on a Gaussian optical trap according to equation 3.4. The top panel again shows $U(x)$.

3.4 Results and discussion

3.4.1 Flow experiments

Single optical traps

Firstly, the colloidal particles are driven at ~ 15 μm s^{-1} along a linear path, running through the centre of a single optical trap. Figure 3.1a shows the position of the particle as a function of time as obtained from the tracking routines. The early and late parts of the position versus time graph are linear and of the same gradient, indicating the particle travelling at the imposed flow velocity far away from the optical trap. When the particle travels through the optical trap its velocity is affected and a characteristic position-time pattern is observed, indicated in figure 3.1a by the markers A to D. The corresponding velocity versus position graph is shown in figure 3.1b. Initially the particle proceeds at the constant velocity of the solvent flow, until point A, when there is a period of acceleration due to gradient forces of the optical trap. The velocity then rapidly drops to its minimum at C, where the gradient force now opposes the flow forces. Beyond this point, the particles accelerates to reach the flow velocity at D.

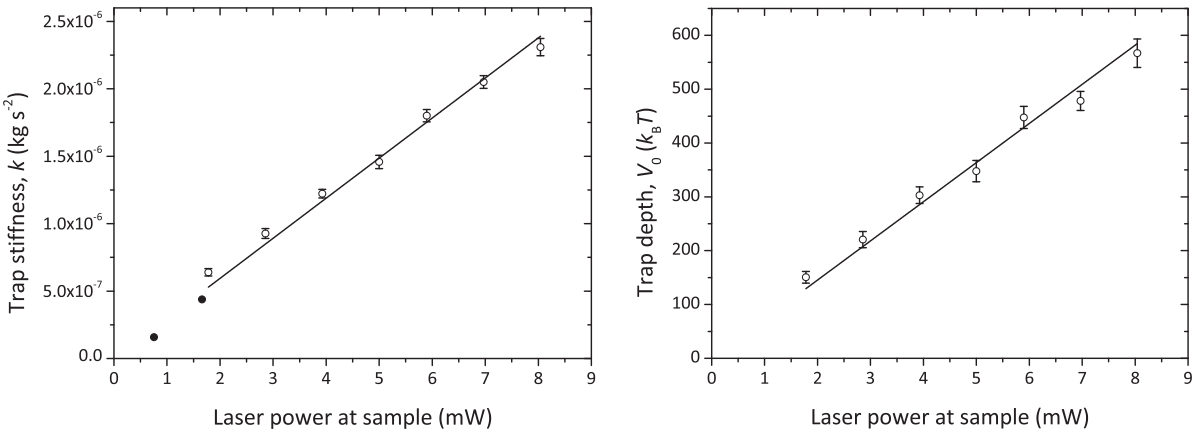


Figure 3.2: (a) The trapping stiffness k (○ flow measurements; • thermal equilibrium measurements) and (b) the depth of the optical trap V_0 as a function of the laser power. The solid lines are linear fits to the data.

Assuming a Gaussian potential for the optical trap (equation 3.2), the experimental data for $v(x)$ is fitted according to equation 3.4 to obtain the complete optical potential, fully characterised by the trapping stiffness, k, and the depth of the optical trap, V_0. The solid curve in figure 3.1b shows that this assumption is valid, and that the region of influence of the trap is around 10 μm. The potential energy landscape, $U(x)$, is also shown in figures 3.1a and 3.1b for completeness. The velocity profile in figure 3.1b is also a direct measure for the force profile (see equation 3.1) and can be directly compared to earlier work which reported a stiffening of the potential at larger displacements [99–101]. The velocity profile shown here appears very similar to the force profile reported in [100, 101], although the uncertainty in the data presented here does not allow the resolution of the expected stiffening of the trap, which would appear between points B and C as a deviation from the derivative of a Gaussian potential.

Next, the laser power dependence of k is determined, and is presented in figure 3.2a. As expected k increases linearly with laser power consistent with earlier reports, e.g. [98, 104]. Also, the k values from flow measurements match well with those from the thermal equilibrium method [29], suggesting that the flow technique used here is indeed an effective, easy and fast way to obtain this information. The depth, V_0, of the optical trap, can only be determined from the full optical force field as shown in figure 3.1b [100, 101]. The measurements presented here show that V_0 is linearly proportional to the laser power for depths up to $\sim 500\ k_\mathrm{B}T$, consistent with theoretical predictions [54, 78]. So far this has only been experimentally demonstrated for potential energy landscapes with maximum energy wells on the order of a few $k_\mathrm{B}T$ using the

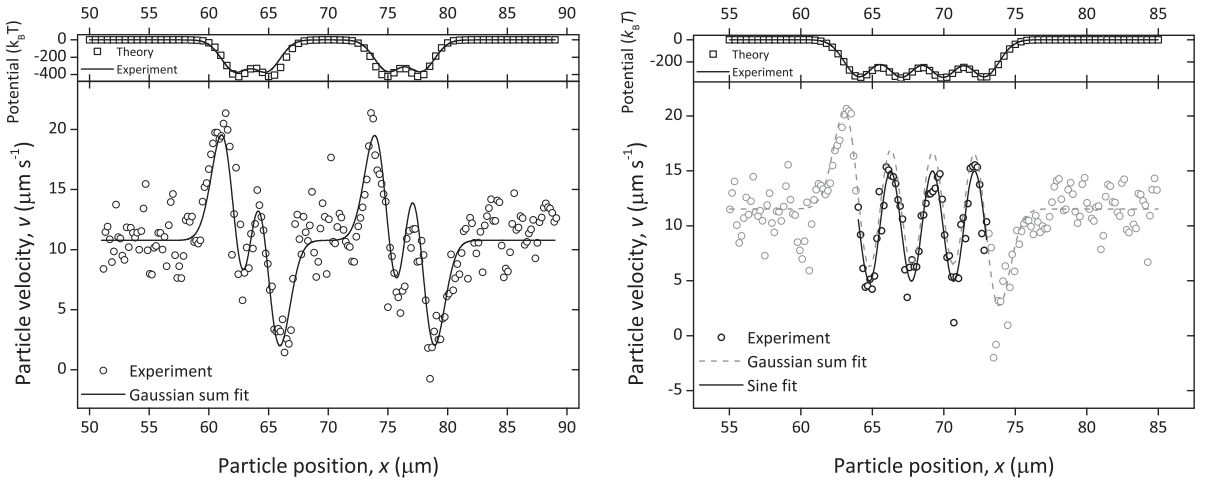


Figure 3.3: The particle velocity $v(x)$ as a function of the position x when driven at a flow velocity of ~ 11 μm s^{-1} through two different optical landscapes, where δ_{ij} is the distance between traps i and j: (a) two pairs of overlapping optical traps positioned at $\delta_{12} = \delta_{34} = 3$ μm and $\delta_{23} = 10$ μm. ○ experimental data, — is a fit according to equation 3.4. (b) Four traps with spacing $\delta = 3$ μm. ○ experimental data, - - - is a fit according to equation 3.4, — is a sinusoidal fit. The top panels in (a) and (b) show a comparison between the potentials, $U(x)$, as obtained from the experiments (—) and predicted by equation 3.3 (□).

thermal equilibrium method [42, 60, 96, 97]. Note that in the original paper [105] the friction coefficient ζ was erroneously taken to be lower than the experimental value of $\zeta = 9.19 \times 10^{-8}$ kg s^{-1} used throughout this work.

Optical potential energy landscapes

The measurements are now extended to 1D potential energy landscapes generated by multiple overlapping single optical traps. This introduces additional contributions to the optical force exerted on the particle. Completely analogously to the single trap experiments, the velocity profile, $v(x)$, is used to reconstruct the potential energy landscape using equation 3.4. It is shown that once the trap stiffness k_j and well depth $U_{0,j}$ of the single optical traps are known, optical landscapes can be fully engineered and described by a simple sum of single Gaussian potentials as given by equation 3.3 [54].

First, a simple 'extended' landscape consisting of two pairs of identical optical traps is considered. Figure 3.3a shows the velocity profile $v(x)$ of a particle driven at a flow velocity of ~ 11μm s^{-1} through four optical traps separated by distances $\delta_{12} = \delta_{34} = 3$μm and $\delta_{23} = 10$μm. This arrangement is well described by four Gaussian wells (equation 3.4), exhibiting additional small peaks in between the two traps constituting the pairs, which clearly illustrates

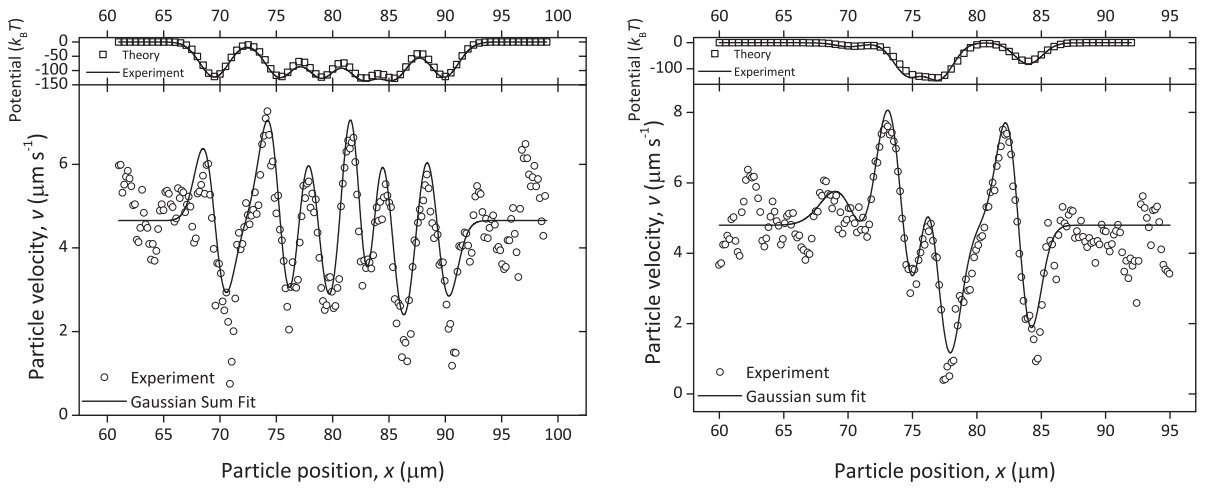


Figure 3.4: The particle velocity $v(x)$ as a function of the position x when driven at a flow velocity of ~ 5 μm s^{-1} through two different random optical landscapes: ○ experimental data, — is a fit according to equation 3.4. (a) six identical traps with random spacing. (b) four traps with random spacing, k and V_0. The top panels in (a) and (b) show a comparison between the potentials, $U(x)$, as obtained from the experiments (—) and predicted by equation 3.3 (□).

the additivity of the potentials. Fitting may be achieved using the same parameters for each trap or independent parameters: the results from both methods are found to be within 3.5% of each other. The good correlation of the reconstructed potential energy landscape to that predicted by equation 3.3 (figure 3.3a, top panel) shows that the velocity profile in figure 3.3a corresponds to two double-well potentials separated by $\delta_{23} + 0.5\,(\delta_{12} + \delta_{34}) = 13$ μm.

Next, multiple overlapping optical traps are used to produce periodic 1D potential energy landscapes. Figure 3.3b shows the result of driving a particle through four identical optical traps with a spacing of $\delta = 3$ μm. The excellent fit to equation 3.4 further corroborates the applicability of the superposition of Gaussian traps (equation 3.4). The corresponding potential energy landscape is again in good agreement with equation 3.3 (figure 3.3b, top panel). The sinusoidal character of the landscape is clearly observed in the velocity profile, and is made evident by the fit in figure 3.3b. The period and amplitude of the sinusoidal landscape may now be tuned via the spacing δ and the laser power, which in turn controls k and V_0. Note that the mean velocity of the sinusoidal fit is slightly lower than the fit based on a sum of Gaussian potentials, reflecting the fact that the particles are slightly closer to the wall due to the increased radiation pressure from overlapping traps, and consequent higher friction coefficient [64]. However, this is only a small effect, consistent with the values presented in section 2.4.1.

Finally, two random potential energy landscape are generated, consisting of overlapping

optical traps with randomly generated positions and/or intensities (figure 3.4). In figure 3.4a a landscape of six identical but randomly spaced traps is shown, and in figure 3.4b a landscape of four traps with random spacing, k and V_0. Again the good fits and close correlation of theoretical and subsequently generated experimental potentials confirm that in principle once simple optical traps are fully characterized, any sort of optical landscape can be generated in a fully predictable manner. Experimental characterization in 2D, particularly of random landscapes [59,60], would pose more of a challenge, as the particle can avoid steep increases in the potential.

3.4.2 Piezo-driven experiments

Single optical traps

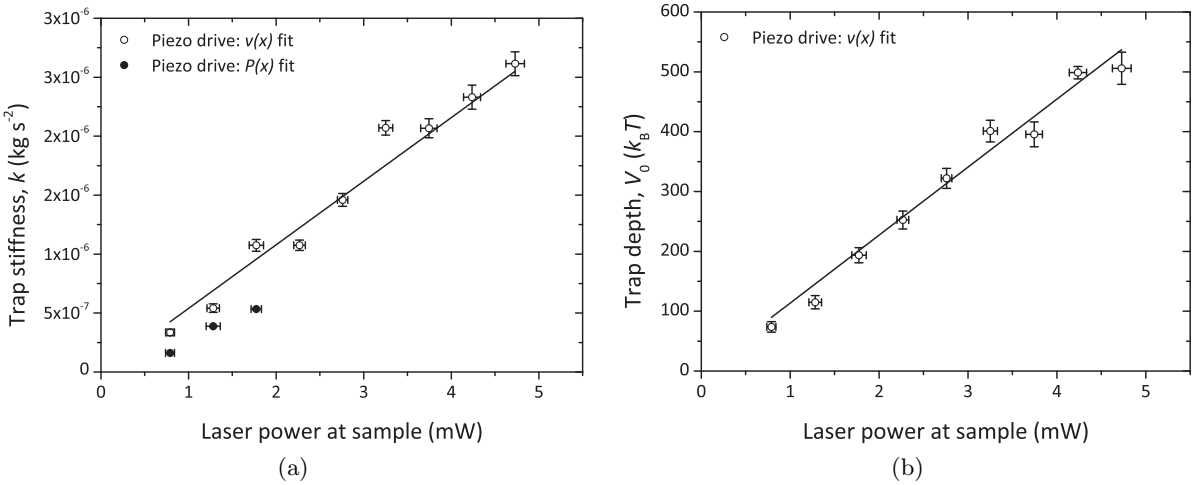


Figure 3.5: (a) The trapping stiffness k (○ piezo drive measurements; • thermal equilibrium measurements) and (b) the depth of the optical trap V_0 as a function of the laser power (○ piezo drive measurements). The solid lines are linear fits to the data.

Equivalent experiments were performed using the piezo-stage, to confirm the validity of this approach in a system with a different source of driving force. Again the particles are driven at constant velocity through single optical traps, giving trajectories ($x(t)$) and $v(x)$ plots identical in nature to those illustrated in figure 3.1. Similarly, $v(x)$ plots are fitted according to equation 3.4, to find k and V_0. Figures 3.5a and 3.5b show that again k and V_0 are found to vary linearly with laser power, and k values are close to, but slightly higher than, values calculated from the equilibrium method. The values calculated for the piezo-drive technique are slightly higher than those found by flow, but importantly the ratio between k and $V_0/k_\mathrm{B}T$ remains roughly constant, at $\sim 2 \times 10^8$. The reason for this difference is not clear, but is likely to be due to the effect of

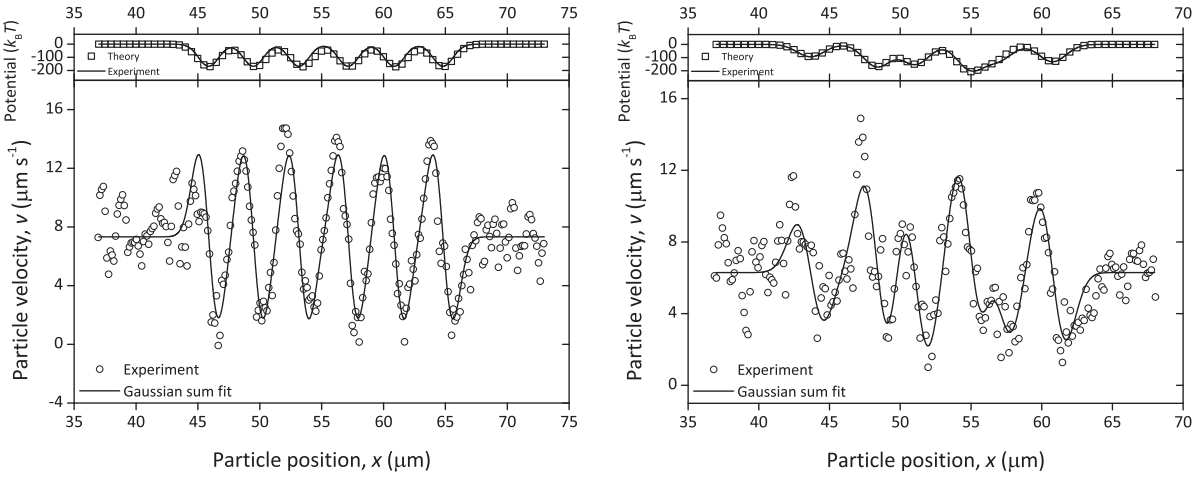


Figure 3.6: The particle velocity $v(x)$ as a function of the position x when driven at a driving velocity of ~ 6 μm s^{-1} through two different optical landscapes: ○ experimental data, — is a fit according to equation 3.4. (a) Six identical traps spaced by 4 μm. (b) Six traps with random spacing, k and V_0. The top panels in (a) and (b) show a comparison between the potentials, $U(x)$, as obtained from the experiments (—) and predicted by equation 3.3 (□).

flow against the cell wall, which is absent for piezo-drive.

Optical potential energy landscapes

Once again, experiments were performed using optical landscapes composed of multiple overlapping single optical traps. As with the flow experiments, $v(x)$ is fitted using equation 3.4, in order to find the potential energy landscape. This is then converted into an experimental measurement of the potential, $U(x)$, which is compared to a prediction from equation 3.3. Figure 3.6 shows two example landscapes. Firstly, figure 3.6a shows six traps spaced by 4 μm, which cause a regular velocity oscillation, as with the flow experiments (see figure 3.3b), and the potential oscillates regularly, confirming that the piezo-drive method produces the same results for optical landscapes as the flow driven experiments. This is the kind of potential which will be predominantly used throughout the following chapters.

Secondly, a landscape is constructed from six traps with random positions, and k and V_0, and once again the theoretical prediction of the landscape provides a good match to the experimental result. The ability of the method presented here to map and predict landscapes using different driving forces demonstrates that this is a robust and general procedure.

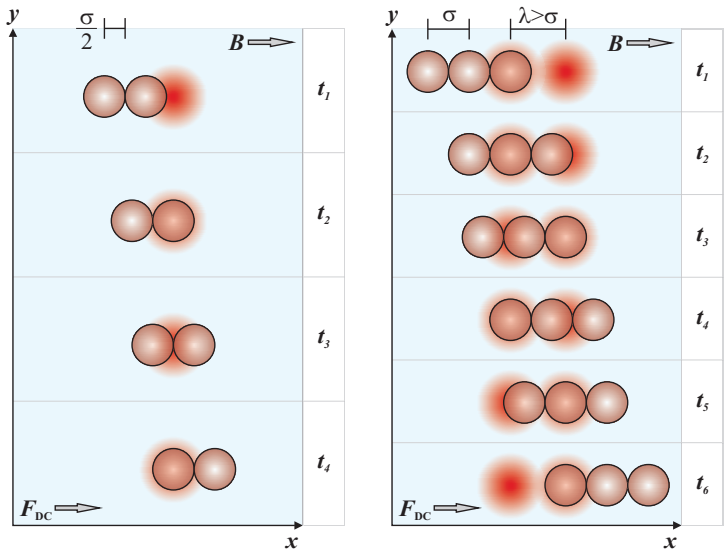


Figure 3.7: Clusters composed of multiple tightly bound particles driven through optical traps. B: magnetic field, σ: cluster spacing, λ: trap spacing. (a) A cluster of two particles is driven through a single trap: t_1 only one particle feels the trap, t_2 one particle is in the trap centre, second particle feels trap, t_3 both particles feel the trap equally, t_4 the second particle is in the trap centre. (b) A cluster of three particles is driven through two adjacent traps: t_1 cluster enters first trap, t_2 to t_5 all three particles feel the traps, t_6 the cluster leaves the traps.

Multi-particle clusters

Clusters composed of multiple tightly bound spherical particles will have a different experience of the optical potential energy landscape. Figure 3.7 illustrates the added complexity when driving small clusters through multiple optical traps. Firstly, two particles are shown moving through a single trap (panel (a)). Neglecting the scattered light, initially (t_1) only one particle feels the trap's influence. By the time the first particle is in the centre of the trap (t_2), however, the second particle is already within its influence, and when the object is centred on the landscape (t_3), both particles are equally within the trap. The situation is then symmetrically reversed as the object leaves the trap (t_4). The situation is similar for three particles passing through two traps (panel (b)). Here the object reaches the landscape at t_1, but it is not until t_2 that all of the particles are directly influenced by the trap. Each particle centre passes each trap in turn (t_3 to t_5), until the object leaves the landscape (t_6). Again this is a symmetrical process.

In order to model the passage of these clusters through an optical potential energy landscape, the equation of motion for the cluster is expressed in terms of a sum of the optical force

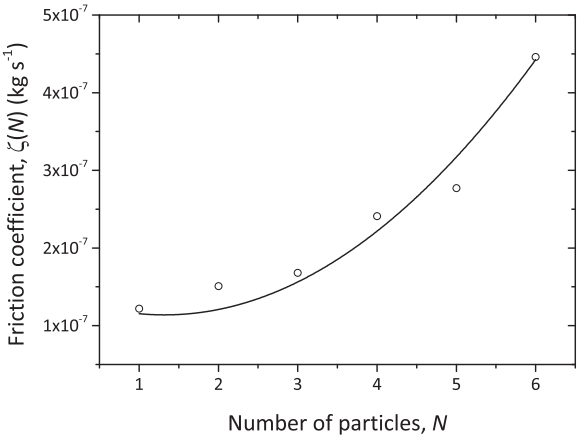


Figure 3.8: The measured coefficient of friction in x for tightly bound clusters of $N = 1$ to 6 particles, freely diffusing. The line is intended only as a guide for the eye.

acting on each individual particle:

$$v_{\text{Cluster}}(x, N) = \frac{1}{\zeta_{\text{Cluster}}(N)} \left(F_{\text{DC,Cluster}}(N) + \sum_{j=1}^{N} F_{\text{T}}(x_j) \right), \tag{3.5}$$

where x is the centre of a cluster containing N particles. The periodic optical potential energy landscapes used here consist of the sum of M identical, evenly spaced, Gaussian optical traps (see equation 3.3). Therefore equation 3.5 becomes:

$$v_{\text{Cluster}}(x, N) = \frac{1}{\zeta_{\text{Cluster}}(N)} \left(F_{\text{DC,Cluster}}(N) - \sum_{j=1}^{N} \sum_{i=1}^{M} k(x_j - x_i) \exp\left[-\frac{k(x_j - x_i)^2}{2V_0} \right] \right), \tag{3.6}$$

where x_j is the position of particle j, and x_i is the centre of trap i. The trap stiffness, k, and potential depth, V_0, are the same for all traps. As clusters contain multiple particles, their friction will not be the same as that of a single particle. The dependence of cluster friction, ζ_{Cluster}, on the number of particles in the chain is not intuitively obvious, as it may depend on a number of factors, including hydrodynamics and chain flexibility. As with the single particle friction, however, it may be obtained from mean squared displacements (see section 2.1). Here only movement along the chain axis is considered, such that $\langle x(t)^2 \rangle = 2Dt$. Figure 3.8 shows the friction coefficient found for clusters of $N = 1$ to 6 particles. The friction coefficient increases monotonically with the number of particles, although the functional dependence of ζ_{Cluster} on N cannot be established for these small N. The consequence of the increased friction is that the force felt by the cluster, $F_{\text{DC,Cluster}}$, will also be higher, because the driving velocity, $v_{\text{DC}} = F_{\text{DC,Cluster}}/\zeta_{\text{Cluster}}$, is externally imposed. It is not possible to know exactly what the

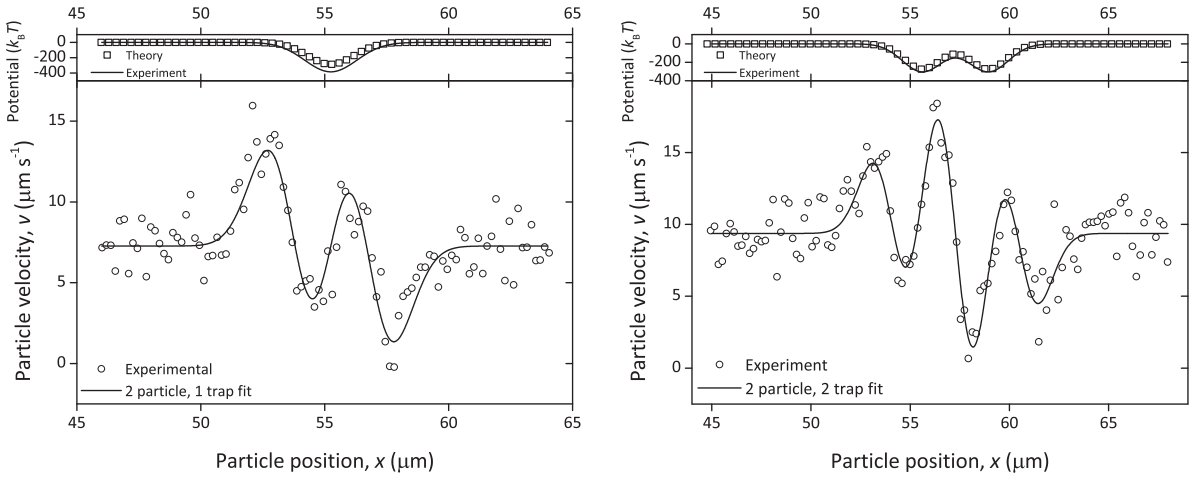


Figure 3.9: Velocity profiles and derived potential landscapes obtained by passing a cluster of two identical particles through one or two optical traps. ○ experimental data; — fit according to equation 3.7; — (top panel) potential derived from experiment. (a) Two particle cluster passing through a single optical trap. (b) Two particle cluster passing through two optical traps spaced by $\lambda = 4$ μm.

friction and force felt by individual particles within the chain is, although their ratio will be constant, as the velocity of every particle is the same as the velocity of the cluster.

The result of fitting a velocity profile with equation 3.6 is that each particle within the cluster experiences a potential energy landscape. The actual potential energy landscape being scanned by the cluster as a whole is the *sum* of these individual particle potential energy landscapes. This means that the landscape seen by the cluster as a whole is the same as that determined by a single particle, even though the velocity profile of the cluster is different to that for a single particle velocity profile.

In the case of clusters, two length scales appear in the system: that of the separation between the particles, $\sigma = 2a$, and that determined by the difference between trap positions, $\lambda = x_i - x_{i-1}$ (see figure 3.7). Taking this with equation 3.6 leads to an expression for a cluster of two tightly bound particles moving across an optical potential energy landscape composed of M identical optical traps:

$$v_{\text{Cluster}}(x, N=2) = v_{\text{DC}} - \frac{k}{\zeta(N=2)}\left(\sum_{i=1}^{M}\left(x - \frac{\sigma}{2} - x_i\right)\exp\left[-\frac{k(x-\frac{\sigma}{2}-x_i)^2}{2V_0}\right] + \sum_{i=1}^{M}\left(x + \frac{\sigma}{2} - x_i\right)\exp\left[-\frac{k(x+\frac{\sigma}{2}-x_i)^2}{2V_0}\right]\right), \tag{3.7}$$

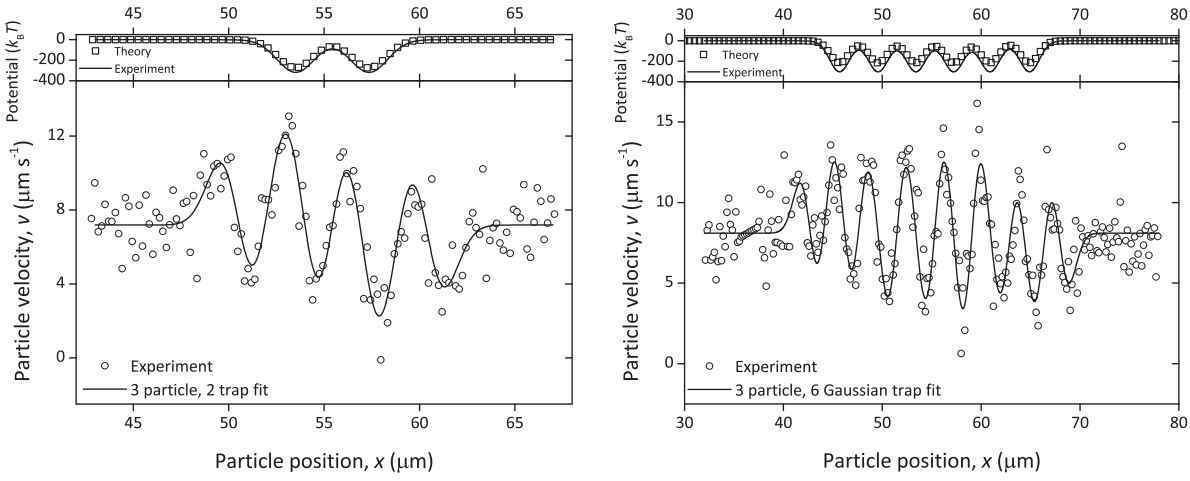


Figure 3.10: Velocity profiles and derived potential landscapes obtained by passing a cluster of three identical particles through two or six optical traps. ○ experimental data; — fit according to equation 3.8; — (top panel) potential derived from experiment. (a) Three particle cluster passing through two optical traps spaced by $\lambda = 4$ μm. (b) Three particle cluster passing through six optical traps spaced by $\lambda = 4$ μm.

where x is the cluster centre. A similar expression may be written for three particles:

$$v_{\mathrm{Cluster}}(x, N=3) = v_{\mathrm{DC}} - \frac{k}{\zeta(N=3)}\left(\sum_{i=1}^{M}(x-x_i)\exp\left[-\frac{k(x-x_i)^2}{2V_0}\right] + \sum_{i=1}^{M}(x-\sigma-x_i)\exp\left[-\frac{k(x-\sigma-x_i)^2}{2V_0}\right] + \sum_{i=1}^{M}(x+\sigma-x_i)\exp\left[-\frac{k(x+\sigma-x_i)^2}{2V_0}\right]\right), \tag{3.8}$$

In order to test the expressions above, two or three particles held together by a magnetic field of 0.8 mT, $\Gamma \approx 400$ (see section 2.2.3), are driven using the piezo-stage through sinusoidal landscapes composed of between one and six traps. Figure 3.9a shows the velocity of a two particle cluster passing through a single trap. As expected, this resembles the case of a single particle passing two traps (see figure 3.3a). The trapping parameters recovered by fitting velocity data with equation 3.7 are the same as those of a single trap. Likewise, figure 3.9b shows the velocity of a pair of particles passing through a pair of traps.

Figure 3.10 shows similar behaviour for clusters of three particles. The velocity profile for such a cluster passing two traps (figure 3.10a) is clearly different to that for two particles (figure 3.9b), but the parameters of the recovered potential are still close to the single particle prediction. The velocity profile of the cluster passing six traps (figure 3.10b) varies in amplitude,

as different numbers of particles interact with the potential landscape at different points. The potential energy landscape found in figure 3.10b is deeper than predicted. This is most likely due to the effect of scattering, which will increase with the numbers of particles and traps.

3.5 Conclusions

One-dimensional optical potential energy landscapes have been generated using optical traps controlled by acousto-optical deflectors. Colloidal particles are driven through the optical landscapes by solvent flow or piezo stage. The full optical potential energy of both single optical traps and complex landscapes composed of multiple overlapping traps is determined by a simple force balance argument. This method is simple and straightforward to implement, allowing for fast and reliable characterization of optical landscapes.

It has been found that the potential of a single optical trap is Gaussian. The magnitude of the trap stiffness and its linear dependence on laser power has been found to be consistent with those found from thermal equilibrium methods. The depth of the optical trap has also been directly obtained, and shown to be linear with the laser power. Subsequently, various optical landscapes ranging from double-well potentials to random landscapes have been generated from individually controlled optical traps. The corresponding energy landscapes as obtained from the velocity profiles are well described by a sum of single Gaussian optical traps. The more general nature of the process is illustrated by using clusters composed of multiple tightly bound particles, which show more complex velocity profiles, but allow potential profiles identical to those found by single spherical particles to be obtained. This in principle allows the fully controlled engineering of any sort of optical potential energy landscape, and this technique may well be of interest for applications in micro-fluidic devices.

Acknowledgements

This work was performed in collaboration with Rut Besseling and Dirk Aarts [105]. Thomas Skinner, Arran Curran and Samantha Ivell are thanked for useful discussions; Rut Besseling is thanked for inspiring this work; Dirk Aarts is additionally thanked for the loan of the micro-fluidics pump.

Chapter 4

Colloidal particles driven across periodic optical potential energy landscapes

Abstract

This chapter describes the motion of colloidal particles driven by a constant force over a periodic optical potential energy landscape. Firstly, the average particle velocity is found as a function of the driving velocity and the wavelength of the optical potential energy landscape. The relationship between average particle velocity and driving velocity is found to be well described by a theoretical model treating the landscape as sinusoidal, but only at low trap spacings. At higher trap spacings, a more complicated, non-sinusoidal, model must be used. Subsequently, the critical velocity required for a particle to move across the landscape is determined as a function of the wavelength of the landscape. Finally, the velocity of a particle driven at a velocity far exceeding the critical driving velocity is examined. Both of these results are again well described by the two theoretical routes, for small and large trap spacings respectively. Brownian motion is found to have a significant effect on the critical driving velocity, but a negligible effect when the driving velocity is high.

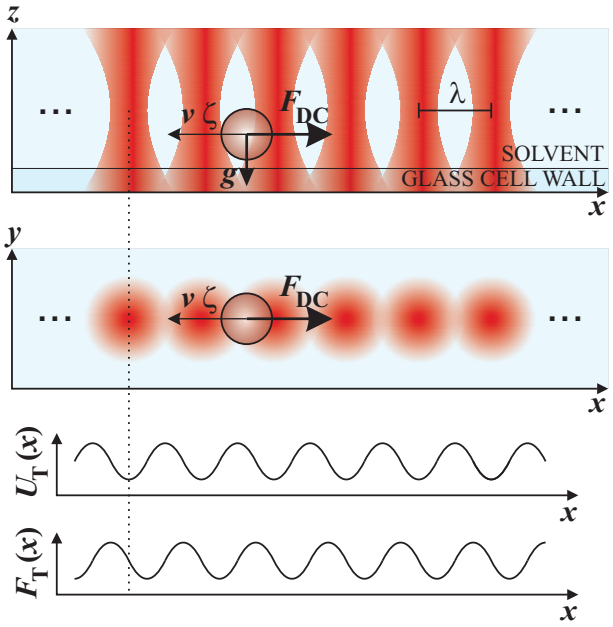


Figure 4.1: Periodic optical potential energy landscape. Spherical colloidal particle travelling across a 'washboard' potential created from AOD-timeshared focused laser spots.

4.1 Introduction

The phenomenon of a particle travelling over a one-dimensional potential energy landscape is important to the behaviour of many physical systems of scientific interest and technological importance. This includes the diverse cases of counter-sliding rough surfaces [106], the movement of adatoms on atomic surfaces [107], and the motion of mobile rings on a poly-rotaxane [108]. Of particular current relevance are superconductor effects, such as DC driven Josephson junctions [109,110], vortex motion [111–113], and charge density waves [114]. Such systems are, however, still challenging to image [5,89,115], making microscopic scale motion difficult to study at easily accessible temperatures and pressures. Extensive work using computer simulation has been conducted in this area [116–118]. There is therefore a requirement for model systems in which it is possible to examine behaviour in real space.

The case of vortices in type-II superconductors is the easiest to visualize: magnetic field penetration is permitted in these materials through 'fluxons', which are essentially non-superconducting holes punched in the super-current, around which a super-current circulates [111]. Sufficiently high magnetic field creates a high density of these repulsive vortices, which then arrange into lattices [119]. The motion of a mobile vortex through a pinned vortex channel may be modelled as a particle moving over a periodic potential energy landscape [120, 121].

Vortices may be directly imaged by techniques including Lorentz microscopy [122] or Bitter decoration [115], but neither of these techniques gives direct, controllable, access to microscopic motion in readily available experimental conditions.

As was described in Chapter 3, optical potential energy landscapes have been used to address numerous problems, from tribology [35, 44] to particle sorting [38, 50, 51, 54], and various techniques have been used to drive colloidal systems. The non-linearities in systems driven far from equilibrium by an external force have garnered recent interest in theory and experiment [40, 123–125]. Considerable attention has been given to the problem of colloidal particles diffusing in a periodic potential [126–128], and diffusing over threshold potentials [129]. Further to this, diffusion in a *tilted* periodic potential has been examined, with the small bias leading to anomalous transport effects [53, 130, 131], particularly giant diffusion [132, 133].

This chapter deals with the question of how Brownian particles behave when driven, and also subject to a periodic optical potential energy landscape (see Chapter 3). A simple theoretical model is established to explain the dynamics of the system, and different approximations are found to be valid over different ranges of the system parameters. The Brownian motion of the particles is taken into account, and found to have a small effect at low Péclet numbers. Both average particle velocities and critical driving velocities are studied in detail for landscapes composed of identical single optical traps at different trap spacings.

4.2 Theory

The Langevin equation is used to describe the motion of a Brownian particle driven by a constant force across a periodic potential energy landscape (see section 2.1, equation 2.8):

$$\zeta\ v(x,t) = \zeta \frac{\mathrm{d}x}{\mathrm{d}t} = F_{\mathrm{DC}} + F_{\mathrm{T}} + \xi(t), \tag{4.1}$$

where the particle velocity, v, at position x and time t depends on the driving force, F_{DC}, the force from the optical potential energy landscape, $F_{\mathrm{T}} = -\partial U_{\mathrm{T}}/\partial x$, the Brownian force, $\xi(t)$, and the friction coefficient, ζ.

To solve this differential equation it is necessary to define the optical potential energy landscape, U_{T}. As only periodic landscapes will be considered here, we assume that the landscape

extends infinitely, from trap $i = -\infty$ to trap $i = \infty$, with traps separated by a spacing of λ. As shown in Chapter 3, individual potentials (equation 3.2) are additive, so the potential landscape may be expressed as a sum:

$$U_{\mathrm{T}}(x) = \lim_{M\to\infty} \sum_{i=-M}^{M} V_i(x) = -V_0 \lim_{M\to\infty} \sum_{i=-M}^{M} \exp\left[-\frac{k(x-\lambda i)^2}{2V_0}\right], \tag{4.2}$$

which leads to an optical force, $F_{\mathrm{T}}(x) = -\partial U_{\mathrm{T}}(x)/\partial x$:

$$F_{\mathrm{T}}(x) = -k \lim_{M\to\infty} \sum_{i=-M}^{M} (x-\lambda i) \exp\left[-\frac{k(x-\lambda i)^2}{2V_0}\right] \tag{4.3}$$

The stochastic force term, $\xi(t)$, is now neglected, as the Péclet number is much higher than 1 for most driving velocities used here (see section 2.1.1). The Langevin equation (equation 4.1) thus becomes:

$$\zeta\ v(x,t) = \zeta \frac{\mathrm{d}x}{\mathrm{d}t} = F_{\mathrm{DC}} - k \lim_{M\to\infty} \sum_{i=-M}^{M} (x-\lambda i) \exp\left[-\frac{k(x-\lambda i)^2}{2V_0}\right], \tag{4.4}$$

which is the deterministic equation of motion for a colloidal particle driven by a constant force over a periodic optical potential energy landscape.

In the experiments, two main observables are considered: the average particle velocity over an integer number of wavelengths of the landscape, $\overline{v}$, and the critical driving velocity, F_{C}/ζ, required for the particle to move. Firstly we consider the average particle velocity, following reference [134]. As the landscape is known and periodic, it is only necessary to determine the time, Δt, in which the particle passes a single wavelength of the landscape, λ:

$$\Delta t = \int_0^{\Delta t} \mathrm{d}t = \int_{-\lambda/2}^{\lambda/2} \frac{\zeta}{F_{\mathrm{DC}} + F_{\mathrm{T}}(x)}\, \mathrm{d}x. \tag{4.5}$$

It therefore follows that in the deterministic regime:

$$\overline{v} = \frac{\lambda}{\Delta t} = \lambda \left(\int_{-\lambda/2}^{\lambda/2} \frac{\zeta}{F_{\mathrm{DC}} + F_{\mathrm{T}}(x)}\, \mathrm{d}x \right)^{-1}. \tag{4.6}$$

Next, the critical driving force required to cause the particle to overcome a maximum in the optical force is considered. The position of the maximum in the optical force, $x = x_*$, is

defined by:

$$\frac{\mathrm{d}F_{\mathrm{T}}(x_*)}{\mathrm{d}x} = 0 = -\frac{k}{V_0}\lim_{M\to\infty}\sum_{i=-M}^{M}\left\{\left[V_0 - k\left(x_* - \lambda i\right)^2\right]\exp\left[-\frac{k(x_* - \lambda i)^2}{2V_0}\right]\right\}, \tag{4.7}$$

so that the critical force may be stated directly, using equation 4.3:

$$F_{\mathrm{C}} = -F_{\mathrm{T}}(x_*) = k\lim_{M\to\infty}\sum_{i=-M}^{M}(x_* - \lambda i)\exp\left[-\frac{k(x_* - \lambda i)^2}{2V_0}\right] \tag{4.8}$$

Equations 4.6 and 4.8 are rigorous, but not analytically tractable. It is therefore necessary to make some approximations in the description of the optical potential energy landscape.

4.2.1 Sinusoidal landscape: small trap spacing

In Chapter 3 (figure 3.3b) it was demonstrated that if the trap spacing is sufficiently small, the velocity profile for a particle passing across the periodic potential is well described by a sinusoidal function. It is therefore asserted that for small λ, the potential may be expressed as a Fourier series of the form:

$$U_{\mathrm{T}}(x) = \frac{1}{2}a_0 + \sum_{m=1}^{\infty}\left[a_m\cos\left(\frac{2\pi mx}{\lambda}\right) + b_m\sin\left(\frac{2\pi mx}{\lambda}\right)\right]. \tag{4.9}$$

The first Fourier coefficient, a_m, is calculated to be [134]:

$$a_m = \frac{2}{\lambda}\int_{-\lambda/2}^{\lambda/2}U_{\mathrm{T}}(x)\cos\left(\frac{2\pi mx}{\lambda}\right)\mathrm{d}x = -\frac{2\sqrt{2\pi}V_0^{3/2}}{\lambda k^{1/2}}\exp\left(-\frac{2\pi^2m^2V_0}{\lambda^2k}\right). \tag{4.10}$$

The second Fourier coefficient $b_m \equiv 0$, because $U_{\mathrm{T}}(x)\sin(2\pi mx/\lambda)$ is an odd function, and the integration limits cover a single period of the landscape. Note that $a_0 = a_{m=0}$, and follows directly from equation 4.10. In the limit of small λ, the trapping potential $U_{\mathrm{T}}(x)$ may thus be rewritten in the following sinusoidal form:

$$U_{\mathrm{T}}(x) = -\frac{2\sqrt{2\pi}V_0^{3/2}}{\lambda k^{1/2}}\left[\frac{1}{2} + \sum_{m=1}^{\infty}\exp\left(-\frac{2\pi^2m^2V_0}{\lambda^2k}\right)\cos\left(\frac{2\pi mx}{\lambda}\right)\right]. \tag{4.11}$$

While λ is small, terms $m > 1$ may be neglected, and it is thus possible to express the optical potential energy landscape with a single term of the sum in equation 4.11. The trapping force

follows directly:

$$F_{\mathrm{T}}(x) = -\frac{\partial U_{\mathrm{T}}}{\partial x} \approx \frac{4\sqrt{2}(\pi V_0)^{3/2}}{\lambda^2 k^{1/2}} \exp\left(-\frac{2\pi^2 V_0}{\lambda^2 k}\right) \sin\left(\frac{2\pi x}{\lambda}\right), \tag{4.12}$$

and this result may be substituted into equation 4.6 to obtain an expression for the average particle velocity.

Next, the critical driving force, F_{C}, is found by again finding the position, $x = x_*$, at which the force from the optical potential energy landscape is at its maximum. Maximising equation 4.12 leads to the position of the highest optical force, $x_* = \lambda/4 + i\lambda$ (where $i = 0, \pm 1, \pm 2, \ldots$). Thus it is possible to find the critical force:

$$F_{\mathrm{C}} = -F_{\mathrm{T}}(x_*) = \frac{4\sqrt{2}(\pi V_0)^{3/2}}{\lambda^2 k^{1/2}} \exp\left(-\frac{2\pi^2 V_0}{\lambda^2 k}\right). \tag{4.13}$$

By comparing equations 4.12 and 4.13, it is seen that the trapping force is the product of the critical force and a sinusoidal term. Hence, the deterministic Langevin equation of motion (equation 4.4) becomes:

$$\zeta\ v = \zeta \frac{\mathrm{d}x}{\mathrm{d}t} = F_{\mathrm{DC}} - F_{\mathrm{C}} \sin\left(\frac{2\pi x}{\lambda}\right), \tag{4.14}$$

which offers a much simpler solution to the average velocity (equation 4.6). The time taken for a particle to pass one wavelength of the landscape in this case is:

$$\Delta t = \int_{-\lambda/2}^{\lambda/2} \frac{\zeta}{F_{\mathrm{DC}} + F_{\mathrm{T}}(x)}\, \mathrm{d}x = \int_{-\lambda/2}^{\lambda/2} \frac{\zeta}{F_{\mathrm{DC}} - F_{\mathrm{C}} \sin(2\pi x/\lambda)}\, \mathrm{d}x = \frac{\zeta\lambda}{\sqrt{F_{\mathrm{DC}}^2 - F_{\mathrm{C}}^2}}, \tag{4.15}$$

leading to an average particle velocity of:

$$\overline{v} = \begin{cases} 0, & \text{if } F_{\mathrm{DC}} \leq F_{\mathrm{C}}; \\ \frac{1}{\zeta}\sqrt{F_{\mathrm{DC}}^2 - F_{\mathrm{C}}^2}, & \text{if } F_{\mathrm{DC}} > F_{\mathrm{C}}. \end{cases} \tag{4.16}$$

When the driving force falls below the critical force, the particle does not slide across the landscape, but instead displaces from a minimum in the potential energy landscape by $\delta x = (\lambda/2\pi)\arcsin(F_{\mathrm{DC}}/F_{\mathrm{C}})$, up to the optical force maximum of $x_* = \lambda/4$. The results found here will be compared to experimental results for periodic optical potential energy landscapes with small trap spacings.

4.2.2 Nearest neighbour landscape: large trap spacing

Now the case of widely spaced traps is considered [134]. An approximation is made that the local optical potential may be described by one central trap and its two nearest neighbours. Taking this approach, only terms with $|i \leq 1|$ are taken from the full sum for the optical potential energy landscape (equation 4.2), leading to an expression for the optical force:

$$F_{\mathrm{T}}(x) = -\frac{\partial U_{\mathrm{T}}}{\partial x} = -k \sum_{i=-1}^{1} (x - \lambda i) \exp\left[-\frac{k(x-\lambda i)^2}{2V_0}\right]. \tag{4.17}$$

This may be substituted into equation 4.6 to find the average particle velocity numerically. In order to calculate the critical driving force for widely spaced traps, firstly the case is considered where the traps are infinitely spaced, and only a single term, where $i = 0$, is taken from the sum. The trapping force is then $F_{\mathrm{T}}^{\infty}(x) = -kx \exp[-kx^2/2V_0]$, and maximising this leads to the position of the highest optical force, $x_*^{\infty} = \sqrt{\frac{V_0}{k}}$, which in turn provides an expression for the critical driving force:

$$F_{\mathrm{C}}^{\infty} = -F_{\mathrm{T}}(x_*^{\infty}) = \sqrt{kV_0} \exp\left[-\frac{1}{2}\right]. \tag{4.18}$$

By assuming that the critical force for the nearest neighbours potential landscape ($|i \leq 1|$) is a small correction to the above expression, it has been shown that the position of the optical force maximum may be found [134]:

$$x_* = \sqrt{\frac{V_0}{k}} - \sqrt{\frac{k}{V_0}}\lambda^2 \exp\left[-\frac{k\lambda^2}{2V_0}\right]. \tag{4.19}$$

Substituting this result into equation 4.17 leads to the critical driving force:

$$F_{\mathrm{C}} = -F_{\mathrm{T}}(x_*) = k \sum_{i=-1}^{1} (x_* - \lambda i) \exp\left[-\frac{k(x_*-\lambda i)^2}{2V_0}\right], \tag{4.20}$$

which is numerically soluble. These expressions for the average velocity and the critical driving velocity will be compared to experimental measurements for periodic optical potential energy landscapes with large trap spacings.

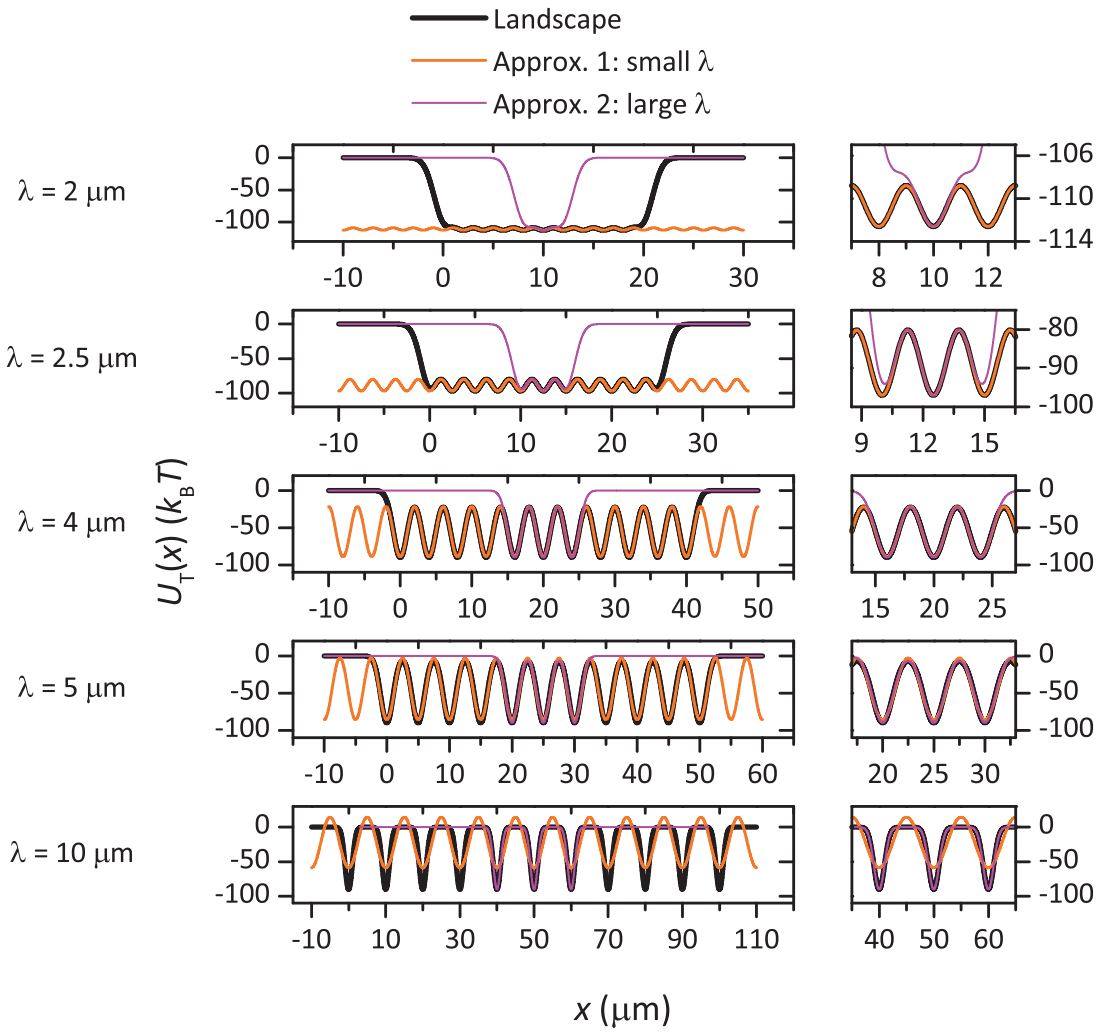


Figure 4.2: Comparison of theoretical approximations for the trapping potential $U_{\mathrm{T}}(x)$. — landscape composed of the sum of 11 individual Gaussian optical traps, at trap spacing, λ, using typical trapping parameters $k = 3.8 \times 10^{-7}$ kg s^{-2} and $V_0 = 90\ k_{\mathrm{B}}T$. — sinusoidal landscape: small λ, — nearest neighbour landscape: large λ.

4.2.3 Comparing the approximations

Figure 4.2 shows periodic optical potential energy landscapes, with trap spacings varying from 2 μm to 10 μm, comprising eleven single Gaussian traps (see equation 4.2) with typical trapping parameters of $k = 3.8 \times 10^{-7}$ kg s^{-2} and $V_0 = 90\ k_{\mathrm{B}}T$. Also shown for comparison are landscapes corresponding to the sinusoidal (small λ) and nearest neighbour (large λ) approximations. The five large panels show the full landscape for each trap spacing, and the small panels show details of these, to highlight the comparisons between the different models. Several features should be noted from the comparisons:

1. The difference between the minima and maxima in the landscape increases with trap spacing, until it is equal to the depth of a single trap, when the trap separation is very large ($\lambda = 10$ μm).

2. At very low trap spacing ($\lambda = 2$ μm), the barrier in the potential is on the order of 4 $k_{\mathrm{B}}T$, easily accessible by diffusion alone. By $\lambda = 2.5$ μm, the barrier is 20 $k_{\mathrm{B}}T$, making diffusion from one minimum to another unlikely.

3. The sinusoidal (small λ) approximation describes the full landscape very well for 2 μm $\leq \lambda \leq 4.5$ μm. Above this, both the form and depth of the potential landscape are poorly described.

4. The nearest neighbour (large λ) approximation does not describe the landscape well below $\lambda = 4$ μm, but is a very good description when $\lambda \geq 4$ μm.

4.2.4 The effect of Brownian noise

So far, a deterministic Langevin equation has been used, which is only valid at high Péclet number, Pe (see section 2.1.1). Just above the critical driving velocity, the particle velocity is very low and Pe ~ 1, so that the stochastic force term, $\xi(t)$, is of the same magnitude as the driving force, F_{DC}. In this regime, it is therefore necessary to consider the effect of Brownian motion on the particle velocity.

It has been reported that the average velocity of a particle driven over the sinusoidal landscape, with Brownian noise included, is described by [8, 134]:

$$\overline{v} = \left(\frac{2k_{\mathrm{B}}T}{\lambda\zeta}\right)\frac{\sinh(\pi D)}{I_{\mathrm{i}D}(D_{\mathrm{C}})I_{-\mathrm{i}D}(D_{\mathrm{C}})} = \left(\frac{2k_{\mathrm{B}}T}{\lambda\zeta}\right)\frac{\sinh(\pi D)}{|I_{\mathrm{i}D}(D_{\mathrm{C}})|^2}. \tag{4.21}$$

Here $I_{\mathrm{i}D}(x)$ is the modified Bessel function of the first kind, and:

$$D = \frac{F_{\mathrm{DC}}\lambda\zeta}{2\pi k_{\mathrm{B}}T}; \qquad D_{\mathrm{C}} = \frac{F_{\mathrm{C}}\lambda\zeta}{2\pi k_{\mathrm{B}}T}, \tag{4.22}$$

where F_{C} is taken from equation 4.13.

An expression for the mean velocity within the nearest neighbour approximation has also been reported [126, 134]:

$$\overline{v} = \frac{\lambda k_{\mathrm{B}} T}{\zeta} \mathcal{J}^{-1} \left(1 - \exp\left[-\frac{F_{\mathrm{DC}} \lambda}{k_{\mathrm{B}} T} \right] \right), \tag{4.23}$$

where:

$$\mathcal{J} = \int_{-\lambda/2}^{\lambda/2} \left[\exp\left[-\frac{(-x F_{\mathrm{DC}} + U_{\mathrm{T}})}{k_{\mathrm{B}} T} \right] \int_{x}^{x+\lambda} \exp\left[\frac{-x' F_{\mathrm{DC}} + U_{\mathrm{T}}}{k_{\mathrm{B}} T} \right] \mathrm{d}x' \right] \mathrm{d}x. \tag{4.24}$$

In order to determine critical driving forces from these expressions, a cut-off velocity is applied, below which the particle is said to be stationary (see section 4.3.4). The cut-off is taken to be 0.05 μm s^{-1}, as this is the maximum resolution of the experimental method for determining the critical driving velocity.

4.3 Experimental methods

4.3.1 Colloidal model system

The colloidal system used is composed of Dynabeads M-270 (diameter 3 μm), in 20% $\mathrm{EtOH_{aq}}$ (see section 2.4.1), held in a Hellma cell. The friction coefficient, ζ, is found from diffusion to be 9.19×10^{-8} kg s^{-1} (see sections 2.1 and 2.4.1). Particle concentration is low, so that only a single particle is visible in the field of view.

4.3.2 Experimental setup and parameters

The experimental setup consists of an infra-red (1064 nm) laser, controlled using a pair of perpendicular AODs, and focused using a 50×, NA=0.55 microscope objective (see section 2.4.3). One-dimensional periodic optical landscapes, with trap spacings 2.5 μm $\leq \lambda \leq$ 10 μm, are generated in Aresis Tweez software, controlled from the LabView interface. The traps are time-shared at 5 kHz, such that on the timescale of the particles (with a Brownian time of ~ 50 s, and a driven time of at least ~ $\frac{1}{3}$ s per trap spacing), the traps form a constant potential energy landscape.

The laser power and the total number of traps are held constant throughout the experiments, so that the laser power per trap (and hence the trapping parameters k and V_0) are consistent. A laser power of 350 mW is set, and 46 traps are used, corresponding to ~ 0.75 mW per trap at the sample position (see section 2.4.3). This gives typical trapping parameters for trap stiffness, $k = 3.8 \times 10^{-7}$ kg s^{-2}, and trap strength, $V_0 = 90\ k_{\mathrm{B}}T$ (see figure 3.5). The number of traps which fit in the field of view changes with trap spacing, so excess traps are positioned at the edges of the field of view, in lines parallel to the experimental landscape. These extra traps are sufficiently far away as to not influence the experiment, and have the added advantage of trapping extra particles which diffuse into the field of view.

The driving force is provided by a PI-542.2CD piezo-stage, controlled using the LabView interface (see section 2.4.5), moving at 0.05 μm s^{-1} ≤ F_{DC}/ζ ≤ 10 μm s^{-1}.

4.3.3 Average velocity experiments

Images are focused onto the Ximea CMOS camera using a 40×, NA=0.50 microscope objective. The setting of experimental parameters is automated in the LabView interface, and six repeats are made at each driving velocity for each trap spacing. Particle position is recorded live at 40 Hz from the camera image (see section 2.4.7). Average velocity is found by linearly fitting to a graph of $x(t)$, over an integer number of wavelengths of the landscape. Instantaneous velocity is found by taking the numerical derivative of the $x(t)$ data.

4.3.4 Critical velocity experiments

The driving velocity is iterated to find the critical driving velocity at which the particle starts to slide across the optical potential energy landscape, with a maximum resolution of 0.05 μm s^{-1}. A particle is said to be locked if it does not move after the stage has moved 100 μm, or three minutes has elapsed, whichever happens first. To determine the critical driving velocity from equations 4.21 and 4.23, a numerical search procedure is conducted to find the driving velocity at which the particle average velocity first exceeds the cut-off. At each trap spacing (separated by $\Delta\lambda = 0.01$ μm), the driving velocity is increased until $\overline{v}$ is found to exceed 0.05 μm s^{-1}. The results of these numerical experiments are presented and compared to experimental results in section 4.4.

4.4 Results and discussion

Results are presented from experiments in which a colloidal particle was driven across a periodic optical potential energy landscape. Figure 4.3a shows four particle trajectories with the same average velocity. These trajectories are clearly different to that for the case of no traps (see figure 2.10b), as they exhibit clear plateaus where the particle position does not increase for a period of time. Each of the four lines in figure 4.3a is driven by a different driving velocity across a periodic optical potential energy landscape with a different wavelength. This means that although the average velocities are the same, the spatial distribution of the plateaus and the velocity of the particles between the plateaus differs. The plateaus are spaced by the trap spacing, λ, as they are caused by the particle sitting in a trap for a period of time, as was seen in Chapter 3. The distribution of the times spent in a trap is a result of the stochastic force.

From the particle trajectories the velocity, $v(t)$, is obtained. Figure 4.3b shows how the velocity of the particle changes with time for the four trajectories in figure 4.3a. When the particle is sitting in a trap, its velocity is around zero. When a particle hops into the next minimum in the landscape, there is a spike in the velocity. The irregularity with which the particle hops to another trap illustrates the stochastic nature of the process, which is governed by Kramers' rate [135, 136].

Combining the y-axes of figures 4.3a and 4.3b leads to a measure of velocity as a function of position. Figure 4.3c shows $v(x)$ for the four cases shown in the previous two panels. The spacing between regions of zero velocity are now evenly spaced by λ, as expected from the periodic potential energy landscape, and the regions where the particle is stationary are roughly the same size. In the case of $\lambda = 10$ μm, when the traps are widely spaced, the particles regain the driving velocity (dashed line) after they have escaped the influence of each individual trap.

4.4.1 Average particle velocity

The first main observable from the experiments is the average velocity of a particle travelling over many wavelengths of the periodic optical potential energy landscape. Figure 4.4 shows the dependence of the average particle velocity, $\overline{v}$, on the driving velocity, F_{DC}/ζ, at a trap spacing of 3.5 μm. At low driving velocities, the particle does not move across the landscape, and an

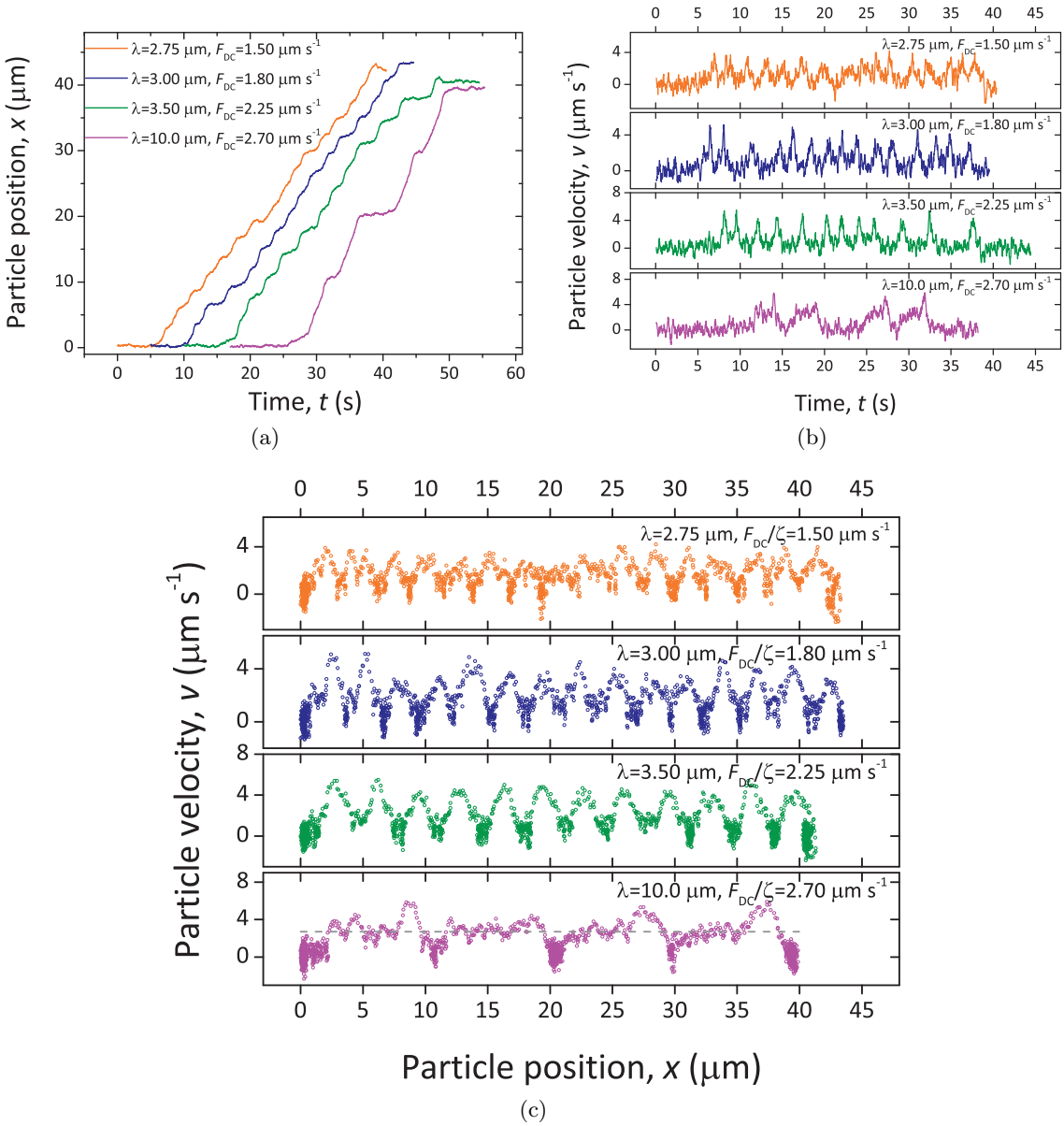


Figure 4.3: Trajectories of Brownian particles driven over a periodic potential. (a) Individual particle trajectories for cases with differing trap spacings and driving velocities, but the same average velocity. Lines are spaced in t for ease of comparison. (b) Particle velocity as a function of time for the four trajectories in (a). (c) Particle velocity as a function of position, for the four trajectories in (a). The dashed line in the bottom panel is at $v = 2.7$ μm s^{-1}

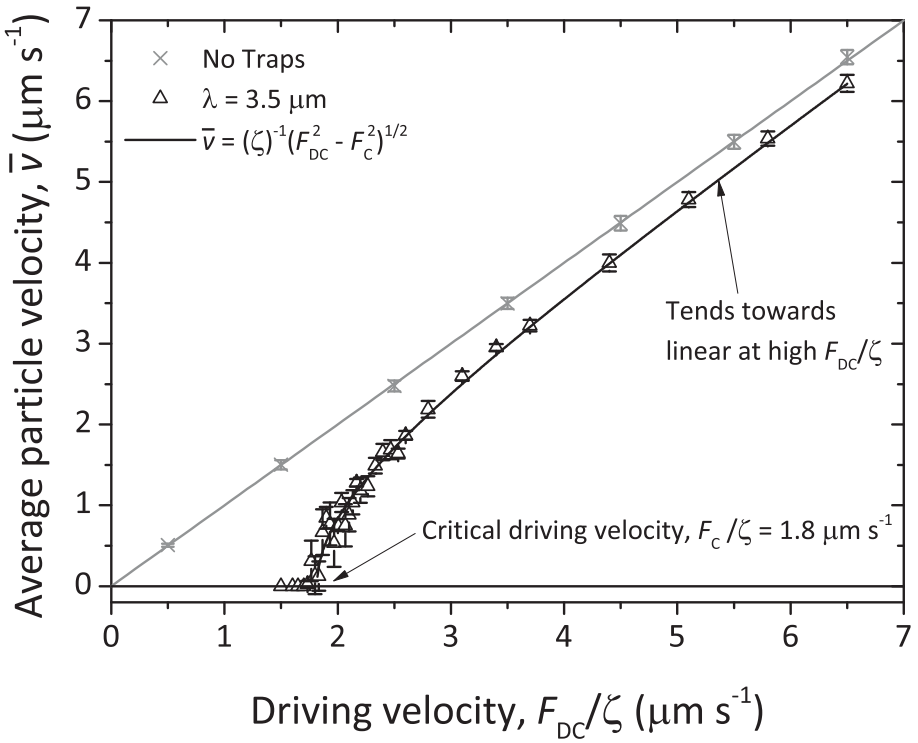


Figure 4.4: Average particle velocity against driving velocity for λ = 3.5 μm, compared to the case of no traps. △ experimental data (error bars represent the standard deviation of the repeats). — fit corresponding to a sinusoidal optical potential energy landscape, $\zeta\overline{v} = \sqrt{F_{\mathrm{DC}}^2 - F_{\mathrm{C}}^2}$ with fitting parameter F_{C}. –×– no traps (see figure 2.10a).

average velocity of 0 is recorded. The driving force then reaches a critical value, $F_{\mathrm{DC}} = F_{\mathrm{C}}$, after which the average particle velocity rises sharply, before the gradient decreases, and ends roughly collinear to the line for the case of no traps (from figure 2.10a). The average velocity will always be lower than the case of no traps, due to the time the particle spends sitting in each trap (see figure 4.3).

The experimental data are fitted with the deterministic expression for the average velocity for a particle driven over a sinusoidal potential energy landscape, $\zeta\overline{v} = \sqrt{F_{\mathrm{DC}}^2 - F_{\mathrm{C}}^2}$ (equation 4.16), which describes the data well, and finds a deterministic critical driving velocity of 1.8 μm s^{-1}.

Next, the dependence of the average particle velocity on the driving velocity for different trap spacing is considered. Figure 4.5 shows the mean particle velocity as a function of driving velocity for six trap spacings, from λ = 2.5 μm to λ = 10 μm. All of the experimental lines show the same shape, but remain below the no trap line. The critical driving velocity increases with λ, which is discussed further in section 4.4.2. Each data set is fitted with equation 4.16, which

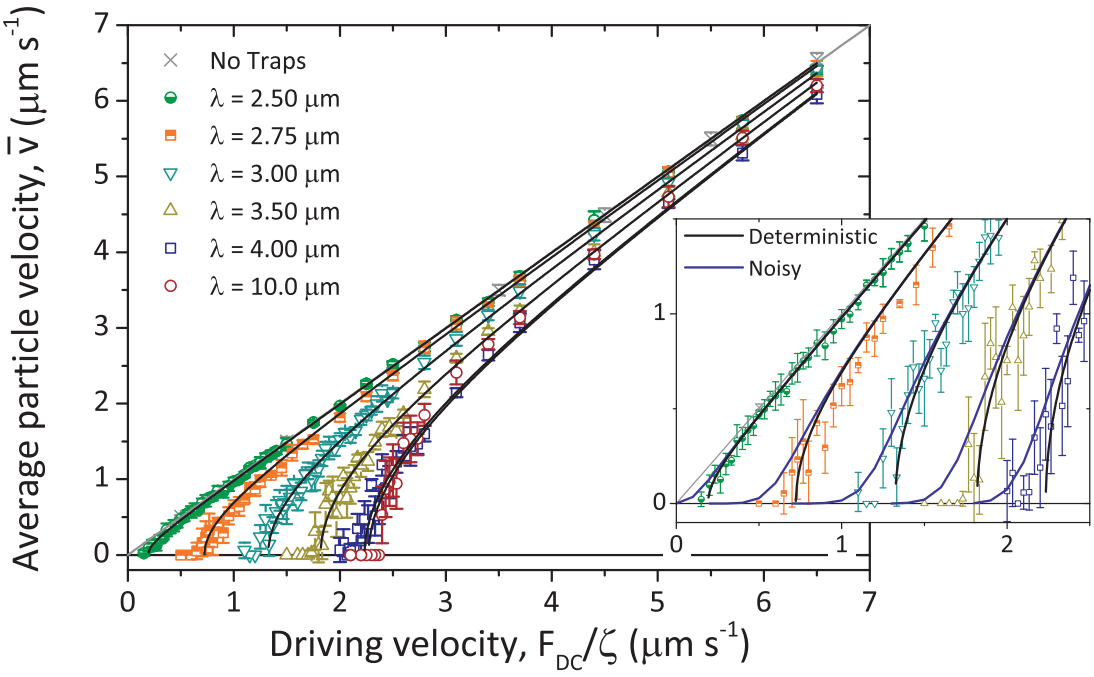


Figure 4.5: Average particle velocity against driving velocity for varying trap spacing. ⊖, ⊟, ▽, △, □, ○ experimental data (error bars represent the standard deviation of the repeats). — fit corresponding to a sinusoidal optical potential energy landscape, $\zeta\overline{v} = \sqrt{F_{DC}^2 - F_C^2}$, with fitting parameter F_C. –×– no traps (see figure 2.10a). Inset: the effect of Brownian noise on particle velocity close to the critical driving velocity. — numerical solutions for a Brownian particle driven over a sinusoidal optical potential energy landscape (equation 4.21).

describes the average velocity of a particle driven over a sinusoidal optical potential energy landscape in the absence of noise. This fit is accurate up to λ = 4 μm, but fits less well at λ = 10 μm. This is expected, as the sinusoidal nature of the potential energy landscape only holds for small trap spacing (see figure 4.2). At high driving velocity, there is a decrease in average velocity as trap spacing increases. This is due to the time the particle spends in each trap, which increases with trap spacing due to the increase in the critical force. This is discussed further in section 4.4.3.

The behaviour at low driving velocity is less well described by the deterministic equation. The inset in figure 4.5 shows the lower parts of the curves for λ = 2.5 μm to λ = 4 μm from the main panel, with the previously described fits and numerical solutions to the stochastic Langevin equation (equation 4.21) for a sinusoidal optical potential energy landscape. The effect of Brownian noise is only noticeable at very low average velocity, where it manifests as a small deviation from the deterministic velocity, caused by Kramers' hopping [135, 136]. These fits using equation 4.21 show excellent agreement with the data at low F_{DC}/ζ.

4.4.2 Critical driving velocity

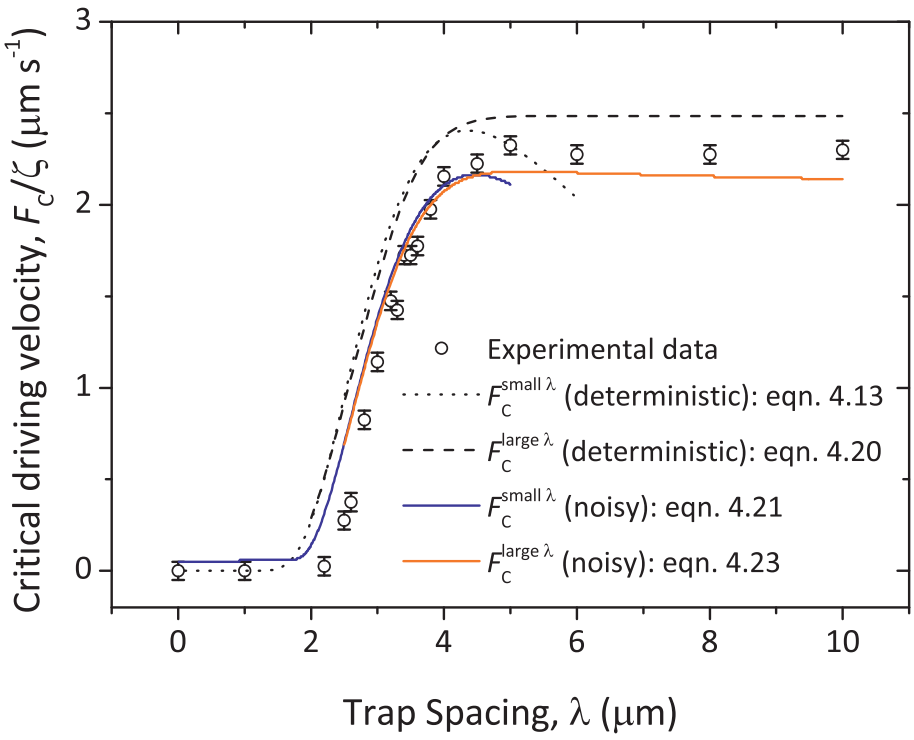


Figure 4.6: Critical driving velocity as a function of trap spacing. ○ experimental data (error bars represent experimental uncertainty). Lines are theoretical predictions. Sinusoidal potential energy landscape: ····· deterministic force (equation 4.13); — stochastic force (equation 4.21). Nearest neighbour landscape: - - - deterministic force (equation 4.20), — stochastic force (equation 4.23).

Now the dependence of the critical driving velocity on the trap spacing is considered in more detail, and compared to theoretical predictions excluding and including Brownian noise. The experimental data shown in figure 4.6 show the critical driving velocity as a function of the trap spacing. It is observed that at small trap spacings there is essentially no critical driving velocity, as the height of the barriers between the minima in the periodic optical potential energy landscape are on the order of a few k_BT, and the particle is able to diffuse across the landscape (see figure 4.2). At $\lambda \approx 2$ μm, the critical driving velocity increases sharply, until it plateaus at $\lambda \approx 5$ μm, with a value of $F_C/\zeta = 2.3$ μm s^{-1}, when the critical driving force becomes the force required to escape a single isolated Gaussian trap.

Four theoretical predictions are plotted on figure 4.6. Firstly, the dotted line and the dashed line show the deterministic solutions for the small λ case (equation 4.13) and the large λ case (equation 4.20) respectively. The deterministic expression for a sinusoidal landscape (small λ) is effective from $\lambda = 0$ to $\lambda \approx 4.5$ μm, which overlaps significantly with the effective range of

the nearest neighbour landscape (large λ). These deterministic theoretical predictions generally follow the same trend as the experimental data, but the critical driving velocity increases from zero at too low a trap spacing, and the plateau lies at too high a value of F_C. This is because around the critical driving velocity the Péclet number is on the order of 1, making the effect of Brownian motion important.

The solutions including Brownian noise for the small λ case (from equation 4.21) and the large λ case (from equation 4.23) are also shown in figure 4.6. These numerical solutions show the same trends as the deterministic lines, but have lower values. This is expected, as the inset on figure 4.5 showed that the effect of the stochastic force term is to increase the particle average velocity at driving forces close to the critical driving force.

4.4.3 Driving velocity far above the critical driving velocity

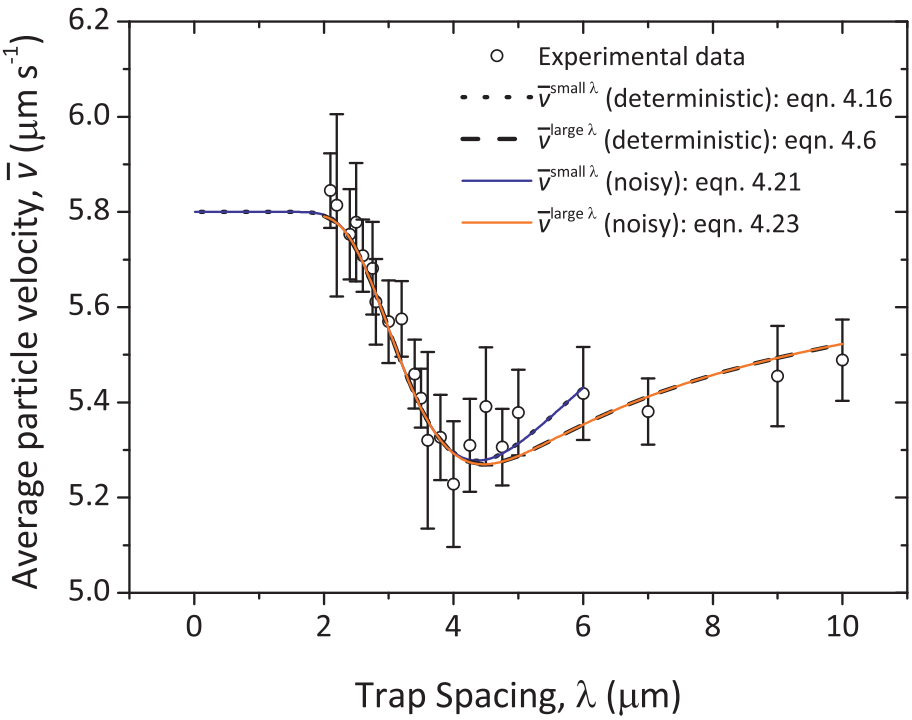


Figure 4.7: Effect of the trap spacing on the average velocity of a particle at a constant driving velocity of 5.8 μm s^{-1}. ○ experimental data (error bars represent the standard deviation of the repeats). Sinusoidal potential energy landscape: ··· deterministic force (equation 4.16), — stochastic force (equation 4.21). Nearest neighbour landscape: - - - deterministic force (equation 4.6), — stochastic force (equation 4.23).

When the particle is driven by a velocity well in excess of the critical driving velocity, the effect of the trap spacing on the average particle velocity is a result of the amount of time the particle is delayed by sitting in each trap (see figure 4.5). Figure 4.7 shows this effect more

clearly by plotting the average particle velocity against the trap spacing. The experimental data show that velocity markedly decreases between λ = 2 μm and λ = 4 μm, before gradually increasing again.

Again, four theoretical predictions are plotted on figure 4.7. The deterministic solutions for the small λ case (equation 4.16) and the large λ case (equation 4.6) are show along with the noisy solutions (small λ: equation 4.21, large λ: equation 4.23). Here there is no difference between the predictions from the deterministic and noisy cases. This is expected, as for high F_{DC} the Péclet number is high, making Brownian noise unimportant.

Again the small λ approximation works up to $\lambda \approx 4$ μm, and the large λ approximation works above $\lambda \approx 2.5$ μm, consistent with figure 4.6. The initial rapid decrease in $\overline{v}$ as λ increases is due to the increased time the particle sits in each trap, due to the increased potential barrier. $\overline{v}$ then increases as traps no longer overlap, and the time spent *between* traps takes over, bringing the average velocity back up towards the driving velocity.

4.5 Conclusions

The behaviour of Brownian particles driven by a constant force through quasi-one-dimensional periodic optical potential energy landscapes has been studied by optical microscopy. Firstly, the average velocity of a particle as a function of the driving velocity has been studied. A critical driving velocity is seen, below which the particle is pinned to the potential energy landscape, and above which the particle slides, with an average velocity that increases non-linearly with the driving velocity. The average particle velocity has been studied for potential energy landscapes with a range of trap spacings or wavelengths, and the critical driving velocity has been found to depend on the wavelength.

At small trap spacings, the critical driving velocity is very low, and it then increases, until it reaches a plateau when the individual traps are fully separated. At driving velocities far in excess of the critical driving velocity the average particle velocity is also found to depend on the landscape wavelength. At small trap spacings, increasing the landscape wavelength reduces the average particle velocity, as the minima in the potential become deeper, thus delaying the particle for longer in each trap. At larger trap spacings, average particle velocity increases again,

as the traps become fully separated, and the particle velocity is determined by the time spent between the minima in the potential.

Theoretical predictions have been made for the average particle velocity and the critical driving velocity. Predictions have been made corresponding to two different approximations describing the optical potential energy landscape. When trap spacing is small, the landscape is treated as sinusoidal. When trap spacing is large, it is treated as a sum of three individual Gaussian traps. These approximations have been broadened to include the effect of Brownian noise.

The trend for the average particle velocity as a function of driving velocity and trap spacing has been shown to very accurately match the theoretical prediction from the small trap spacing approximation, up to a limiting trap spacing. Including the effect of Brownian noise allows average particle velocity at driving velocities close to the critical driving velocity to be more accurately predicted. Critical driving velocities are also found to agree well with the theoretical predictions, especially once the effect of Brownian noise has been taken into account. At higher driving forces, however, it has been shown that the deterministic solutions alone provide an adequate description.

Acknowledgements

This work was done in collaboration with Arthur Straube, Rut Besseling, and Dirk Aarts. Alice Thorneywork and Samantha Ivell are thanked for useful discussions.

Chapter 5

Dynamic mode locking in a driven colloidal system

Abstract

This chapter examines the dynamics of a Brownian colloidal particle driven by a modulated force over a sinusoidal optical potential energy landscape. The frequency of the modulated drive competes with the natural frequency of particle motion over the periodic landscape. Coupling between the competing frequencies leads to synchronisation of particle motion into discrete dynamic modes. This synchronisation manifests as a 'Devil's staircase' of mode locked steps in the average particle velocity as a function of driving velocity. The amplitude and frequency dependence of the step width and critical driving velocity of the mode locked staircase are studied, and good qualitative agreement is found with theory. Furthermore, particle trajectories for locked and unlocked states are examined and a clear difference in behaviour is found. Phase portraits show locked (unlocked) states as closed (open) loops in phase space. A state diagram of mode locked steps is constructed, and phase portraits of the modes are shown.

5.1 Introduction

Synchronisation is one of the most diverse fundamental physical phenomena [137]. From Huygens' pendulum clocks 350 years ago [138,139] to fireflies [140], hairs of the inner ear [141], clapping crowds [142,143], and the circadian rhythms of animals [144], frequency entrainment occurs all over the natural and technological world. The phenomenon results when a weak coupling force between competing oscillators causes their rhythms to adjust to match each other [140]. Synchronisation on the micro-scale is of huge technological importance, as the decreasing size of electronic and mechanical systems demands ever-smaller frequency references [145]. Recent developments include electromechanical [146,147] and optomechanical oscillators [148,149], but such systems are limited in their scalability [149].

One such synchronisation phenomenon is *dynamic mode locking*, which occurs when systems with a natural internal frequency are driven by an external modulation. Competition between the two frequencies leads to coupling between the oscillations, causing the system to synchronise into repeating modes of motion. Much effort has been put into the understanding of dynamic mode locking in superconductor vortex lattices [6, 112, 118, 150, 151], but the difficulty in visualising such systems makes model systems necessary [152]. Other systems showing such resonance behaviour include Josephson junctions [153–155] and driven adatoms on atomic surfaces [107, 156]. The AC Josephson effect occurs at a thin insulated superconductor junction [109], where the current caused by the tunnelling of Cooper pairs is equivalent to a particle moving over a periodic potential landscape, due to the phase difference between the two sides of the barrier [157]. Driving the junction with an AC current causes regions to appear where the resistance of the system does not increase with increased DC current [109, 155]. The shape of the resulting graph is known as 'Shapiro Steps'. Charge density waves are another technologically significant system demonstrating dynamic mode locking, and have been extensively studied experimentally and numerically [5, 114, 158].

Model systems composed of colloidal particles in periodic potentials have been studied for a number of years [37, 40], from simple double well potentials [95–97, 159] to directed motion [46, 160–163] and particle sorting [35, 164] in two dimensional optical lattices. Their inherent time and length scales and ease of manipulation make colloidal systems attractive models for the study of such phenomena at the microscopic scale. Noise in Brownian systems has been

found in theory to induce anomalous diffusion [130] and stochastic resonance [165–167], and rocking-ratchet like potentials have been used in optical and magnetic systems [168, 169]. The possibility of resonance has also been explored in systems with feedback [170] and random pinning potentials [171]. Recent work studied the transport properties of a system of super-paramagnetic colloidal particles driven on a magnetic film by a rotating magnetic field [172].

Here, a system of Brownian colloidal particles is driven over a sinusoidal optical potential energy landscape by a driving force consisting of a constant and a modulated part. The natural frequency of the particle driven over the optical potential energy landscape by the DC component of the force couples to the frequency of the AC component of the driving force. Firstly it is shown that this coupling leads to dynamic mode locking steps in the system, and then the frequency and amplitude dependence of their step widths and critical forces is analysed. Individual particle trajectories are analysed, and the differences between particle dynamics on locked steps and the unlocked regions between them are identified through phase portraits, with the range of dynamic modes displayed in a state diagram.

5.2 Theory

To describe a Brownian particle driven by the sum of a constant and a modulated force across a periodic optical potential energy landscape (see section 2.1, equation 2.8), the Langevin equation is now written as:

$$\zeta\ v(x,t) = \zeta \frac{\mathrm{d}x}{\mathrm{d}t} = F_{\mathrm{DC}} + F_{\mathrm{mod}}(t) + F_{\mathrm{T}} + \xi(t), \tag{5.1}$$

where the particle velocity, v, at position x and time t depends on the force from the optical potential energy landscape, F_{T}, the Brownian force, $\xi(t)$, the constant driving force, F_{DC}, the friction coefficient, ζ, and the oscillating driving force,

$$F_{\mathrm{mod}}(t) = F_{\mathrm{AC}} \cos(\omega t)\,. \tag{5.2}$$

Here, F_{AC} is the amplitude of the modulated driving force, and $\omega = 2\pi\nu$ is the angular frequency, where ν is the frequency of the applied oscillation. The optical potential energy landscape,

$U_{\mathrm{T}}(x)$, is taken to be sinusoidal, as described in section 4.2.1:

$$U_{\mathrm{T}}(x) = -\frac{2\sqrt{2\pi}V_0^{3/2}}{\lambda k^{1/2}}\left[\frac{1}{2} + \exp\left(-\frac{2\pi^2 V_0}{\lambda^2 k}\right)\cos\left(\frac{2\pi x}{\lambda}\right)\right], \tag{5.3}$$

which leads to an optical force (see section 4.2.1):

$$F_{\mathrm{T}} = -\frac{\partial U_{\mathrm{T}}}{\partial x} = -F_{\mathrm{C}}\sin\left(\frac{2\pi x}{\lambda}\right). \tag{5.4}$$

The critical driving force, F_{C}, is given by equation 4.13:

$$F_{\mathrm{C}} = \frac{4\sqrt{2}(\pi V_0)^{3/2}}{\lambda^2 k^{1/2}}\exp\left(-\frac{2\pi^2 V_0}{\lambda^2 k}\right). \tag{5.5}$$

Thus, the full equation of motion for a particle driven by DC and AC driving forces over a sinusoidal optical potential energy landscape is given by:

$$\zeta\ v(x,t) = \zeta\ \frac{\mathrm{d}x(t)}{\mathrm{d}t} = F_{\mathrm{DC}} + F_{\mathrm{AC}}\cos(2\pi\nu t) - F_{\mathrm{C}}\sin\left(\frac{2\pi x}{\lambda}\right) + \xi(t). \tag{5.6}$$

Note that the critical driving force, F_{C}, is a property of the landscape (equation 5.5), and is equal to the DC critical driving force found in Chapter 4. As the total driving force in equation 5.6 is a sum of the DC and time dependent AC contributions, the critical DC driving force required to overcome pinning depends on the amplitude and frequency of the modulated component of the driving force.

5.2.1 The 'high frequency' regime

While equation 5.6 is not analytically soluble, useful insight can be obtained in the limit of high frequency. In order to solve equation 5.6 for a certain range of driving frequencies, the work of Cotteverte et al. [173], Chow et al. [174], and Reichhardt et al. [175] is followed. Results obtained in these previous works are expressed in the variables used in this work [176]. The first step in solving equation 5.6 is to split the particle trajectory, $x(t)$, into a 'linear' part containing the terms not dependent on $x(t)$, and a 'non-linear' deviation from the linear part, containing terms dependent on $x(t)$:

$$x(t) = x_{\mathrm{lin}}(t) + \delta(t), \quad \text{such that} \quad \frac{\mathrm{d}x(t)}{\mathrm{d}t} = \frac{\mathrm{d}x_{\mathrm{lin}}(t)}{\mathrm{d}t} + \frac{\mathrm{d}\delta(t)}{\mathrm{d}t}, \tag{5.7}$$

where $x_{\mathrm{lin}}(t)$ is the linear part and $\delta(t)$ is a non-linear deviation. The linear part is taken to contain the DC and AC parts of the driving force, such that:

$$\zeta \frac{\mathrm{d}x_{\mathrm{lin}}(t)}{\mathrm{d}t} = F_{\mathrm{DC}} + F_{\mathrm{AC}} \cos(\omega t) \quad \text{and} \quad \zeta\, x_{\mathrm{lin}}(t) = F_{\mathrm{DC}} t + \frac{F_{\mathrm{AC}}}{\omega} \sin(\omega t). \tag{5.8}$$

Substituting equations 5.7 and 5.8 into equation 5.6 leads to:

$$\zeta \frac{\mathrm{d}x}{\mathrm{d}t} = F_{\mathrm{DC}} + F_{\mathrm{AC}} \cos(\omega t) + \zeta \frac{\mathrm{d}\delta(t)}{\mathrm{d}t}. \tag{5.9}$$

By neglecting noise and comparing this to equation 5.6, the time derivative of the non-linear deviation may be written using the integrated form of equation 5.8:

$$\zeta \frac{\mathrm{d}\delta(t)}{\mathrm{d}t} = -F_{\mathrm{C}} \sin\left(\frac{2\pi x_{\mathrm{lin}}}{\lambda}\right) = -F_{\mathrm{C}} \sin\left[\frac{2\pi}{\lambda}\left(\frac{F_{\mathrm{DC}}}{\zeta} t + \frac{F_{\mathrm{AC}}}{\zeta\omega} \sin(\omega t) + \delta(t)\right)\right]. \tag{5.10}$$

Using the identity $\sin[A\sin(\omega t) + B] \equiv \sum_{m=-\infty}^{\infty} J_m(A) \sin(B + m\omega t)$, where J_m is the mth order Bessel function of the first kind, equation 5.10 becomes:

$$\zeta \frac{\mathrm{d}\delta(t)}{\mathrm{d}t} = -F_{\mathrm{C}} \sum_{m=-\infty}^{\infty} J_m\left(\frac{2\pi}{\lambda}\frac{F_{\mathrm{AC}}}{\zeta\omega}\right) \sin\left[\left(\frac{2\pi}{\lambda}\frac{F_{\mathrm{DC}}}{\zeta} + m\omega\right) t + \frac{2\pi}{\lambda}\delta(t)\right]. \tag{5.11}$$

Equation 5.11 is difficult to solve, so an approximation is made that only one term of the sum is retained, where $m\omega = -r\omega \approx -2\pi F_{\mathrm{DC}}/\lambda\zeta$, with $r = 0, \pm 1, \pm 2, \ldots$. This approximation is valid while the following condition holds [173–176]:

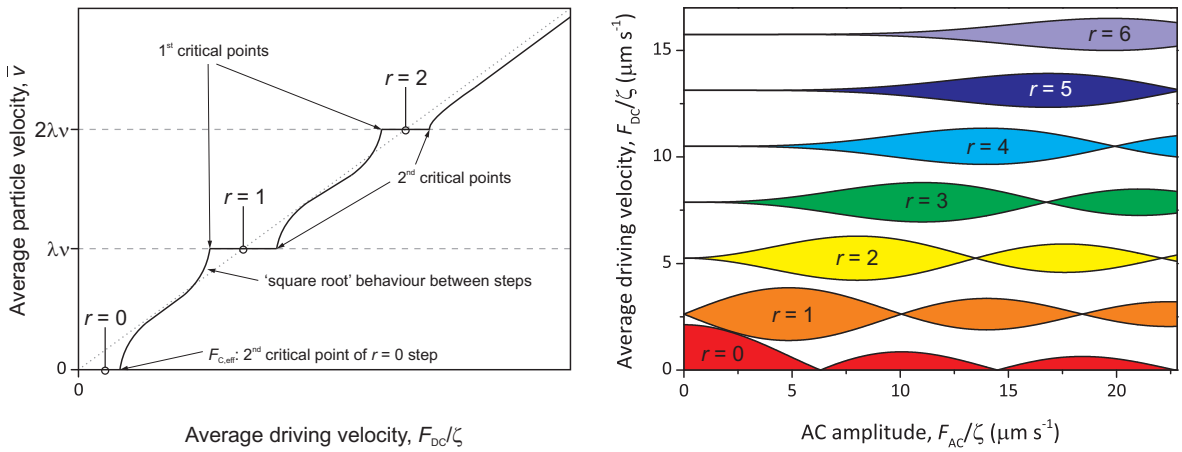
$$\omega \gg \frac{2\pi}{\lambda}\frac{F_{\mathrm{C}}}{\zeta} \quad \text{or} \quad \nu \gg \frac{F_{\mathrm{C}}}{\lambda\zeta}. \tag{5.12}$$

Equation 5.11 therefore becomes:

$$\zeta \frac{\mathrm{d}\delta(t)}{\mathrm{d}t} = -F_{\mathrm{C}} J_{-r}\left(\frac{2\pi}{\lambda}\frac{F_{\mathrm{AC}}}{\zeta\omega}\right) \sin\left[\frac{2\pi}{\lambda}\left(\frac{\Delta F_{\mathrm{DC}}}{\zeta} t + \delta(t)\right)\right], \tag{5.13}$$

where $\Delta F_{\mathrm{DC}} = F_{\mathrm{DC}} - r\lambda\omega\zeta/2\pi$ is a small change in the constant part of the driving force, F_{DC}. Introducing a variable $q(t) = (\Delta F_{\mathrm{DC}}/\zeta)t + \delta(t)$ further reduces equation 5.13 to an equation of the form found for the case of constant drive alone (equation 4.14):

$$\zeta \frac{\mathrm{d}q(t)}{\mathrm{d}t} = \Delta F_{\mathrm{DC}} - F_{\mathrm{C}} J_{-r}\left(\frac{2\pi}{\lambda}\frac{F_{\mathrm{AC}}}{\zeta\omega}\right) \sin\left[\frac{2\pi}{\lambda} q(t)\right]. \tag{5.14}$$



(a) (b)

Figure 5.1: 'High frequency' regime. (a) Illustrative graph of average particle velocity as a function of the average driving velocity (equation 5.15) (not to scale). Mode locked steps lie at $r\lambda\nu$, between pairs of critical points. (b) State diagram calculated from equation 5.16, for a periodic optical potential energy landscape with a trap spacing of $\lambda = 3.5$ μm s^{-1}, for an AC frequency of $\nu = 0.75$ Hz.

The expression for the average velocity may then be written, by noting that $\overline{v} = \left\langle \frac{\mathrm{d}x(t)}{\mathrm{d}t} \right\rangle = F_{\mathrm{DC}}/\zeta + \left\langle \frac{\mathrm{d}q(t)}{\mathrm{d}t} \right\rangle$, as the oscillating force term (the modulated part of the driving velocity) becomes zero after time averaging. Thus an equivalent expression to equation 4.16 is found:

$$\overline{v} = \begin{cases} r\lambda\nu, & \text{if } |\Delta F_{\mathrm{DC}}| < \left| F_{\mathrm{CRIT}} J_{-r}\left(\frac{F_{\mathrm{AC}}}{\lambda\nu\zeta}\right)\right|; \\ r\lambda\nu + \frac{1}{\zeta}\sqrt{\Delta F_{\mathrm{DC}}^2 - F_{\mathrm{CRIT}}^2 J_{-r}^2\left(\frac{F_{\mathrm{AC}}}{\lambda\nu\zeta}\right)}, & \text{if } |\Delta F_{\mathrm{DC}}| > \left| F_{\mathrm{CRIT}} J_{-r}\left(\frac{F_{\mathrm{AC}}}{\lambda\nu\zeta}\right)\right|, \end{cases} \tag{5.15}$$

for $r = 0, \pm 1, \pm 2, \ldots$. Once again this expression describes mean particle velocity 'above' and 'below' critical points, although here there are two critical points found for every absolute value of r. Between each pair of critical points, a 'subcritical' regime exists, where the particle velocity is constant, corresponding to mode locking steps. The two critical points at the ends of resonant step r are found in the deterministic regime as follows [176]:

$$F_{\mathrm{CRIT}} = r\lambda\nu\zeta \pm F_{\mathrm{C}} \left| J_{-r}\left(\frac{F_{\mathrm{AC}}}{\lambda\nu\zeta}\right)\right|. \tag{5.16}$$

The condition for the approximation, $\nu \gg F_{\mathrm{C}}/\lambda\zeta$ (equation 5.12), means that on a landscape with a trap spacing of $\lambda = 3.5$ μm ($F_{\mathrm{C}} \approx 1.8$ μm s^{-1}), the high frequency regime is valid when $\nu \gg 0.5$ Hz. Figure 5.1a shows the dependence of the average particle velocity (equation 5.15) on the driving velocity, F_{DC}/ζ, and indicates critical points, including the effective critical driving velocity, $F_{\mathrm{C,eff}}$. Figure 5.1b shows a state diagram calculated from equation 5.16, for an optical landscape with a trap spacing of $\lambda = 3.5$ μm driven by a modulated drive of frequency $\nu = 0.75$ Hz.

5.3 Experimental methods

5.3.1 Colloidal model system

The colloidal system used is composed of Dynabeads M-270 carboxylic acid (diameter 3 μm), in 20% $EtOH_{aq}$ (see section 2.4.1), held in a Hellma cell (see section 2.4.2). The coefficient of friction, ζ, is found from diffusion to be 9.19×10^{-8} kg s^{-1} (see section 2.1). Particle concentration is low, so that only a single particle is visible in the field of view.

5.3.2 Experimental setup and parameters

The experimental setup consists of an infra-red (1064 nm) laser, controlled using a pair of perpendicular AODs, and focused using a 50×, NA=0.55 microscope objective (see section 2.4.3). The one-dimensional periodic optical landscape, with trap spacing λ = 3.5 μm, is generated in Aresis Tweez software controlled from the LabView interface (see section 2.4.7). A landscape with this trap spacing may be treated as sinusoidal, as shown in Chapter 4. The traps are time-shared at 5 kHz, such that on the time scale of the particles (with a Brownian time of ~ 50 s, and a driven time of at least ~ $\frac{1}{3}$ s per trap spacing), the traps form a constant potential energy landscape.

The laser power and the total number of traps are held constant throughout the experiments, so that the laser power per trap (and hence the trapping parameters k and V_0) are consistent. A laser power of 350 mW is set and 46 traps are used, corresponding to ~ 0.75 mW per trap at the sample position (see section 2.4.3). This gives typical trapping parameters for trap stiffness, $k = 3.8 \times 10^{-7}$ kg s^{-2}, and trap strength, $V_0 = 90\ k_BT$ (see figure 3.5).

The driving force is provided by a PI-542.2CD piezo-stage, controlled using the LabView interface (see section 2.4.5), at 0.05 μm s^{-1} ≤ F_{DC}/ζ ≤ 10 μm s^{-1}. AC driving velocity is added to the DC drive, with an amplitude 0.4 μm s^{-1} ≤ F_{AC}/ζ ≤ 7.9 μm s^{-1}, and a frequency of 0.125 Hz ≤ ν ≤ 1.5 Hz.

Images are focused onto the Ximea CMOS camera using a 40×, NA=0.50 microscope objective. The setting of experimental parameters is automated in the LabView interface. Particle position is recorded live at 40 Hz from the camera image (see section 2.4.7).

5.3.3 Average velocity experiments

To obtain plots of average particle velocity against driving velocity, six repeats are made at each driving velocity for each amplitude and frequency of the AC driving velocity. Average velocity, $\overline{v}$, is found by linearly fitting the particle trajectory, $x(t)$, over an integer number of periods of the oscillation (see figure 5.2a). Data from average velocity experiments is further analysed to find the widths of the steps. The phase, φ, is found from $x(t)$ by subtracting the line of average velocity, dividing by the trap spacing, and multiplying by 2π (see figure 5.2b), such that:

$$\varphi = \frac{2\pi}{\lambda}\left(x(t) - \overline{v}t\right). \tag{5.17}$$

Instantaneous velocity is found by taking the numerical derivative of $x(t)$ (see figure 5.2c), and converted to a phase velocity, or angular frequency, by subtracting the mean velocity, $\overline{v}$, and multiplying by $2\pi/\lambda$ (see figure 5.2d), such that:

$$\frac{\mathrm{d}\varphi}{\mathrm{d}t} = \frac{2\pi}{\lambda}\left(\frac{\mathrm{d}x}{\mathrm{d}t} - \overline{v}\right) = \frac{2\pi}{\lambda}(v - \overline{v}), \tag{5.18}$$

which is plotted against phase to form phase portraits (see figure 5.2e).

5.3.4 Critical velocity experiments

The critical DC driving velocity is defined as the DC driving velocity at which the particle starts to slide irreversibly across the optical potential energy landscape. It is found by iterating the DC driving velocity, with a maximum resolution of 0.05 μm s^{-1}. A particle is said to be pinned if it still returns to its starting lattice position after the stage has moved 100 μm, or three minutes has elapsed, whichever happens first. The region in which the particle does not irreversibly slide is essentially the zeroth mode locked step, and the effective critical driving velocity is therefore the second critical point of this step (see section 5.2.1).

The critical driving velocity found here is *not* the critical driving velocity found in Chapter 4, F_{C}/ζ, because the total driving force in equation 5.6 is a sum of the DC and time dependent AC contributions. Therefore the critical driving velocity measured here is an *effective* critical driving velocity, $F_{\mathrm{C,eff}}/\zeta$, as it is not purely a property of the landscape.

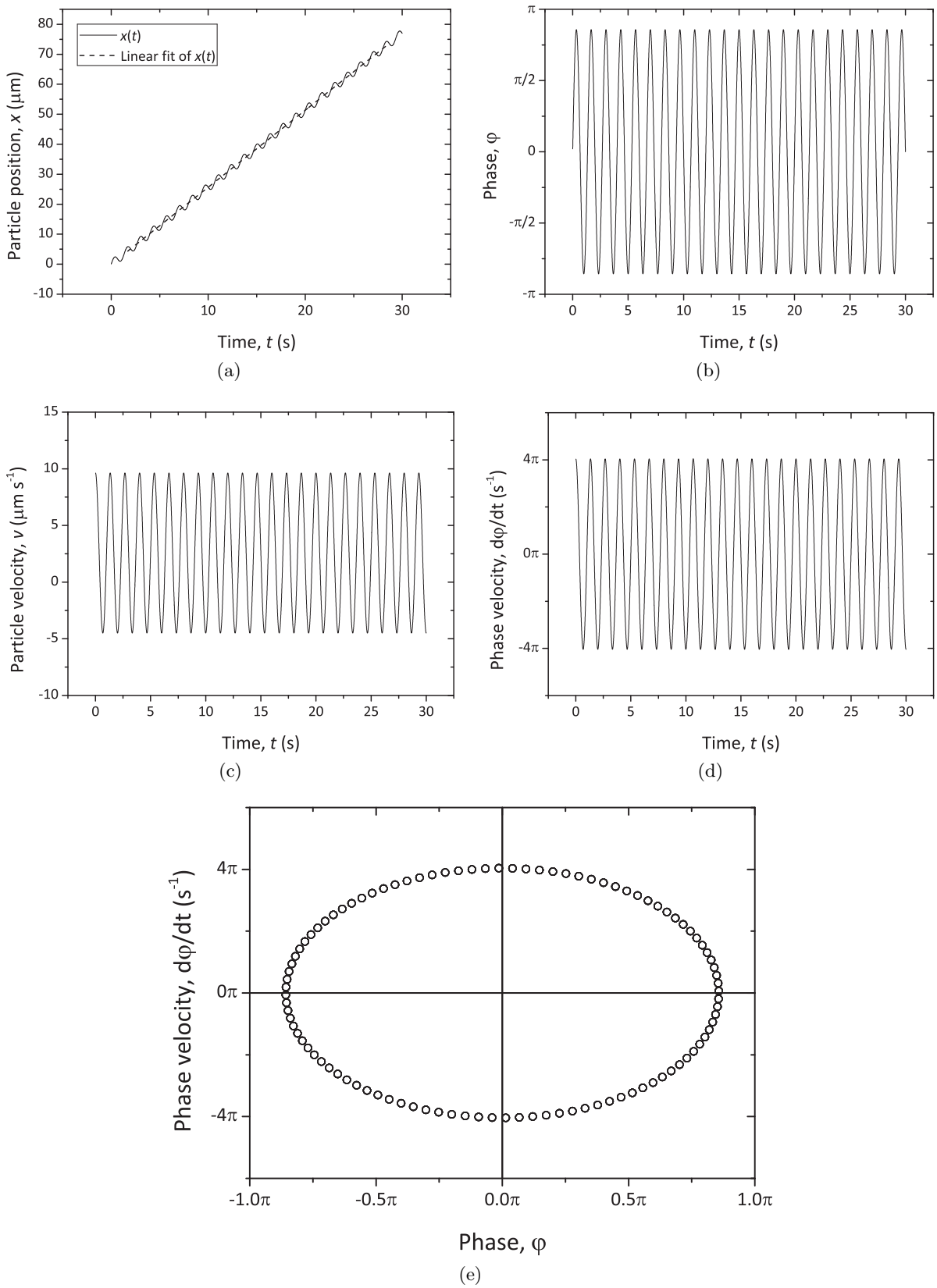


Figure 5.2: From particle trajectory to phase portrait (idealised data). (a) Particle trajectory, $x(t)$, with linear fit to find average velocity, $\overline{v}$. (b) Phase, $\varphi(t) = (2\pi/\lambda)(x(t) - \overline{v}t)$. (c) Particle velocity, $v(t) = \mathrm{d}x(t)/\mathrm{d}t$. (d) Phase velocity, $\mathrm{d}\phi(t)/\mathrm{d}t = (2\pi/\lambda)(v - \overline{v})$. (e) Phase portrait: phase velocity, $\mathrm{d}\phi(t)/\mathrm{d}t$, against phase, $\phi(t)$.

5.4 Results and discussion

5.4.1 The 'Devil's staircase'

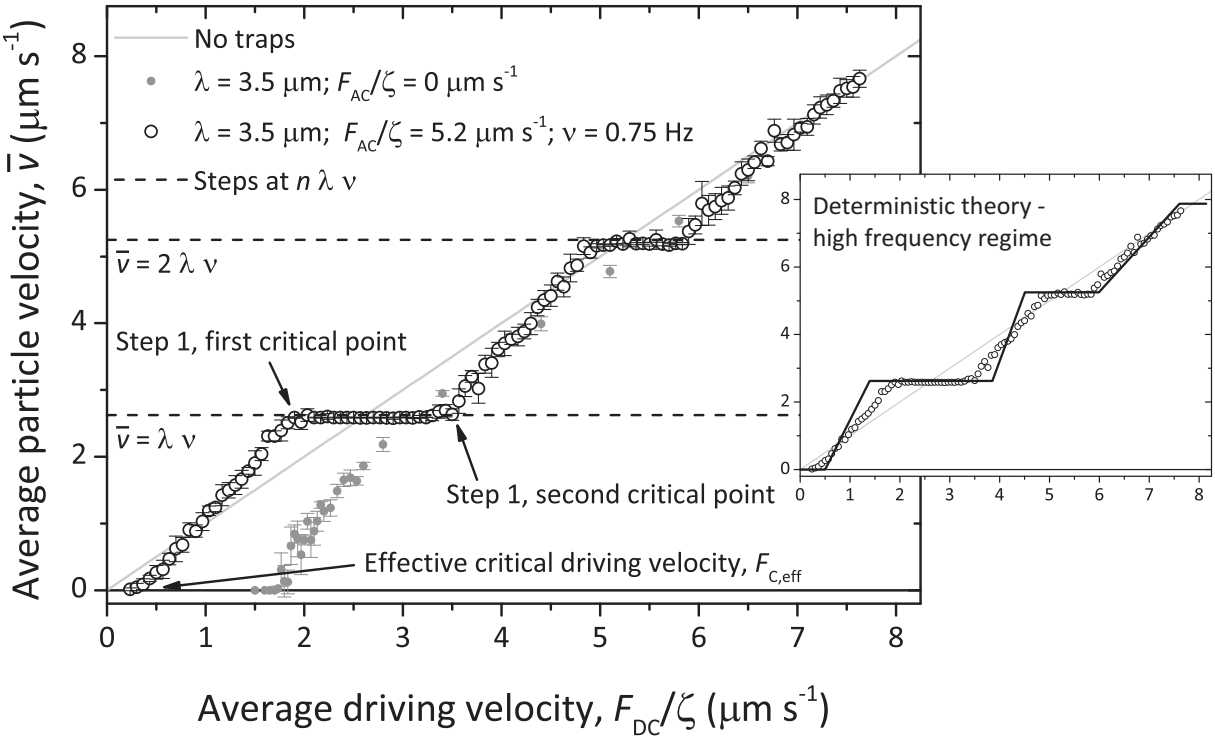


Figure 5.3: The average particle velocity, $\overline{v}$, against average driving velocity, F_{DC}, for non-zero amplitude of oscillation F_{AC}. ○ F_{AC}/ζ = 5.2 μm s^{-1}, ν = 0.75 Hz (error bars represent the standard deviation of the repeats); • F_{AC} = 0 (from figure 4.4); - - - resonance step velocity, $\overline{v} = n\lambda\nu$; — no traps line from figure 2.10a.

Results are presented which show the non-linear dynamic effects seen when colloidal particles are driven by a modulated force over a periodic optical potential energy landscape. Figure 5.3 shows the effect on the average velocity, $\overline{v}$, of introducing the oscillating force term to the equation of motion (equation 5.6). One set of data with a modulated force of amplitude F_{AC}/ζ = 5.2 μm s^{-1} and frequency ν = 0.75 Hz is presented, and compared to the F_{AC} = 0 (i.e. DC drive only) data for a landscape of trap spacing λ = 3.5μm (see Chapter 4). The case of $F_{\mathrm{AC}} \neq 0$ clearly deviates from the DC only case. The effective critical driving velocity is almost zero. After that $\overline{v}$ increases roughly linearly until it is significantly larger than the no trap line, implying that the particle is moving on average more quickly than the piezo stage which drives the particle.

The average velocity then plateaus at $\overline{v} \approx 2.6$ μm s^{-1}, which is the first resonant step

at $\overline{v} = 1\lambda\nu$. The step extends over a range of driving velocities, from the first critical point at $F_{\mathrm{DC}}/\zeta \approx 2.0$ μm s^{-1} to the second critical point at $F_{\mathrm{DC}}/\zeta \approx 3.3$ μm s^{-1}, where $\overline{v}$ increases again. Average velocity then plateaus a second time, at $\overline{v} = 2\lambda\nu \approx 5.2$ μm s^{-1}. This second resonance step extends over a smaller range of driving velocities, from the first critical point at $F_{\mathrm{DC}}/\zeta \approx 4.9$ μm s^{-1} to the second critical point at $F_{\mathrm{DC}}/\zeta \approx 5.8$ μm s^{-1}. Finally, $\overline{v}$ increases again. The dashed lines on figure 5.3 show that the two plateaus lie at the first two integer multiples of $\lambda\nu$. This means that on the steps, the particle moves through an integer number of wavelengths of the landscape in one period of the oscillating drive. These steps represent the range of driving forces over which the particle motion is locked into each of the first two dynamic modes of the system. The resonance condition for this locking is that the 'internal frequency' of the particle moving over the periodic optical potential energy landscape ($\sim \overline{v}/\lambda$) matches an integer times the imposed frequency, ν, of the modulated driving force. The graph composed of these mode locked steps in the average velocity is know as a 'Devil's Staircase', and is analogous to the Shapiro Steps seen in Josephson junctions [155], and also in charge density wave systems [114] and vortex lattices [6, 150, 151, 175].

The inset in figure 5.3 compares the experimental data to the theoretical predictions for the high frequency regime (equation 5.16). The theoretical line is constructed by connecting the critical points found for steps $n = 0$ to $n = 3$, with step velocity given by $n\lambda\nu$. Although qualitatively correct, the first critical points for each step are underestimated, and the second critical points overestimated, as the theory is deterministic and does not take into account the Brownian noise which will smooth the ends of each step.

5.4.2 Trajectories and phase portraits

Next, the microscopic dynamics underlying the macroscopic staircase behaviour depicted in figure 5.3 are elucidated by analysing particle trajectories individually. Figure 5.4a indicates five points in figure 5.3, both on and in between the mode locked steps. Typical particle trajectories (particle position, x, against time, t) are shown in figure 5.4b. The locked trajectories, when the system is on a step, show very regular oscillation as the particle moves forward, with small irregularities introduced by Brownian motion. The insets show single periods of the oscillation for the locked trajectories (B and D), demonstrating that the particle moves forward by an integer number of trap spacings in a single period of the oscillation. Between the steps, unlocked

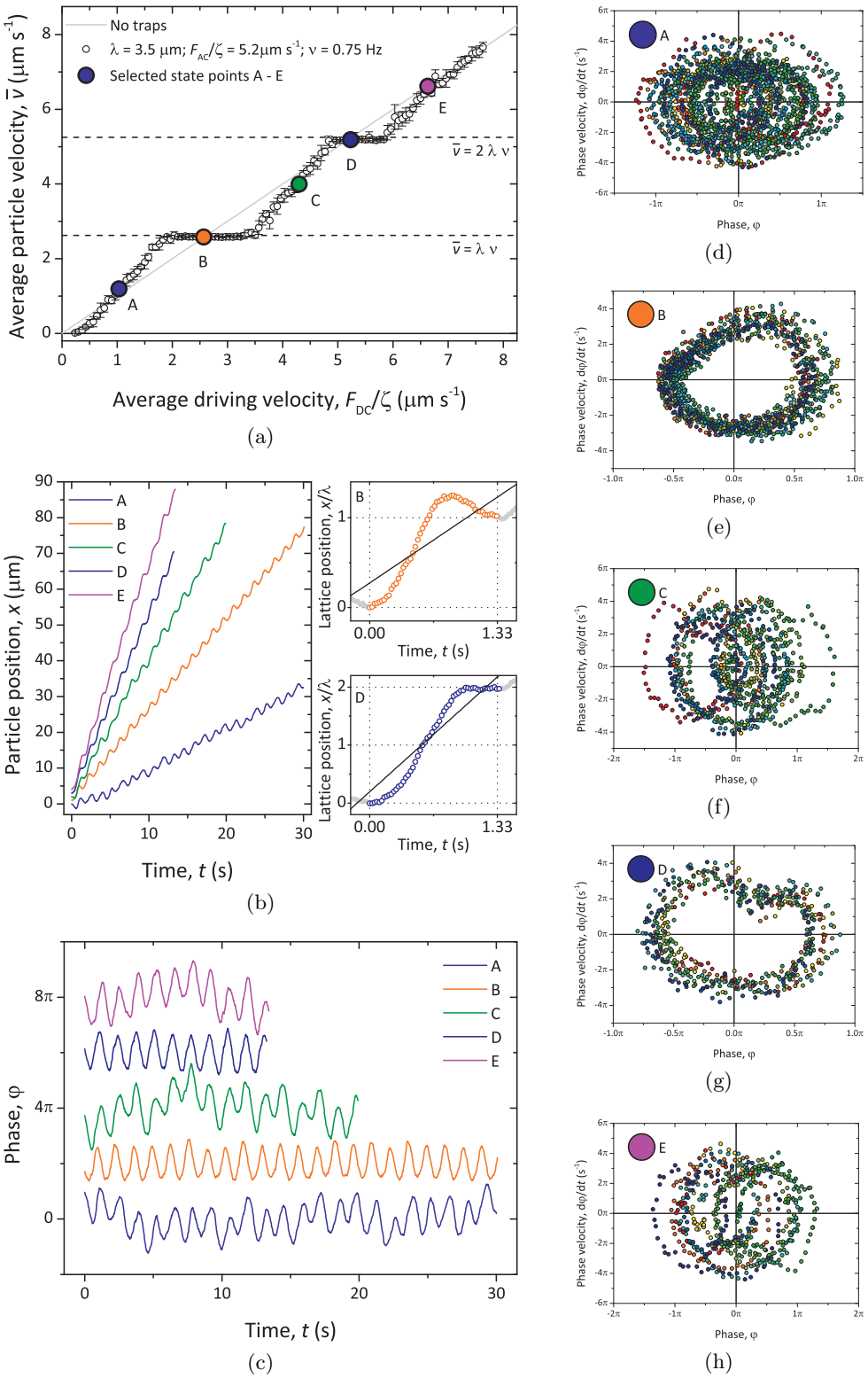


Figure 5.4: Trajectories and phase portraits. (a) Five points on the staircase: F_{DC}/ζ = 1.033 μm s^{-1}, 2.567 μm s^{-1}, 4.300 μm s^{-1}, 5.233 μm s^{-1}, and 6.633 μm s^{-1}. (b) Main panel: particle trajectories, $x(t)$; small panels: single oscillation trajectories for points B (on step 1) and D (on step 2). Solid lines show average particle velocity. (c) Trajectories presented as $\varphi(t)$, vertically shifted for clarity. (d)-(h) Phase portraits, with F_{DC}/ζ increasing down the page. Each cycle is represented by a colour, from red for cycle 0 to blue for the final cycle.

trajectories show irregular oscillations. This is made clearer by figure 5.4c, where the phase, φ, is plotted against time.

The phase describes where the particle is on an oscillation cycle. It is therefore well defined for locked states, and ill-defined for unlocked states. Figure 5.4c shows that when the system is in a locked state, the phase oscillates regularly as a function of time, as the particle undergoes a regular, predictable, cycle of motion. The unlocked states, however, show irregular oscillation, with no fixed amplitude to each cycle. This is because when the particle is in an unlocked state, it does not move a regular distance in each 'cycle' of its oscillation.

Another direct way to represent the periodic, locked nature of the dynamics is shown in figures 5.4d to 5.4h, where phase velocity, $\mathrm{d}\varphi/\mathrm{d}t$ is plotted against the phase, φ. These 'phase portraits' capture the particle's whole microscopic motion. Figures 5.4e and 5.4g show locked states, where the phase velocity oscillations form 'closed loops' as a function of the phase. The shape of the two loops is different, as in figure 5.4e the particle moves forward by a total of one lattice spacing, whereas in figure 5.4g, the particle moves forward by two lattice spacings (see also figure 5.4b, insets). The dip in velocity seen on the top of the phase portrait in figure 5.4g may be attributed to the effect of the trap through which the particle completely passes on each cycle.

The phase portraits in figures 5.4d, 5.4f, and 5.4h correspond to unlocked states, and show 'open loops'. This occurs because the particle does not follow a regular velocity cycle. As each cycle is given a different colour in the phase portraits, it is possible to see that all cycles lie on top of each other when the system is locked, whereas the cycles are all centred around different points (which are randomly distributed in φ) when the system is unlocked.

5.4.3 Frequency dependence

The mean velocities of the steps depend on the frequency of the oscillating part of the driving force, as the resonant condition is $\overline{v} = n\lambda\nu$. Now the effect of the frequency is studied in more detail. Figure 5.5 shows experimental data at three different frequencies, for an amplitude of $F_{\mathrm{AC}}/\zeta = 2.0\ \mu\mathrm{m\ s}^{-1}$. At a lower frequency more steps are seen over the same range of particle velocities as more harmonics are attainable. Indeed at the lowest frequency, $\nu = \frac{1}{4}$ Hz, the mean particle velocity shows three steps corresponding to the first three integer multiples of $\nu\lambda$, at

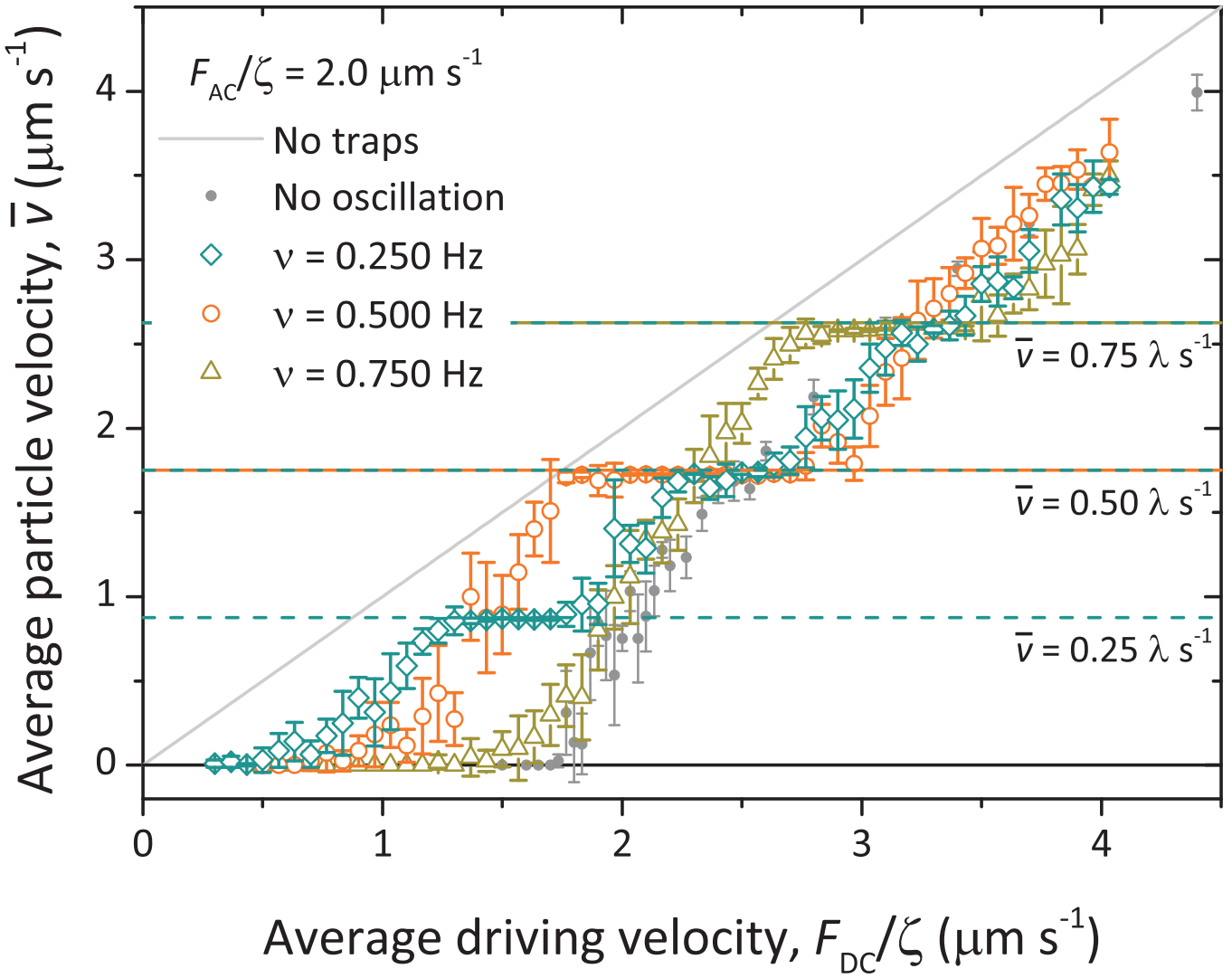


Figure 5.5: Average particle velocity as a function of average driving velocity, at constant AC amplitude of F_{AC}/ζ = 2.0 μm s^{-1}, for three different frequencies; ◇ $\nu = \frac{1}{4}$ Hz, ○ $\nu = \frac{1}{2}$ Hz, △ $\nu = \frac{3}{4}$ Hz. Dashed lines indicate step positions for $\nu = \frac{1}{4}$ Hz (- - -), $\nu = \frac{1}{2}$ Hz (- - -), and $\nu = \frac{3}{4}$ Hz (- - -). • $F_{AC} = 0$ (from figure 4.4), — calibration line from figure 2.10a

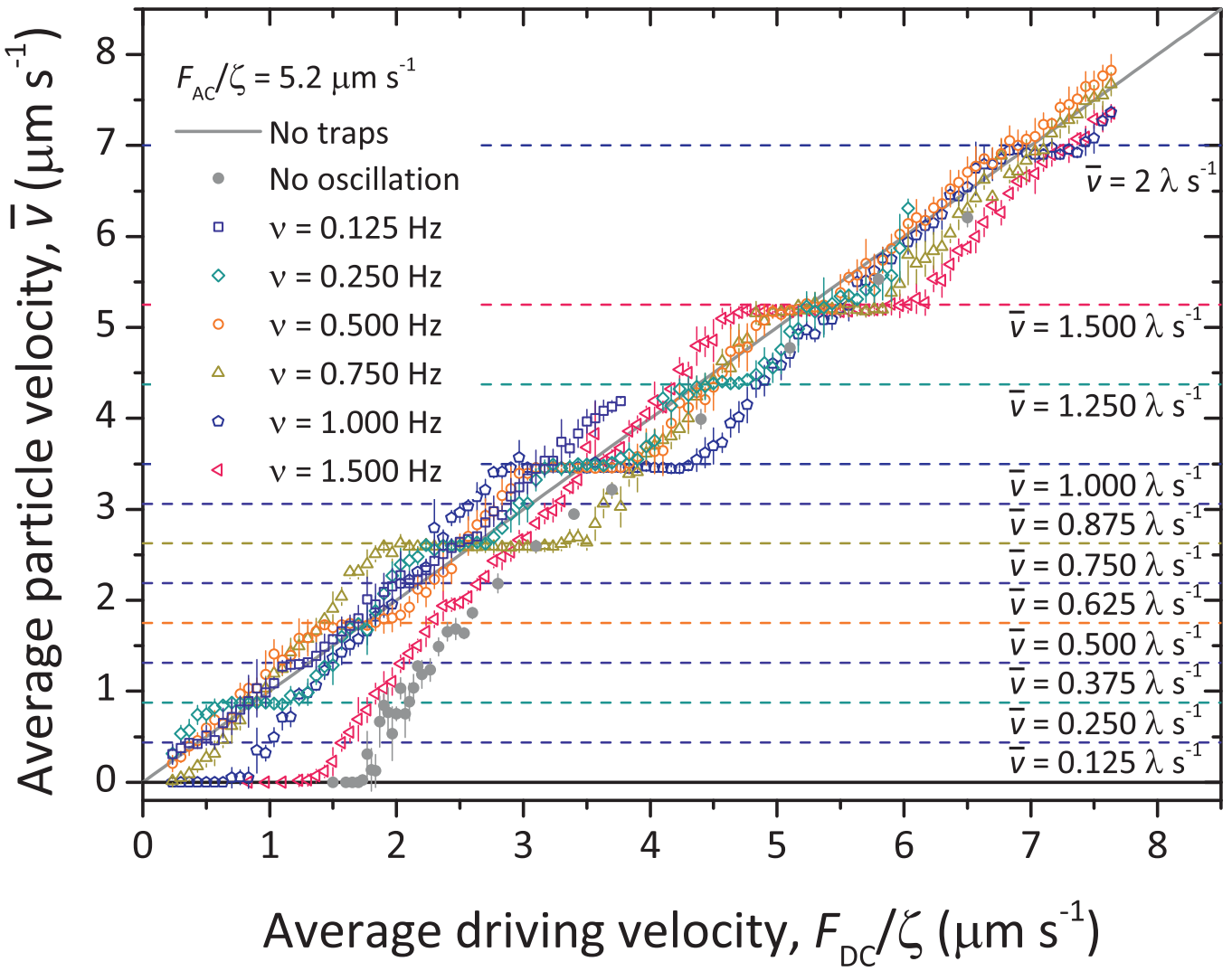


Figure 5.6: Average particle velocity as a function of average driving velocity, at constant AC amplitude of $F_{AC}/\zeta = 5.2$ μm s^{-1}, for six different frequencies; □ $\nu = \frac{1}{8}$ Hz, ◇ $\nu = \frac{1}{4}$ Hz, ○ $\nu = \frac{1}{2}$ Hz, △ $\nu = \frac{3}{4}$ Hz, ⬠ $\nu = 1$ Hz, ◁ $\nu = \frac{3}{2}$ Hz. • $F_{AC} = 0$ (from figure 4.4), — calibration line from figure 2.10a

$\nu\lambda = \frac{1}{4}\lambda$ s^{-1}, $2\nu\lambda = \frac{2}{4}\lambda$ s^{-1}, and $3\nu\lambda = \frac{3}{4}\lambda$ s^{-1}. The second and third steps at this frequency therefore coincide with the first steps for the other two frequencies, of $\nu = \frac{1}{2}$ Hz and $\nu = \frac{3}{4}$ Hz.

Figure 5.6 shows the frequency dependence of the average particle velocity for an AC amplitude of $F_{AC}/\zeta = 5.2$ μm s^{-1}, for frequencies ranging from $\nu = \frac{1}{8}$ Hz to $\nu = \frac{3}{2}$ Hz. Even at the very bottom of this range ($\nu = \frac{1}{8}$ Hz), small steps are visible, particularly at $\overline{v} = \frac{1}{8}\lambda$ s^{-1}, $\frac{3}{8}\lambda$ s^{-1}, $\frac{5}{8}\lambda$ s^{-1}, and λ s^{-1}. The trend continues as outlined above, with steps only at integer multiples of $\nu\lambda$. Steps appear on all other lines, from $\nu = \frac{1}{4}$ Hz (5 visible steps, from 6 possible), through $\nu = \frac{1}{2}$ Hz (3 from 4), $\nu = \frac{3}{4}$ Hz (2 from 2), $\nu = 1$ Hz (2 from 2), to $\nu = \frac{3}{2}$ Hz (1 from 1). It is worth noting that not all possible steps appear; for example there is no visible step at $\overline{v} = \frac{1}{2}\lambda$ s^{-1} for $\nu = \frac{1}{4}$ Hz. This occurs because step width is oscillatory with F_{AC} and ν (see below) and is therefore sometimes zero, or within the noise or the experimental error of the data.

Critical driving velocity

It is also clear from figures 5.5 and 5.6 that the critical driving velocity is dependent on the frequency of the oscillating driving velocity [167,177]. This is shown more clearly in figure 5.7a, where the effective critical driving velocity is plotted as a function of frequency, for data at an AC amplitude of $F_{AC}/\zeta = 5.2$ μm s^{-1}. Note that this is an *effective* critical driving velocity as the driving force is a combination of AC and DC driving forces (see section 5.3.4). The behaviour is in fact rather complex: the experimental data first show a small bump, with critical driving velocity then decreasing back to zero, before increasing again, and then reaching a plateau at $F_C/\zeta = 1.25$ μm s^{-1} when $\nu = 1.5$ Hz. Also presented on figure 5.7a is the theoretical prediction from equation 5.16, which is only plotted from $\nu = 0.6$ Hz, as this equation corresponds to the high frequency regime. The trend seen in the experimental data is well captured, but the magnitude is significantly lower than predicted. This is expected, as the prediction is deterministic and does not account for Brownian noise, which is inevitably present in the experimental data.

Step width

The width of the mode locked steps, $\Delta F/\zeta$, also depends on the driving parameters [177]. Figure 5.7b shows the frequency dependence of the width of the first two steps for $F_{AC}/\zeta = 5.2$ μm s^{-1}, from the data in figure 5.6. Only a limited range of frequencies have been studied here as high

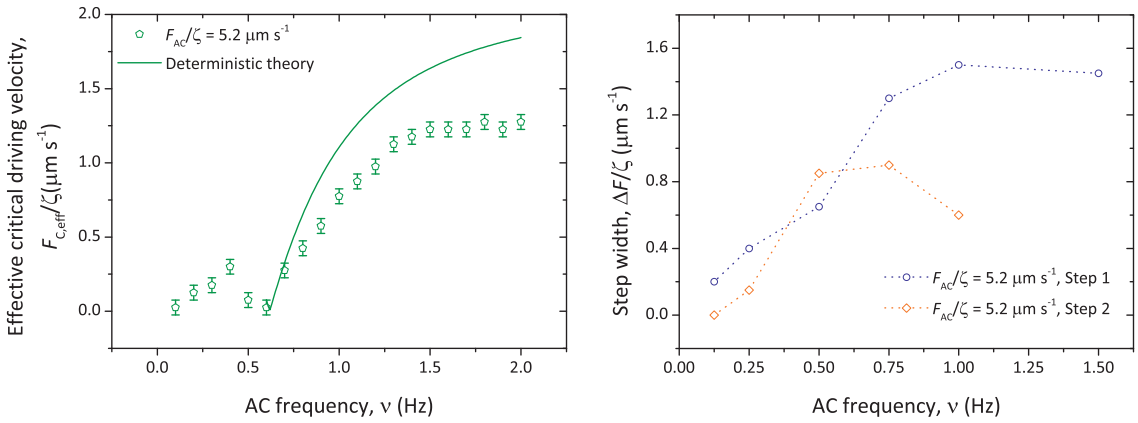


Figure 5.7: (a) Critical driving velocity, F_C/ζ, as a function of frequency of oscillation, ν, for F_{AC}/ζ = 5.2 μm s^{-1} (see figure 5.6). (b) Step width, $\Delta F/\zeta$, as a function of frequency of oscillation, for the first two steps for amplitude F_{AC}/ζ = 5.2 μm s^{-1}; ○ step 1, ◇ step 2 (see figure 5.6).

driving velocities are required to reach the first step at high frequency, leading to poor statistics. Nevertheless, some trends may be observed. The first step starts with a finite width, which then increases with ν, and appears to peak at a value of $\Delta F/\zeta$ = 1.5 μm s^{-1} at ν = 1 Hz. The second step starts from zero width, and then peaks much lower, at $\Delta F/\zeta$ = 0.9 μm s^{-1}, when $\nu = \frac{3}{4}$ Hz, before decreasing. The predictions of the high frequency regime (equation 5.16) are not attempted here, as they cover too small a region of the data to make a comparison meaningful.

5.4.4 Amplitude dependence

Next, the dependence of dynamic mode locking on the AC amplitude is examined. Because the step velocity depends only on the trap spacing and the frequency, steps for different amplitude lie at the same set of velocities. Figure 5.8 shows mode locking steps for seven different amplitudes, at the same frequency, $\nu = \frac{3}{4}$ Hz. There is a strong dependence of the width of the locked step on the amplitude of the oscillation. For very low amplitudes there is a small visible first step, giving a deviation from the zero oscillation data, but no second step is observed; the points lie on top of the DC-only line. As amplitude increases, the first step increases in width, and a small second step appears. As the amplitude increases further, a clear and growing second step appears, but the first step appears to be decreasing in size.

Figure 5.9 shows similar behaviour at a lower frequency of $\nu = \frac{1}{4}$ Hz, i.e. a much larger number of steps, at eight different amplitudes. Up to eight steps are visible, although not all

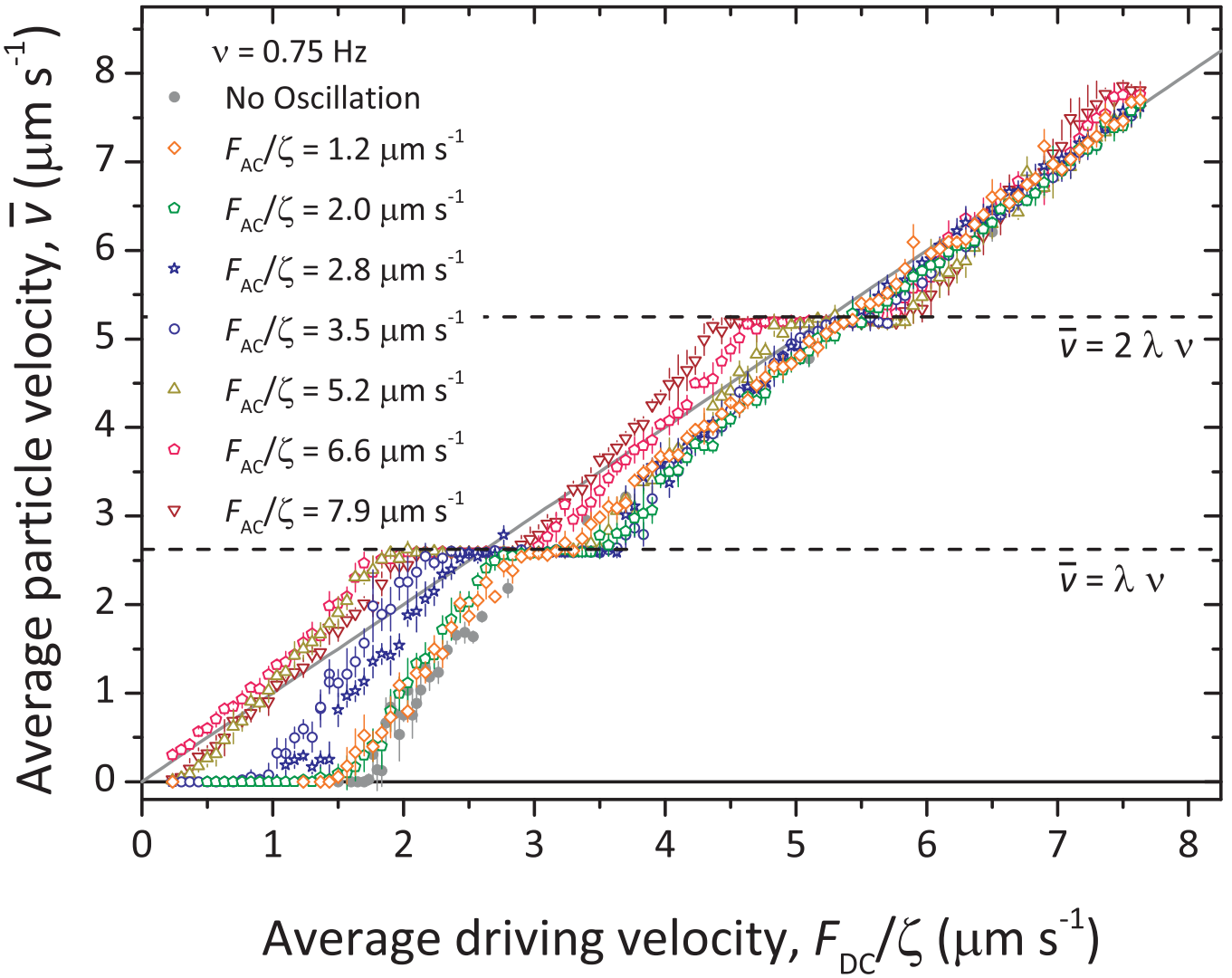


Figure 5.8: Average particle velocity as a function of average driving velocity, at a constant AC frequency of $\frac{3}{4}$ Hz, for seven different amplitudes; ◇ F_{AC}/ζ = 1.2 μm s^{-1}, ⬠ F_{AC}/ζ = 2.0 μm s^{-1}, ☆ F_{AC}/ζ = 2.8 μm s^{-1}, ○ F_{AC}/ζ = 3.5 μm s^{-1}, △ F_{AC}/ζ = 5.2 μm s^{-1}, ⬠ F_{AC}/ζ = 6.6 μm s^{-1}, ▽ F_{AC}/ζ = 7.9 μm s^{-1}.

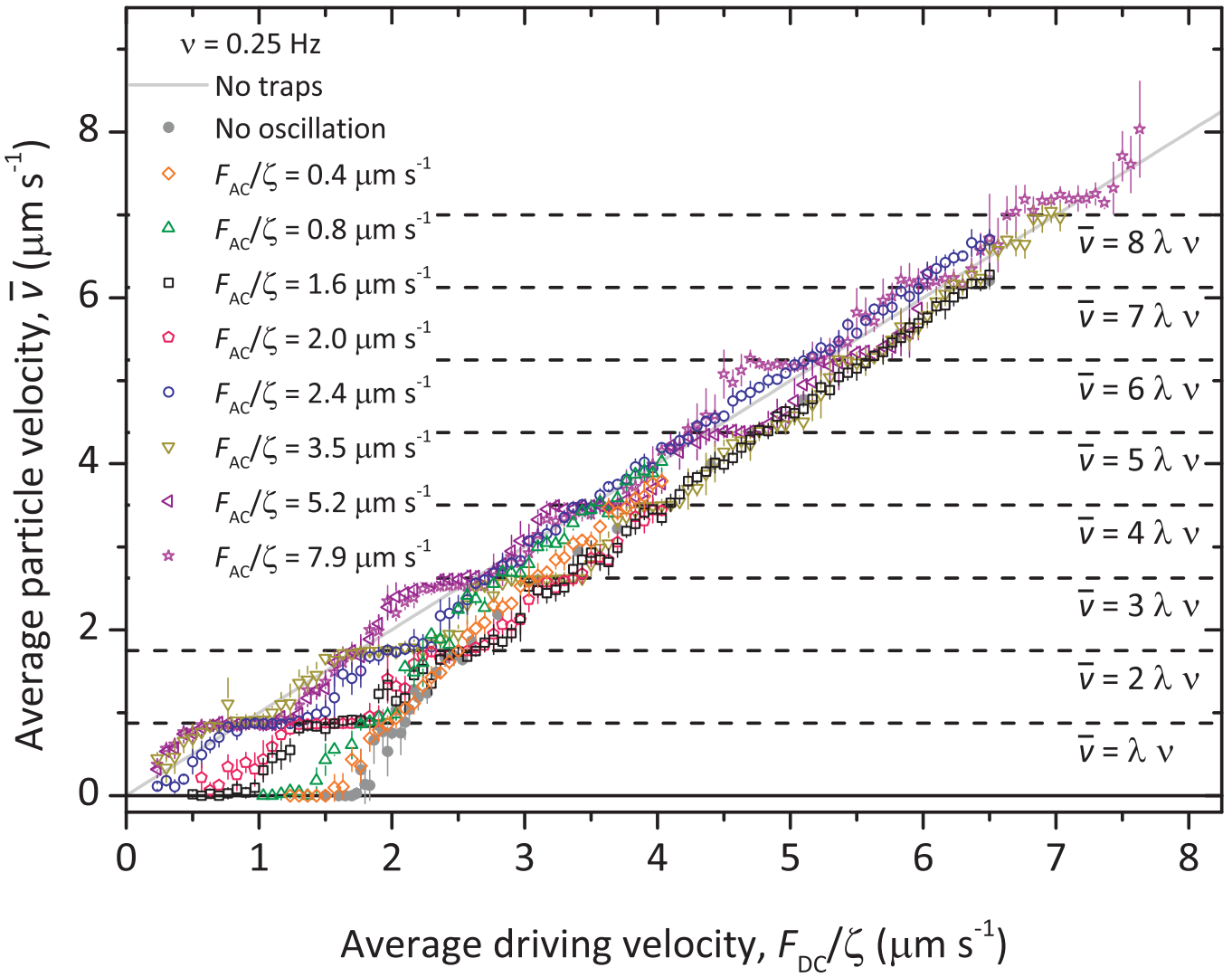


Figure 5.9: Average particle velocity as a function of average driving velocity, at a constant AC frequency of $\frac{1}{4}$ Hz, for eight different amplitudes; ◇ F_{AC}/ζ = 0.4 μm s^{-1}, △ F_{AC}/ζ = 0.8 μm s^{-1}, □ F_{AC}/ζ = 1.6 μm s^{-1}, ⬠ F_{AC}/ζ = 2.0 μm s^{-1}, ○ F_{AC}/ζ = 2.4 μm s^{-1}, ▽ F_{AC}/ζ = 3.5 μm s^{-1}, ◁ F_{AC}/ζ = 5.2 μm s^{-1}, ☆ F_{AC}/ζ = 7.9 μm s^{-1}.

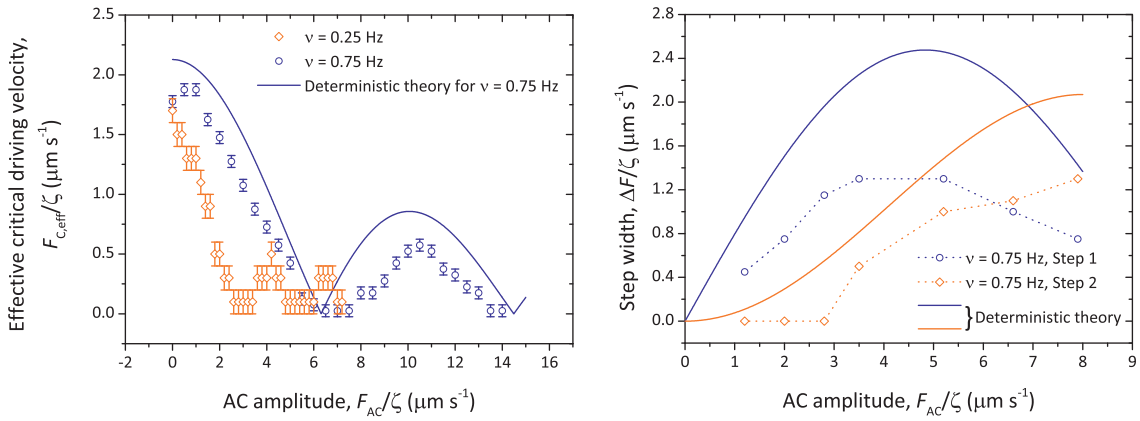


Figure 5.10: (a) Critical driving velocity, F_C/ζ, as a function of amplitude of oscillation, F_{AC}/ζ, for $\nu = \frac{1}{4}$ Hz and $\nu = \frac{3}{4}$ Hz (see figures 5.8 and 5.9). (b) Step width, $\Delta F/\zeta$, as a function of amplitude of oscillation, for the first two steps for frequency $\nu = \frac{3}{4}$ Hz; ○ step 1, ◇ step 2 (see figure 5.8).

steps appear for all lines, as sometimes the step width is zero (see below). Again, the widths of these steps are clearly dependent on amplitude.

Critical driving velocity

Figure 5.10a shows the critical driving velocity as a function of amplitude, for data at frequencies of $\nu = \frac{1}{4}$ Hz and $\nu = \frac{3}{4}$ Hz. Once again the behaviour is non-monotonic: at small amplitudes, an increase in F_{AC} causes a sharp decrease in F_C, but this then periodically increases and decreases again, with a Bessel-function-like form. For the higher frequency measurements the same behaviour appears, stretched out over a larger range of F_{AC}. Each peak represents a different mode of the pinned state. Regions where the critical force is zero occur because thermal motion is sufficient overcome the barriers. The theoretical prediction for the high frequency regime (equation 5.16) predicts the shape of the experimental data reasonably well.

Step width

The width of both of the steps in figure 5.8 is shown for all of the amplitudes in figure 5.10b. The first step increases to a maximum width of $\Delta F/\zeta = 1.3$ μm s^{-1} and then decreases again. The second step is initially of zero width and then increases until it is larger than the first step. Theoretical predictions from equation 5.16 are shown, and clearly overestimate the experimental data, due to thermal noise being neglected.

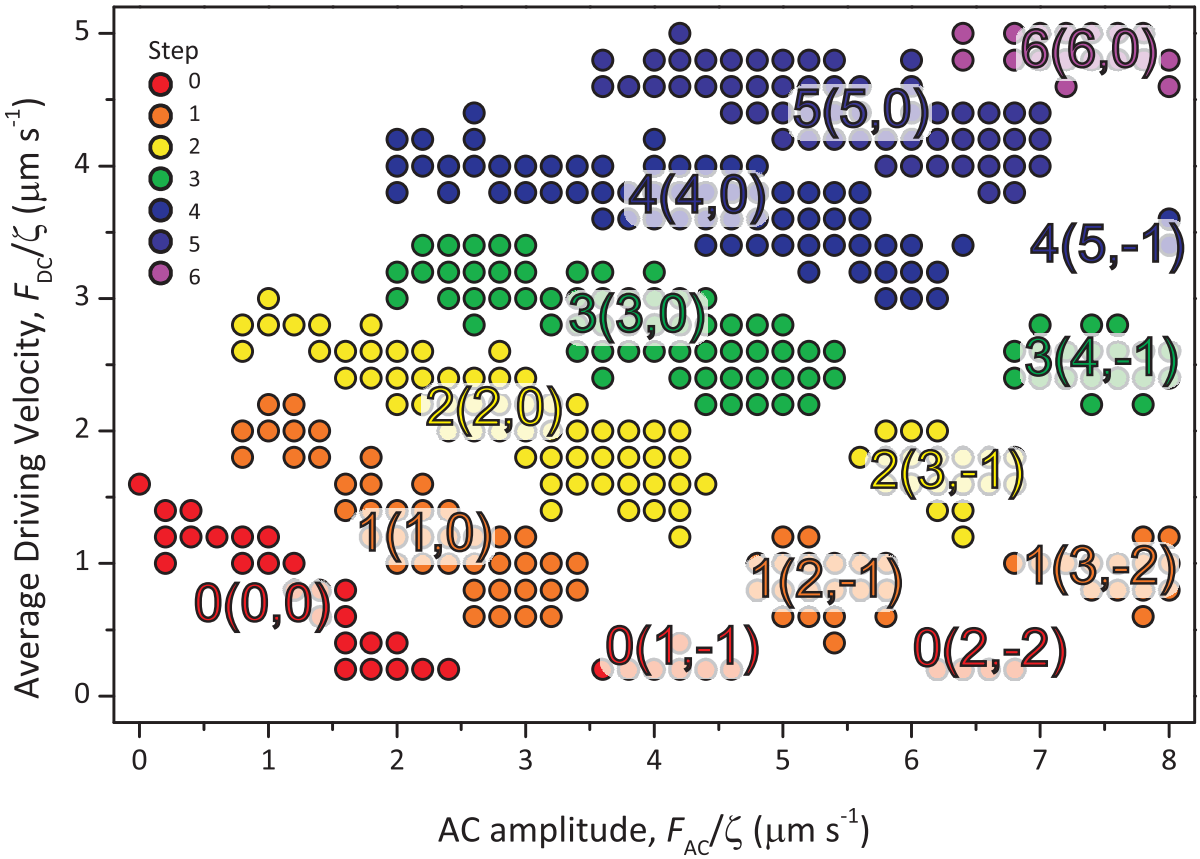


Figure 5.11: State diagram showing all dynamic modes over a range of AC amplitudes and average driving velocities. Regions of the same colour represent the same net forward motion, white regions represent unlocked states. Regions are labelled with their modes in the form $n(i, j)$, where n is the total forward motion, i is the maximum forward motion and $-j$ is the number of reverse steps, such that $i + j = n$.

State diagram

In order to draw together the amplitude dependent behaviour of the system, a state diagram is constructed. Figure 5.11 shows the extent of each dynamic mode in $F_{\mathrm{AC}}/\zeta, F_{\mathrm{DC}}/\zeta$ space. Each point on the diagram is coloured according to the nature of the mode the system is in at that point. Note that points corresponding to unlocked states are not shown for ease of interpretation.

Each colour on the state diagram represents a net forward motion of an integer number of wavelengths of the landscape. For example, the orange regions correspond to a net forward motion of one lattice spacing, the yellow regions correspond to a net forward motion of two lattice spacings, and so on. Separated regions of the same colour represent different modes with the same net result: the three orange regions represent net forward motion of one wavelength

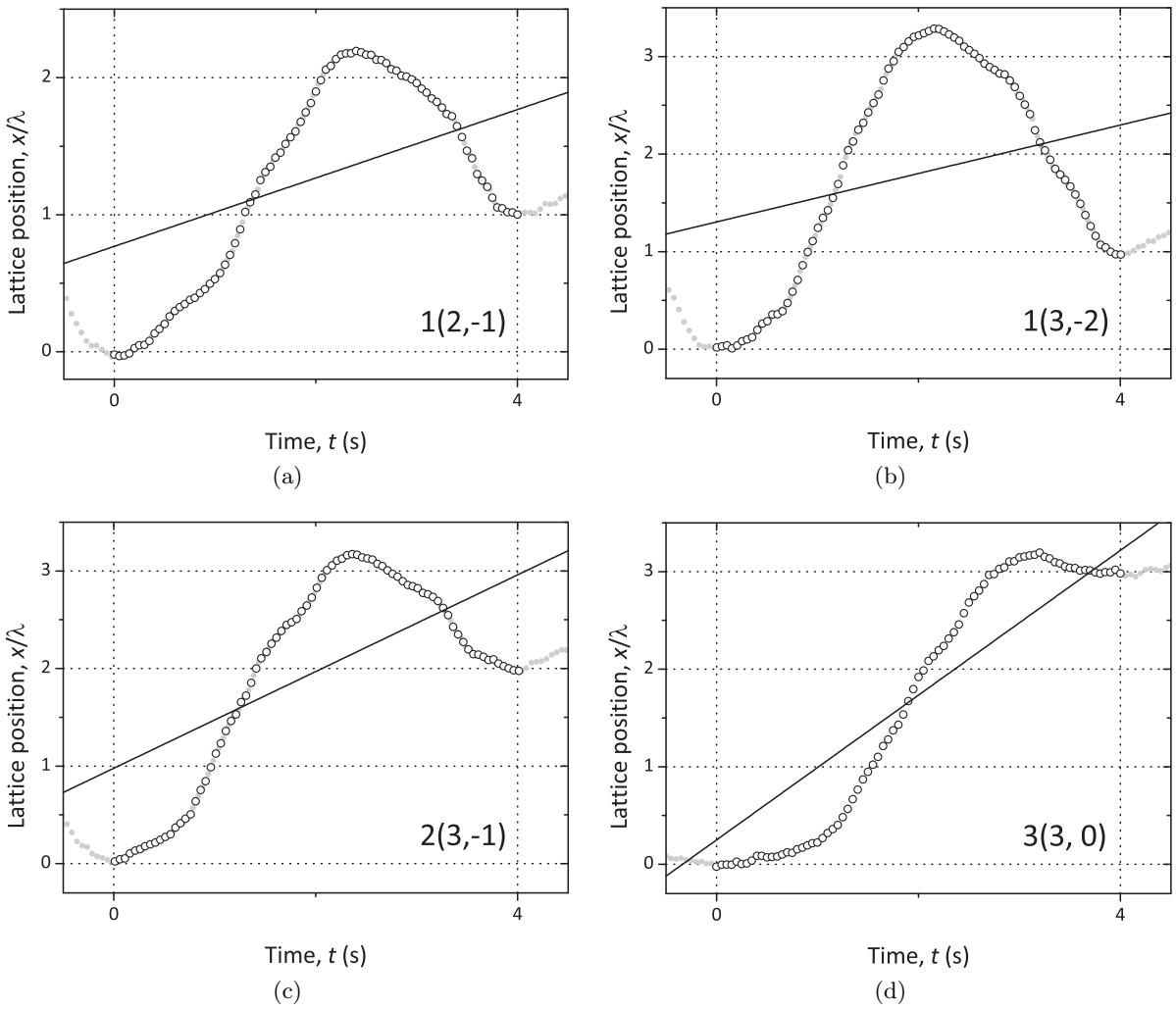


Figure 5.12: Single oscillation trajectories corresponding to selected modes from the state diagram (figure 5.11). ○ Experimental data. — average particle velocity (linear fit to whole trajectory). Modes are labelled as $n(i,j)$, where n is the total forward motion, i is the maximum forward motion and $-j$ is the number of reverse steps, such that $i+j=n$. (a) and (b) both show net forward motion of 1λ, through different pathways. (b), (c), and (d) all show maximum forward displacement of 3λ, but have net forward motion of 1λ, 2λ, and 3λ respectively.

via three different routes. The microscopic nature of the modes is represented as $n(i,j)$, where n is the net forward motion, i is the maximum forward displacement in wavelengths, and $-j$ is the number of wavelengths moved in reverse, such that $i+j=n$. The critical driving velocity and step widths are also visible in the state diagram. It is clear from the edge of the $0(i,j)$ modes that the critical driving velocity oscillates with a Bessel function-like form, consistent with the critical driving velocities for $\nu = 0.25$ Hz shown in figure 5.10a. The shape of the regions shows that for each mode, the step width has an oscillatory behaviour, with gaps present between the locked modes, where the system exists in unlocked states. This state diagram is qualitatively similar to that calculated for the high frequency regime, in figure 5.1b.

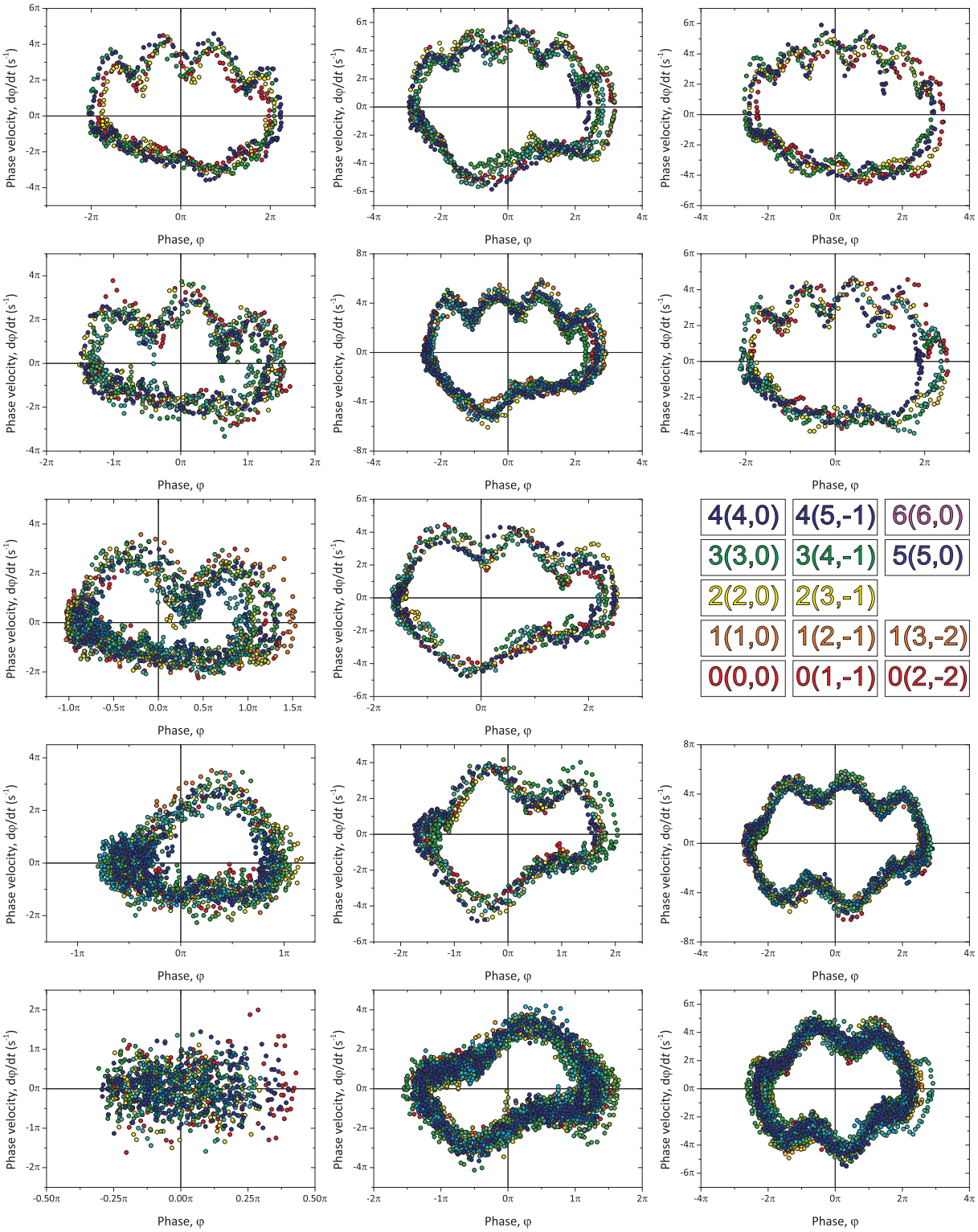


Figure 5.13: Phase portraits for all of the modes found in the state diagram (figure 5.11). Modes are labelled as $n(i, j)$, where n is the total forward motion, i is the maximum forward motion and $-j$ is the number of reverse steps, such that $i + j = n$.

The microscopic motion underlying these different modes may be discerned from the particle trajectories as introduced in figure 5.4b (insets). Figure 5.12 shows single periods of the oscillation (all equal to 4 s because $\nu = \frac{1}{4}$ Hz) for four different modes from the state diagram. Because each trajectory displays a locked state, the *net* forward motion is always an integer number of lattice spacings; 1 in (a) and (b), 2 in (c), and 3 in (d). Panels (a-c) show that the particle may experience a maximum displacement of far more than its net motion. These trajectories are very illuminating, as they allow for determination of the nature of the modes. Panel (a) for example clearly shows that during one period of the oscillation, the particle moves forward a single wavelength, via a maximum displacement of two wavelengths. This should be compared to panels (b) (net displacement one, maximum displacement three) and (c) (net displacement two, maximum displacement three). Panel (d) shows a mode for which the net and maximum displacements are both the same, at three wavelengths.

The microscopic motion may be shown even more compellingly by plotting phase portraits. Figure 5.13 illustrates each of the fourteen states displayed on the state diagram. The top half of each phase portrait represents forward motion, with each dip in velocity representing an optical trap passed by the particle on its forward motion. Note that this is the number of traps passed, rather than the number of traps experienced; i.e. the phase portrait for mode $3(3,0)$ shows two dips, as the particle *passes* two traps on its forward motion, even though it moves forward by three traps.

States $n(n,0)$ have only forward motion, and therefore only show detail on the top half of their phase portraits. This varies from $0(0,0)$, which shows motion of less than one lattice spacing, all the way to $6(6,0)$, which passes 5 traps. States $n(n+1,-1)$ have one backwards step, and therefore also show detail on the lower (reverse) half of the phase portrait. Each closed loop may be thought of as a cycle, which begins at a trap, and ends at a trap n lattice spacings forward. As the end is the beginning of a new cycle, the loop is closed. Modes $n(n+2,-2)$ have two reverse steps, and therefore show a single velocity spike in their lower half, as the particle passes a single trap. Modes with $n = 0$ are symmetric, as the particle experiences no net forward motion, despite having a finite maximum displacement.

5.5 Conclusions

Colloidal particles driven by the sum of constant and oscillating forces through a quasi-one-dimensional periodic optical potential energy landscape have been shown to exhibit very rich non-linear behaviour. Optical microscopy has been used to study such a system, and the trajectories of particles driven using a piezo stage have been determined through live particle tracking. The average velocity of the particles has been measured as a function of the average driving velocity, and dynamic mode locking steps have been observed. These steps represent states of synchronisation, whereby the particle velocity is regulated by the coupling between the oscillations due to the DC drive and the landscape, and the externally imposed modulation. At resonance, the same average velocity is maintained over a range of imposed average driving velocities. This dynamic mode locking has also been presented as phase portraits, whereby the regular repeating nature of the particle motion is elucidated. Locked states manifest as closed loops, in which the particle exhibits repeating behaviour. Between the steps the system is unlocked, resulting in open loops, as the behaviour is no longer regulated. The dependence of the dynamic mode locking on the amplitude and frequency of the modulated part of the driving force is examined, and the effective critical driving velocity and the width of the steps is measured. A state diagram of the amplitude dependent behaviour has been plotted, showing fourteen different dynamic modes. Finally, trajectories and phase portraits of these modes have been used to illustrate the diversity of their microscopic natures.

Acknowledgements

This work was performed in collaboration with Arthur Straube, Dirk Aarts, and Rut Besseling. Alice Thorneywork, Arran Curran, and Urs Zimmermann are thanked for useful discussions.

Chapter 6

Coupled colloidal particles driven over periodic optical potential energy landscapes

Abstract

In this chapter, systems of magnetically interacting colloidal particles are driven with constant and modulated driving forces over periodic optical potential energy landscapes. Three cases from different parts of the parameter space are explored to illustrate the richness of the behaviour in this complex system. Firstly, the critical driving velocity of a chain of coupled particles driven by a constant force is investigated. It is found to depend strongly on the length of the chain and the magnetic field, which may be reminiscent of the Aubry transition. Secondly, a mobile density wave in a chain of coupled particles pinned on an optical potential energy landscape is driven using constant and modulated forces. This 'kink' is found to behave as a quasi-particle, exhibiting dynamic mode locking behaviour analogous to that seen for single particles. It is shown that the 'single particle' dynamics proceed via a similar mechanism. Finally, the mode locking of a finite mobile chain is considered, and the effect of the magnetic field on the internal chain dynamics is examined. A 'breathing' mode seen for flexible chains is found to enhance mode locking.

6.1 Introduction

Imposing an undulating potential energy landscape on a system of interacting particles gives rise to a vast array of structural and dynamic phenomena. Such effects are found in a range of physical systems, from mobile crystal dislocations [178] and surface diffusion [107, 179], to the motion and friction of adsorbed monolayers [87, 130, 180–182]. Phase transitions during epitaxy [183] and age hardening in alloys [184] may also be explained in terms of particles in potential energy landscapes. Even diffusion within living cells has been described in this way [185]. The common factor in all of these systems is the competition between the length scales of the substrate and the adsorbate, which are related to the inter-particle and particle-substrate interactions.

Friction is one of the most studied phenomena of interacting particles in potential energy landscapes [87,130,180–182,186,187]. The simplest model seeking to describe this is the Prandtl-Tomlinson model [4,188], in which a point mass is moved in a one-dimensional periodic potential energy landscape (see figure 6.1a). The Frenkel-Kontorova model is an extension of the Prandtl-Tomlinson model, but retains much of its simplicity [7]. In the Frenkel-Kontorova model, a chain of particles interacting via harmonic springs is placed on a periodic potential energy landscape (see figure 6.1b). Such a model allows for a great variation in the length scale associated with the adsorbed chain, the inter-particle spacing a_0, relative to the spacing of the pinning potential of the landscape, a_s. The ratio of these length scales can therefore be anything from completely commensurate, where $a_0 = na_s$ (where n is an integer), to incommensurate, where there is an irrational relationship between the length scales [189]. This causes emergent structures, such as topological solitons ('kinks' and 'anti-kinks'), which are localised defects in the lattice due to the presence of extra particles (kinks) or vacancies (anti-kinks). These defects have a much higher mobility than the pinned particles in the lattice and move as density waves. Emergent collective dynamic phenomena also occur when the chain is driven across the substrate. For instance, the DC and AC-driven Frenkel-Kontorova model has been extensively studied, from its unlocking mechanism [190], to its dissipative dynamics [177, 191, 192], and its response to noise [193] or a deformable substrate [194]. Various topological aspects of the model, such as kinks and excitations, have been probed [88, 195], and the model has also been used to describe phenomena like cluster mobility and friction on an atomic surface [196, 197], including super-

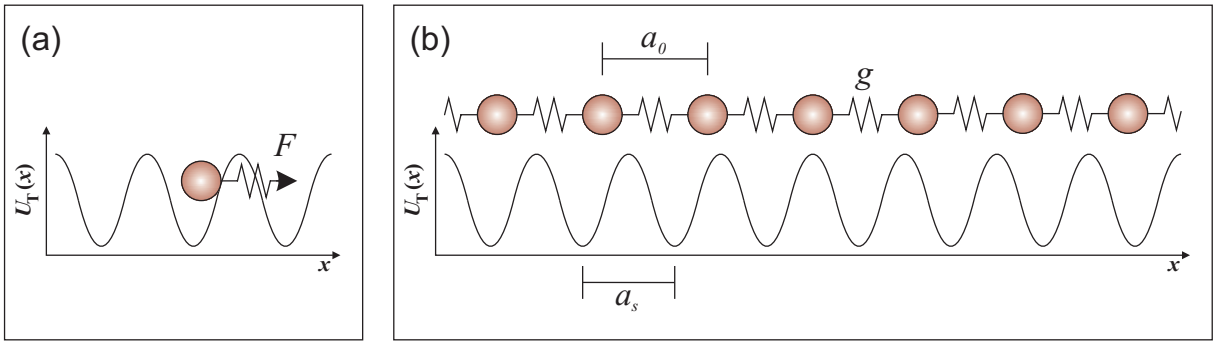


Figure 6.1: Physical models of particles on periodic potential energy landscapes. (a) Prandtl-Tomlinson model: a single particle pulled by a spring over a periodic potential energy landscape. (b) Frenkel-Kontorova model: a chain of particles coupled by springs with stiffness g, such that the particles have preferred spacing of a_0, on a periodic potential energy landscape with wavelength a_s.

lubricity [198].

A particularly interesting result obtained from study of the DC-driven Frenkel-Kontorova model is that of the 'transition by breaking of analyticity' [156], now known as the Aubry transition after its proposer. If the periodic potential energy landscape and the length of the chain of particles are both infinite, and their length scales are incommensurate, then the friction in the system will drop to zero, even in the presence of the potential energy landscape [156]. This occurs because in this case the number of degenerate ground states available is infinite, and the barrier between them is thus zero, resulting in vanishing friction [7]. This cannot be seen in a finite deterministic chain, as there will always be a finite number of ground states, and therefore a finite energy barrier to motion. Modulating the chain's motion can, however, overcome this barrier, leading to a dynamical Aubry transition [199].

Another physical system driven by constant and modulated driving forces which has received considerable recent theoretical and experimental attention is that of mobile vortex lines [113, 120]. These may be treated as chains of interacting quasi-particles moving in a periodic potential energy landscape. As with atomic systems, phase transitions may be induced by the competing length scales [116–118, 200]. Shapiro steps are also seen in such systems in theory [121, 175] and experiments [6, 112, 150, 151]. Also, on the colloidal length scale, the structure and dynamics of systems of interacting particles under the influence of random and periodic optical potential energy landscapes have been studied for a number of years numerically and in experiments [40, 59, 171, 201–205]. As a model system for epitaxy, colloids have proved particularly worthwhile [11]. Where there is a mismatch between the length scales induced by

the substrate potential and the inter-particle spacing various structural effects have been found, including domain formation [43], separation into stripes [162], and phase transitions [42,46]. Dynamic effects similar to those seen in chapter 4 are also seen, including critical pinning potentials, which have been found in both small systems [206] and large monolayers [161]. Furthermore, topological defects, including kinks, have been created and manipulated [35,45,207]. The highly controllable interactions in magnetic systems have made them particularly experimentally interesting, and they have been applied to driving systems and particle sorting [169,208,209].

This chapter considers quasi-one-dimensional chains of coupled super-paramagnetic colloidal particles, driven by constant and modulated forces through periodic optical potential energy landscapes. The particles interact as attractive magnetic dipoles, through a magnetic field imposed collinear to the axis of the potential energy landscape. The imposition of two external fields, optical and magnetic, introduces a competition between the particle separation length scale, which is controlled by the magnetic field and the spacing of the optical traps making up the periodic optical potential energy landscape. Three cases are studied; the first is that of a coupled chain, weakly pinned to the optical potential energy landscape. Here the length scale of particle separation is on the order of the particle diameter. The dependence of the critical driving velocity on the number of particles, the interaction strength, and the wavelength of the optical landscape is studied. The second system is that of a weakly coupled chain, strongly pinned to the optical potential energy landscape, such that a static chain is created. A simple mobile defect in the form of a topological soliton or 'kink' is introduced, and its dynamics in constant and modulated driving forces are studied. Finally, the dynamic mode locking of a finite mobile chain is considered, and the relationship between the flexibility of the chain and the stability of the mode locked states is studied.

6.2 Theory

The experiments in this chapter study clusters of N interacting Brownian colloidal particles, driven by constant and modulated forces in a periodic potential energy landscape. To describe this, the Langevin equation for a single particle (equation 2.8) is adapted, by the addition of a term accounting for the interactions of particle j with the other particles in the cluster,

$F_j(x_1, x_2, \ldots, x_N)$:

$$\zeta v_j = \zeta \frac{\mathrm{d}x_j}{\mathrm{d}t} = F_{\mathrm{DC}} + F_{\mathrm{mod}}(t) + F_{\mathrm{T}}(x_j) + F_j(x_1, x_2, \ldots, x_N) + \xi(t). \tag{6.1}$$

Note that hydrodynamic effects are neglected in this expression. The interaction term is generally very complicated, but by assuming pairwise additivity, a separation dependent interaction force between each pair of particles, $F_{jk}(|x_k - x_i|)$, may be used:

$$\zeta v_j = \zeta \frac{\mathrm{d}x_j}{\mathrm{d}t} = F_{\mathrm{DC}} + F_{\mathrm{mod}}(t) + F_{\mathrm{T}}(x_j) + \sum_{k \neq j}^{N} F_{jk}(|x_k - x_i|) + \xi(t). \tag{6.2}$$

The trapping force, $F_{\mathrm{T}}(x_j)$, is a sum of the M identical Gaussian optical traps making up the periodic optical potential energy landscape, as described in section 4.2 (equation 4.3), such that:

$$F_{\mathrm{T}}(x_j) = -k \sum_{i=1}^{M} (x_j - x_i) \exp\left[-\frac{k(x_j - x_i)^2}{2V_0} \right], \tag{6.3}$$

The particles used here are super-paramagnetic colloidal spheres, which possess a magnetic dipole moment in the presence of a magnetic field (see section 2.2.3). The magnetic interaction energy of a pair of magnetic dipoles depends on the local magnetic field strength, $\mathbf{B}_j$, as shown in figure 2.2a. The pair potential between two such dipolar particles separated by a distance r_{jk} (where $\mathbf{r}_{jk}$ is parallel to $\mathbf{B}_j$) is thus given by (see equation 2.20):

$$U_{jk} = -\frac{\mu_0}{2\pi} \frac{\chi^2 B^2}{r_{jk}^3}, \tag{6.4}$$

The strength of the dipolar inter-particle attraction is often expressed as a dimensionless interaction parameter Γ, which gives the interaction energy at contact of a pair of particles of diameter σ (see figure 2.2b, inset):

$$\Gamma \equiv -\frac{U_{jk}(r_{jk} = \sigma)}{k_{\mathrm{B}}T} = \frac{\mu_0}{2\pi} \frac{\chi^2 B^2}{\sigma^3 k_{\mathrm{B}} T} \tag{6.5}$$

Equation 6.4 leads to the inter-particle force via $F_{jk} = -\partial U_{jk}/\partial r_{jk}$:

$$F_{jk} = -3 \frac{\mu_0}{2\pi} \frac{\chi^2 B^2}{r_{jk}^4} \tag{6.6}$$

Substituting equations 6.3 and 6.6 into equation 6.2 leads to an equation of motion for a particle within a cluster of N particles, driven by constant and modulated forces over a periodic optical potential energy landscape:

$$v_j = \frac{\mathrm{d}x_j}{\mathrm{d}t} = v_{\mathrm{DC}} + v_{\mathrm{mod}}(t) + \frac{1}{\zeta}\left(\sum_{i=1}^{M} k(x_j - x_i)\exp\left[\frac{-k(x_j - x_i)^2}{2V_0}\right] - \sum_{k\neq j}^{N} 3\frac{\mu_0}{2\pi}\frac{\chi^2 B^2}{r_{jk}^4} + \xi(t)\right). \quad (6.7)$$

Although hydrodynamic effects are not included in equation 6.7, hydrodynamics are obviously present in the experiments. Accounting for this in equation 6.7 would make the equation of motion very difficult to solve, and advanced numerical techniques such as stochastic rotation dynamics [210] would be required. Note that the equation of motion is written in terms of velocities, as this is what is measured in the experiments, and externally imposed via v_{DC} and v_{mod}. In this chapter, therefore, (critical) driving *forces* will not be referred to and (critical) driving *velocities* will be used instead.

6.3 Experimental methods

6.3.1 Colloidal model system

The colloidal system used is composed of Dynabeads M-270 (diameter 3 μm), in 20% $\mathrm{EtOH_{aq}}$ (see section 2.4.1), held in a Hellma cell. The coefficient of friction for a single particle, ζ, is found from diffusion to be 9.19×10^{-8} kg s^{-1} (section 2.4.1). The particles are super-paramagnetic, due to single domain magnetic nano-particles encapsulated in the polystyrene matrix. These domains align in the presence of an external magnetic field, causing the particles to obtain a magnetic dipole moment in the direction of the imposed field. In the absence of an external magnetic field, the nano-particle orientations are distributed randomly so no magnetic dipole moment is seen. Chains of particles are created by imposing a homogeneous in-plane magnetic field, such that the dipoles attract. The particles have been found by SQUID magnetometry to have a magnetic susceptibility of $\chi = 6.7 \times 10^{-12}$ A m^2 T^{-1} [84]. Particle concentration is low, such that only the particles required to compose the chains are visible in the field of view.

6.3.2 Experimental setup

The experimental setup consists of an infra-red (1064 nm) laser, controlled using a pair of perpendicular AODs, and focused using a 50×, NA=0.55 microscope objective (see section 2.4.3). The one-dimensional periodic optical landscape, with trap spacings varying from $\lambda = 3.5$ μm to $\lambda = 5.5$ μm, is generated in Aresis Tweez software, controlled from the LabView interface. The traps are time-shared at 5 kHz, such that on the timescale of the particles (with a Brownian time of ~ 50 s, and a driven time of at least ~ $\frac{1}{3}$ s per trap spacing), the traps form a constant potential energy landscape.

The laser power and the total number of traps are held constant throughout each experiment, so that the laser power per trap (and hence the trapping parameters k and V_0) are consistent. The laser power used depends on the experiment, and the laser power per trap at the sample ranges between ~ 0.75 mW and ~ 1.75 mW. This gives typical trapping parameters of trap stiffness, k, of 3.8×10^{-7} kg s^{-2} $\leq k \leq$ 8.7×10^{-7} kg s^{-2}, and trap strength, V_0, of 90 $k_\mathrm{B}T \leq V_0 \leq 200$ $k_\mathrm{B}T$ (see figure 3.5).

The driving force is provided by a PI-542.2CD piezo-stage, controlled using the LabView interface (see section 2.4.5), at driving velocities, v_DC of 0.05 μm s^{-1} $\leq v_\mathrm{DC} \leq$ 10 μm s^{-1}. For the mode locking experiments, an AC driving velocity is added to the DC drive with an amplitude, v_AC, of 1.0 μm s^{-1} $\leq v_\mathrm{AC} \leq$ 5.2 μm s^{-1}, and a frequency, ν, of 0.2 Hz $\leq \nu \leq$ 0.75 Hz. Note that here driving *velocities* are referred to, as discussed in section 6.2.

Homogeneous, in-plane, magnetic fields are provided by a pair of permanent magnets, positioned equidistantly from the sample centre, such that the area within which the experiments are conducted has no detectable magnetic field gradient. Magnetic field strengths depend on the spacing of the magnets, and vary between 0.43 mT $\leq B \leq$ 4.29 mT. The dimensionless magnetic field parameter, Γ (see equation 6.5), therefore varies between ~ 15 and ~ 1500.

Images are focused onto the Ximea CMOS camera using a 40×, NA=0.50 microscope objective. The setting of experimental parameters is automated in the LabView interface, and four to six repeats are made at each driving velocity for each amplitude and frequency of the AC driving velocity. The positions of all of the individual particles in the chain are recorded live at 40 Hz from the camera image (see section 2.4.7).

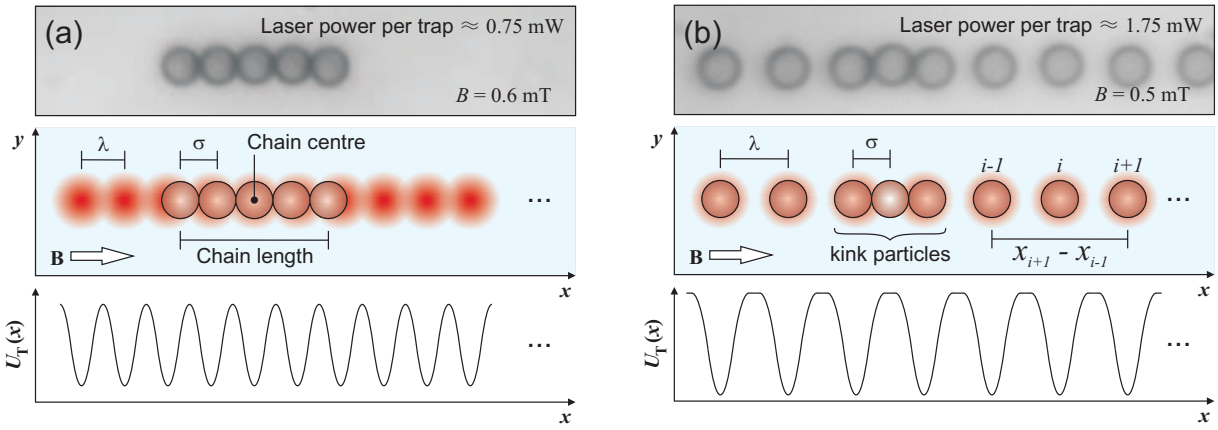


Figure 6.2: Two experimental systems of magnetically coupled colloidal particles. (a) Mobile chain of $N = 5$ particles. $\lambda = 3.5$ μm, $B = 0.6$ mT, laser power per trap 0.75 mW. (b) Static (pinned) chain with a single kink defect. Trap spacing $\lambda = 5.5$ μm, magnetic field strength $B = 0.5$ mT, laser power per trap 1.75 mW.

6.3.3 Critical velocity experiments

The DC driving velocity is iterated to find the critical average driving velocity at which the chain starts to slide irreversibly across the optical potential energy landscape. The resolution of this protocol is 0.05 μm s^{-1}. A chain is said to be pinned to the landscape if it still returns to its starting lattice position after the stage has moved 100 μm, or three minutes has elapsed, whichever happens first. Magnetic field strengths below 0.43 mT are not considered, as below this level the chains tend to break up irreversibly when driven, rather than remaining contiguous.

6.3.4 Average velocity experiments

The average chain velocity for mobile chains (see figure 6.2a) is found by linearly fitting the trajectory of the centre of the chain, $x(t)$, defined as the mean of the positions of the terminating particles. Instantaneous velocity is found by taking the numerical derivative of $x(t)$. The phase, φ, is found from $x(t)$ data by subtracting the line of average velocity, and multiplying by $2\pi/\lambda$, as explained in section 5.3.3. Phase velocity, $\frac{d\varphi}{dt}$, is calculated by subtracting average velocity from the instantaneous velocity, and then multiplying by $2\pi/\lambda$, as is also shown in section 5.3.3. The phase and phase velocity for a kink are therefore defined as:

$$\varphi = \frac{2\pi}{\lambda}\left(x(t) - \overline{v}t\right) \quad \text{and} \quad \frac{d\varphi}{dt} = \frac{2\pi}{\lambda}(v(t) - \overline{v}). \tag{6.8}$$

The phase velocity is plotted against phase to form phase portraits. Additionally, the chain length, L, is defined as the difference between the first and last particles' co-ordinates.

The position of a kink in a static chain (see figure 6.2b) is determined from the reduced local number density along the chain. The one-dimensional number density is defined as $\rho = N/L$, where N is the number of particles and L is the chain length. The reduced number density is defined as $\tilde{\rho} = \rho\lambda = N\lambda/L$. The reduced local number density around a particle, $\tilde{\rho}_i$, is therefore calculated using the positions of the particle's nearest neighbours:

$$\tilde{\rho}_i = \frac{2\lambda}{x_{i+1} - x_{i-1}}, \tag{6.9}$$

where x_i is the position of particle i. This will be referred to henceforth as 'local density'. Local density is found for all of the particles in the chain except the terminating particles, which have only one neighbour. The local number density far away from the kink particles is found to be $\tilde{\rho}_i \approx 1$, but the kink particles and their nearest neighbours will have higher density (see figure 6.3d). The centre of the kink is subsequently found by the following weighted average:

$$x_{\text{kink}} = \frac{\sum_{i=1}^{N} x_i(\tilde{\rho}_i - 1)}{\sum_{i=1}^{N}(\tilde{\rho}_i - 1)}. \tag{6.10}$$

Figure 6.3 illustrates the different stages in locating the position of a kink. Panel (a) shows the movement of a kink one lattice spacing to the right, such that the kink centre passes from particle 3 (A) to particle 4 (C), via configuration (B). Figure 6.3b shows the local density distribution between particles 2 and 7, and shows that at A (C), there is a sharp peak around particle 3 (4), while at B the density is evenly distributed between the two particles. The kink trajectory determined using equation 6.10 is shown in figure 6.3c. Figure 6.3d shows a contour plot of local density, for the motion of a kink along an entire chain. The particle trajectories and the kink position determined from the density plot are shown in figure 6.3e.

The average kink velocity is found by linearly fitting to the kink trajectory $x_{\text{kink}}(t)$. The instantaneous velocity, $v_{\text{kink}}(t)$, is found by taking the numerical derivative of the kink trajectory $x_{\text{kink}}(t)$. The phase and phase velocity are found as described above and in section 5.3.3, and are used to construct phase portraits.

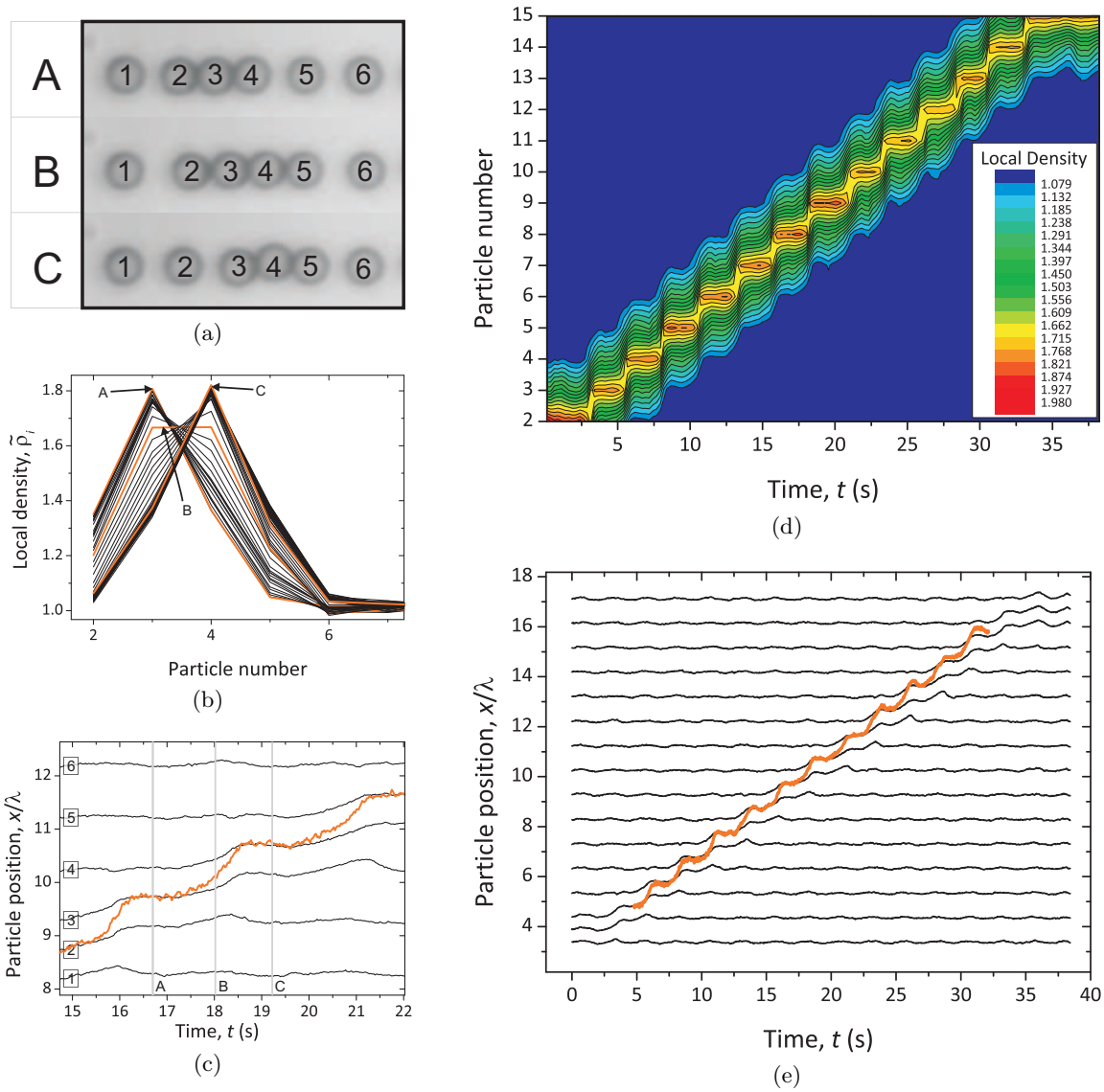


Figure 6.3: Characterisation of the position of a kink. (a) Experimental image, showing a kink moving a single lattice spacing (time runs A→C). (b) The local density profile along the chain. Each line represents a single time. — Lines A→C are representative of the configurations shown in (a), and show that the kink moves as a travelling density wave. (c) — Located kink position as a function of time. — Individual particle trajectories for particles 1-6. Times A→C are representative of the configurations shown in (a). (d) Local density as a function of time. (e) — Particle trajectories, — Kink trajectory.

6.4 Results and discussion

Introducing multiple coupled colloidal particles to the periodic optical potential energy landscapes considered throughout this thesis creates a rich and vast parameter space, through the addition of variability in the number of particles and the (magnetic) interaction strength. These parameters further act in combination with the spacing and strength of the optical potential to introduce commensurability effects. In this chapter, results are presented from three multi-particle systems, which offer complimentary insights into the rich phenomenology of the parameter space. The first system is a mobile chain driven by a constant driving velocity. The second system is a pinned incommensurate chain, with a mobile kink, which is driven by both constant and modulated driving velocities. Finally, a mobile chain is driven by constant and modulated driving velocities.

6.4.1 Critical velocity of coupled particles driven by a constant velocity

In this section, the critical velocity of a chain of super-paramagnetic colloidal particles driven by a constant driving velocity in a periodic optical potential energy landscape is examined. The same sinusoidal optical potential energy landscape used in Chapter 5 is used, with a trap spacing of λ = 3.5 μm, and a total laser power of 350 mW. This is also compared to landscapes with λ = 3 μm and λ = 4 μm. A magnetic field of strength B is imposed collinear with the axis of the one-dimensional optical potential energy landscape, such that the particles attract each other. The dipolar attraction between the particles introduces an additional length scale to the system, as at high magnetic fields the particles will form a chain with an inter-particle separation corresponding to the particle diameter, σ = 3.0 μm. The inter-particle spacing will be a function of B, and will compete with the wavelength of the optical potential energy landscape, λ, such that the particle spacing, r, will lie between the two. Along the length of the chain, this will result in particles being displaced from trap centres by varying amounts.

This competition between length scales will have consequences for the motion of the chain when it is driven across the landscape. The critical driving velocity may no longer be thought of as the barrier for a single particle to escape a single potential well, but rather as the barrier over which the whole chain must pass. This is a more complex problem than that of a single particle,

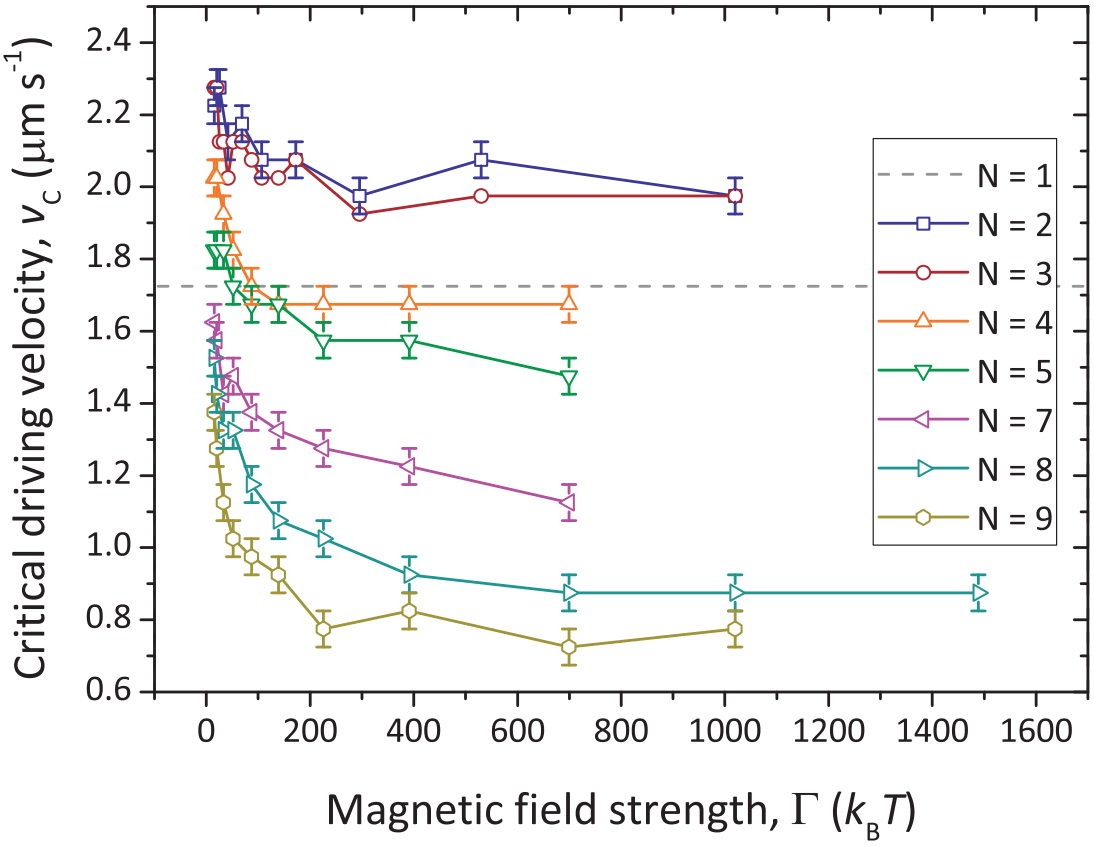


Figure 6.4: Critical driving velocity as a function of magnetic field strength, for chains containing N particles, driven over a sinusoidal optical potential energy landscape with a trap spacing of $\lambda = 3.5$ μm. - - - critical driving velocity, v_{DC}, for a single particle (see section 4.4.2).

as it depends on whether the chain is commensurate or incommensurate with the lattice spacing of the periodic potential energy landscape.

Figure 6.4 shows the measured critical driving velocity of chains of particles consisting of 2 to 9 particles, as a function of the magnetic field strength. The critical driving velocity for a single particle (from section 4.4.2) is also indicated. The first observation is that the critical driving velocity clearly decreases as a function of magnetic field strength, B, for all chain lengths, N. At low magnetic fields, the particles are largely localised to the minima in the sinusoidal optical potential energy landscape, such that the spacing between the particles becomes approximately the same as the trap spacing, λ. As B increases, the attraction between the particles increasingly overcomes the barriers between individual minima of the optical potential energy landscape, and the particle spacing moves away from λ, and tends towards the particle diameter, σ. The increase in the mismatch between the length scales leads to an increase in incommensurability. As a result, fewer particles will be located in potential energy minima, and more will be high on the potential energy landscape, leading to a small barrier to motion, and hence a smaller v_C.

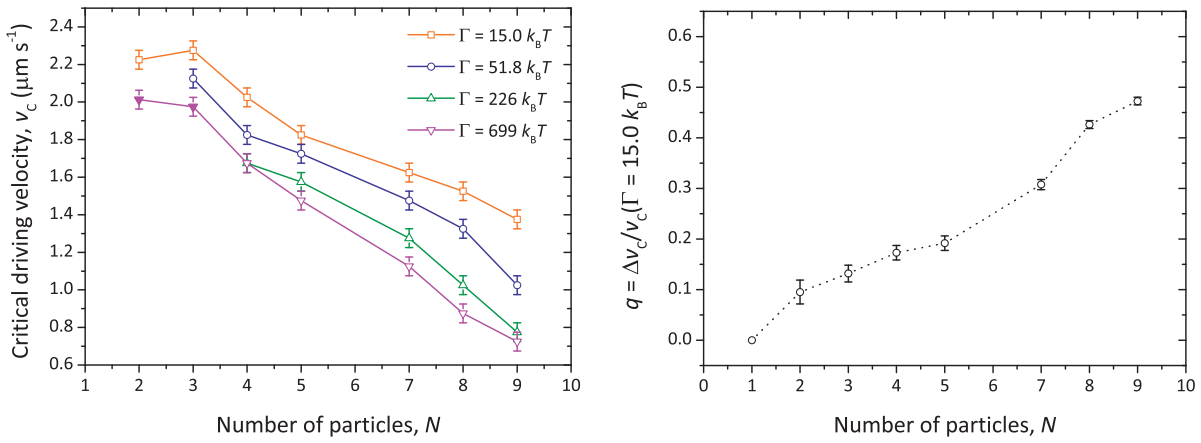


Figure 6.5: Critical chain driving velocity as a function of chain composition. (a) Critical driving velocity for four representative values of magnetic field strength (data from figure 6.4). Filled symbols are interpolated values. (b) Ratio of decrease in critical driving velocity in figure 6.5a to $\Gamma = 15.0\ k_BT$ ($B = 0.43$ mT) value, plotted against the number of particles, N.

The next observation to make from figure 6.4 is that the critical driving velocity clearly decreases with increasing chain length. This effect is shown more clearly in figure 6.5a, where the critical driving velocity is plotted against the number of particles, N, for several values of the magnetic field strength, B. As discussed above, increasing the magnetic field strength increases the incommensurability of the chain on the periodic optical potential energy landscape. When the number of particles is small, i.e. $N = 2$ or 3, this will manifest as symmetrical displacements of the particles, such that the distance between the terminating particles decreases with increasing B, but the centre of mass changes position little. As N increases further, this 'end-effect' becomes less prominent, as the incommensurability is spread over more particles. This has the effect that the chain gains more degenerate ground states, which are increasingly close together as N increases, and therefore have a lower barrier between them. This results in a decrease in the critical driving velocity as the chain length increases at constant magnetic field. This effect is reminiscent of the Aubry transition [156, 199], and has exactly the same basis.

Intriguingly, this decrease in the critical driving velocity with increasing N is greater at higher magnetic fields. This effect may be quantified by finding the difference between the critical driving velocity at high and low magnetic fields, normalised by the low magnetic field value:

$$q = \frac{\Delta v_C}{v_C(\Gamma = 15.0\ k_BT)} = \frac{v_C(\Gamma = 15.0\ k_BT) - v_C(\Gamma = 699\ k_BT)}{v_C(\Gamma = 15.0\ k_BT)}. \tag{6.11}$$

Figure 6.5b plots q against the number of particles in the chain. As well as v_C decreasing with B and N, figure 6.5b shows that the effect of B increases considerably with increasing N. This further demonstrates the importance of the chain length, and the number of degenerate ground states, which increases rapidly with N.

Effect of trap spacing

Next the effect of a small change in the trap spacing, λ, is considered. It was noted above that the level of incommensurability in the system depends on the difference between the particle spacing, which is variable with the magnetic field strength, B, and the trap spacing, which is fixed. It is therefore expected that changing λ will have an effect on the incommensurability, and consequently the critical driving velocity. Figure 6.6 shows the critical driving velocity for chains containing $N = 2, 5, 10$ particles, driven over periodic optical potential energy landscapes with $\lambda = 3$ μm (figure 6.6a) and $\lambda = 4$ μm (figure 6.6b). For the case where $\lambda = 4$ μm, the critical driving velocity depends on N and B in the same way as for $\lambda = 3.5$ μm (figure 6.4). There is a much stronger effect, however, due to the increase in incommensurability caused by increasing the trap spacing. In fact the critical driving velocity drops to almost zero for high magnetic field strengths. The inset on figure 6.6b shows the same data, plotted on a vertical log axis. Figure 6.6a shows that when $\lambda = 3$ μm, however, the behaviour is completely different. Now the effect of B on the critical driving velocity is small, and even at $N = 10$, v_C passes through a minimum before increasing again towards the values for $N = 2$ and 5. It is important to note here that the chain is always commensurate with the landscape, as the trap spacing is equal to the particle diameter. Based on the arguments above, there should therefore be no dependence on N or B. The effects at small magnetic field seen in the graph are due to the softness of the chain. When the chain is driven, it may deform slightly in order to attain a more favourable configuration to overcome the barriers in the potential energy landscape. This flexibility decreases greatly with increasing B, so the critical driving velocity increases again.

Anomalous behaviour for small clusters

Finally, the anomalously high critical driving velocities seen for small chains are considered. The single particle critical driving velocity is plotted on figures 6.4, 6.6a, and 6.6b as a dashed line,

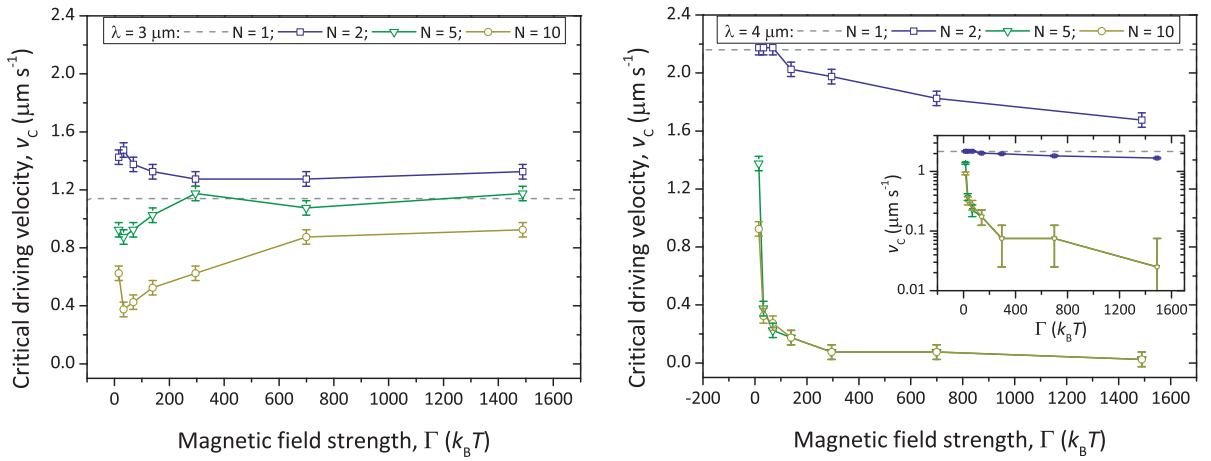


Figure 6.6: Critical driving velocity as a function of magnetic field strength for several chain lengths, for trap spacings: (a) $\lambda = 3$ μm, (b) $\lambda = 4$ μm. The inset in (b) shows the same data plotted with a vertical log scale. Note that the data for $N = 5$ and $N = 10$ lie almost on top of each other.

and although most of the chains have a critical driving velocity below the single particle value for most values of N and B, some small chains ($N \approx 2 \rightarrow 4$) can have critical driving velocities *higher* than the single particle value. This is remarkable, and not yet fully understood. One possible explanation is that the N dependence of the friction coefficient and the optical force are not the same. The increase in the optical force with N is likely to be approximately linear, but it was shown in figure 3.8 that the increase in ζ_{Cluster} is certainly not linear with N, at least for small clusters. As the critical driving force is that required to overcome the optical force, this would imply a non-linear relationship between the critical driving force (and velocity) and N.

6.4.2 Dynamic mode locking of a kink in a static chain

The dynamics of a single colloidal particle driven by DC and AC driving forces across a periodic optical potential energy landscape was studied in Chapters 4 and 5. Here, a constant and modulated driving velocity is applied to a system consisting of sixteen particles in a one-dimensional optical potential energy landscape consisting of fifteen traps (see figure 6.7). The presence of the extra particle causes a local increase in density, which is known as a topological soliton or kink [211]. Kinks are known to behave as quasi-particles, and move as density waves when driven [35, 88, 212]. In the case studied here, the optical trapping force is high, so that the chain is stationary but the kink is mobile. The trap spacing is set at $\lambda = 5.5$ μm, such that the free space between particles is 2.5 μm. The 'extra' particle is forced to lie along the axis of the rest

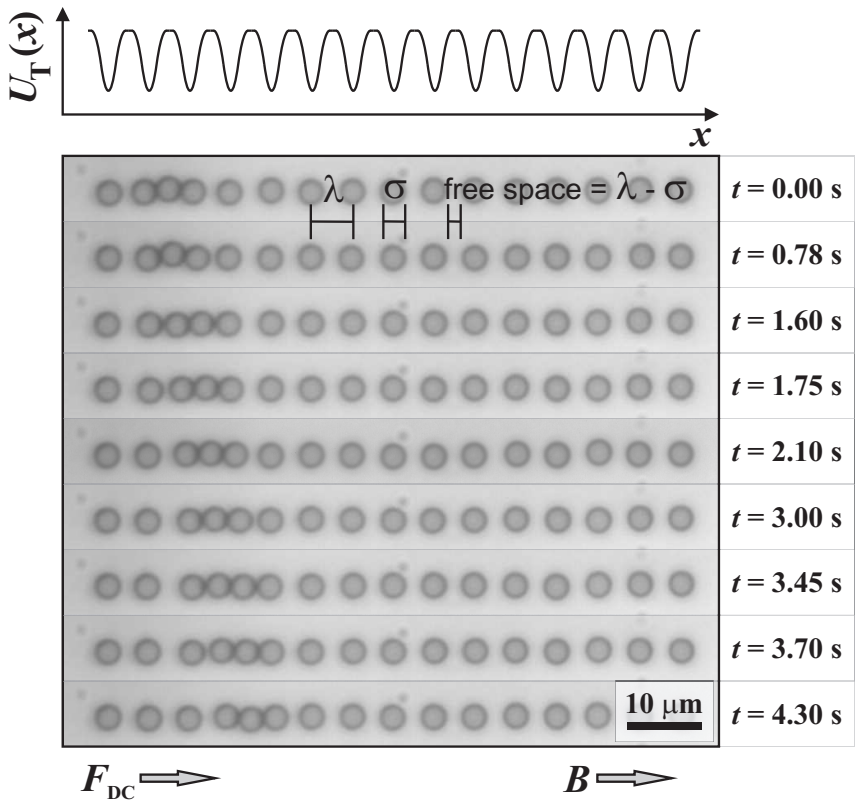


Figure 6.7: A chain of 16 3.0 μm super-paramagnetic colloidal particles spread over 15 minima of a periodic optical potential energy landscape with a wavelength of 5.5 μm, such that a kink forms. A driving velocity of v_{DC} = 1.9 μm s^{-1} is applied along the chain, collinear with a magnetic field of Γ = 20.2 k_BT (B = 0.50 mT).

of the chain using a magnetic field. The field is required as the immediate neighbours of the extra particle must be slightly displaced in order to accommodate the extra particle, which has a diameter of 3 μm, slightly more than the space between particles. In the absence of a magnetic field, the particle will sit out of the line of the chain [103, 172].

Figure 6.7 shows the system of sixteen particles overloading a line of fifteen traps, and the kink is easily identified as an increase in the local density due to the presence of the extra particle. When a constant driving velocity is applied, the kink is able to move, by displacing individual particles away from their equilibrium positions. Importantly, individual particles do not move very far, and have a maximum displacement of $\sim \lambda$. This means that the kink is using the free space between particles to migrate, with the consequence that the kink may move more quickly than the driving velocity. Indeed, in figure 6.7 the centre of the kink moves two lattice spacings in 4.3 seconds, which corresponds to an average kink velocity of $\overline{v} \approx 2.5$ μm s^{-1}, compared to a driving velocity of v_{DC} = 1.9 μm s^{-1}.

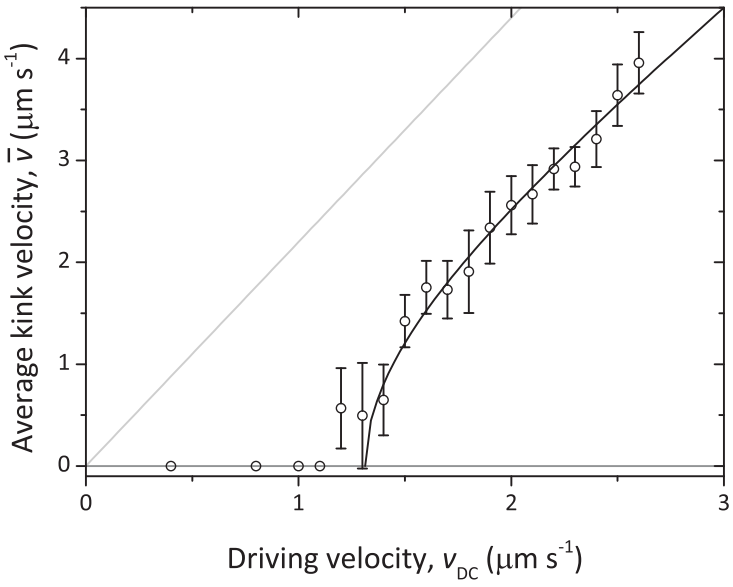


Figure 6.8: Average kink velocity against driving velocity, for a chain of 16 particles in 15 traps spaced by $\lambda = 5.5$ μm. ○ experimental data (error bars represent the standard deviation of the repeats). — fit corresponding to a sinusoidal potential energy landscape, $\overline{v} = \sqrt{v_{DC}^2 - v_C^2}$. — Driving velocity scaled by the free space in the chain $v_{DC,eff} = \frac{5.5}{2.5} v_{DC}$.

Average kink velocity

The average velocity, $\overline{v}$ of the kink as a function of a constant driving velocity is shown in figure 6.8. Just as with the single particle data shown in figure 4.4, at low driving velocities there is no movement, as the kink is pinned, but above a critical driving velocity the kink starts to move. The velocity initially increases rapidly with increasing driving velocity, and then the rate of increase subsides and the curve becomes linear. The experimental data in figure 6.8 is fitted with the expression for the average velocity for a single particle on a sinusoidal optical potential energy landscape, $\overline{v} = \sqrt{v_{DC}^2 - v_C^2}$ (see section 4.2.1, equation 4.16). The equation describes the data here excellently, despite the fact that the landscape is relatively widely spaced, with $\lambda = 5.5$ μm. For a single particle, it was found in Chapter 4 that the periodic optical potential energy landscape is not well described by a single sinusoidal term above $\lambda = 4$ μm. Here, however, it is necessary to consider the fact that the kink is much larger than a single particle, and is composed of several individual coupled particles, which all see different parts of the potential energy landscape. The upshot is that a larger object is sampling the potential energy landscape, extending the sinusoidal approximation to larger wavelengths of the landscape. The final (grey) line on figure 6.8 shows the driving velocity, scaled by the free space in the chain, such that $v_{DC,eff} = \frac{5.5}{2.5} v_{DC}$ as this is the effective maximum velocity of the kink.

Dynamic mode locking of a kink

Next, the dynamics of a kink driven by constant and modulated driving velocities are examined. Figure 6.9a shows the average velocity of a kink driven with a modulated driving force with amplitude v_{AC} = 2.0 μm s^{-1}, and frequency ν = 0.2 Hz. Just as has been shown previously for a single particle (see Chapter 5), the average kink velocity against driving velocity shows a smaller critical driving velocity relative to the constant drive case. Then the kink velocity increases, until it reaches a plateau at a velocity corresponding to the lattice spacing multiplied by the frequency, $\overline{v} = \lambda\nu$. Then the kink velocity increases again, until another step is reached, at twice the velocity of the previous one, $\overline{v} = 2\lambda\nu$. These steps again correspond to resonant modes of the system, with the kink moving forward an integer number of lattice spacings in a single period of the modulation of the driving velocity, and are equivalent to the Shapiro steps in Josephson junctions [155].

The nature of the dynamic modes can be elucidated by inspecting the kink trajectories shown in figure 6.9b. The four lines show single kink trajectories at four different driving velocities, as shown in figure 6.9a. The first trajectory is for a point just below the first mode locked step (v_{DC} = 0.55 μm s^{-1}) and, although almost regular, does not have a perfectly periodic nature. The next, at v_{DC} = 1.00 μm s^{-1}, corresponds to a point on the first mode locked step, and has a perfectly periodic nature. Figure 6.9c(B) shows the trajectory for a single period of the oscillation, showing that this is a 1(1,0) mode. This is highlighted more clearly in figure 6.9e, where the phase portrait shows that each cycle of the oscillation results in the same velocity oscillation, giving a regular closed-loop structure. In contrast, the phase portrait for the point just below the first step is not a closed loop (see figure 6.9d). The final two trajectories are for driving velocities between the first and second step (v_{DC} = 1.30 μm s^{-1}), and on the second step (v_{DC} = 1.90 μm s^{-1}). For the latter, figure 6.9c(D) shows the trajectory for a single period of the oscillation, showing that this is a 2(2,0) mode. Figure 6.9f and 6.9g show that again there is an irregular open-loop structure in the phase portrait of the first of these lines, and a regular closed-loop for the point on the step. It is important to note here that the phase portraits for kink motion resemble closely those for a single particle shown in figure 5.4. This means that the behaviour of a kink is analogous to that of a single particle on a periodic optical potential energy landscape, despite being a mobile density wave, rather than a single particle.

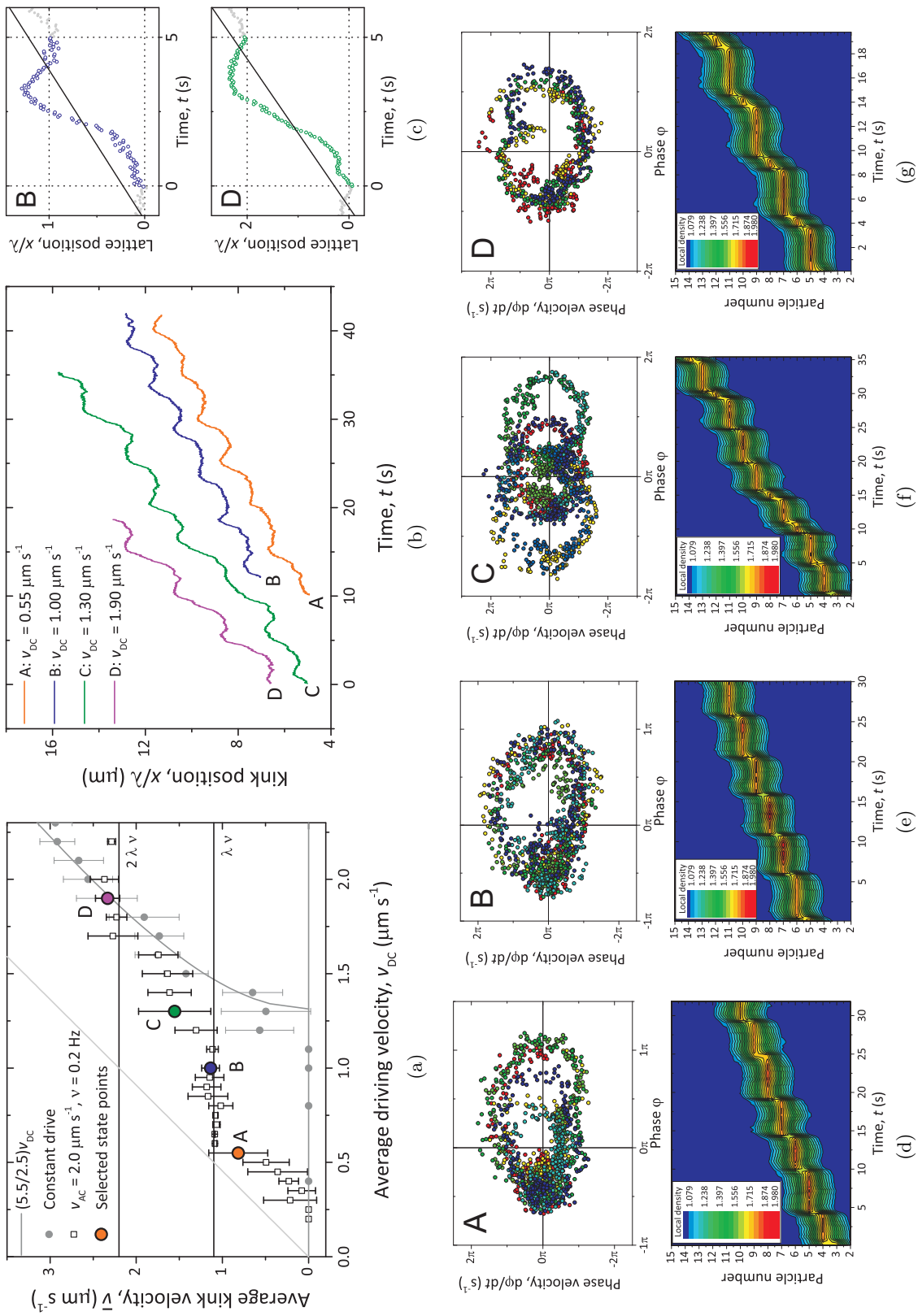
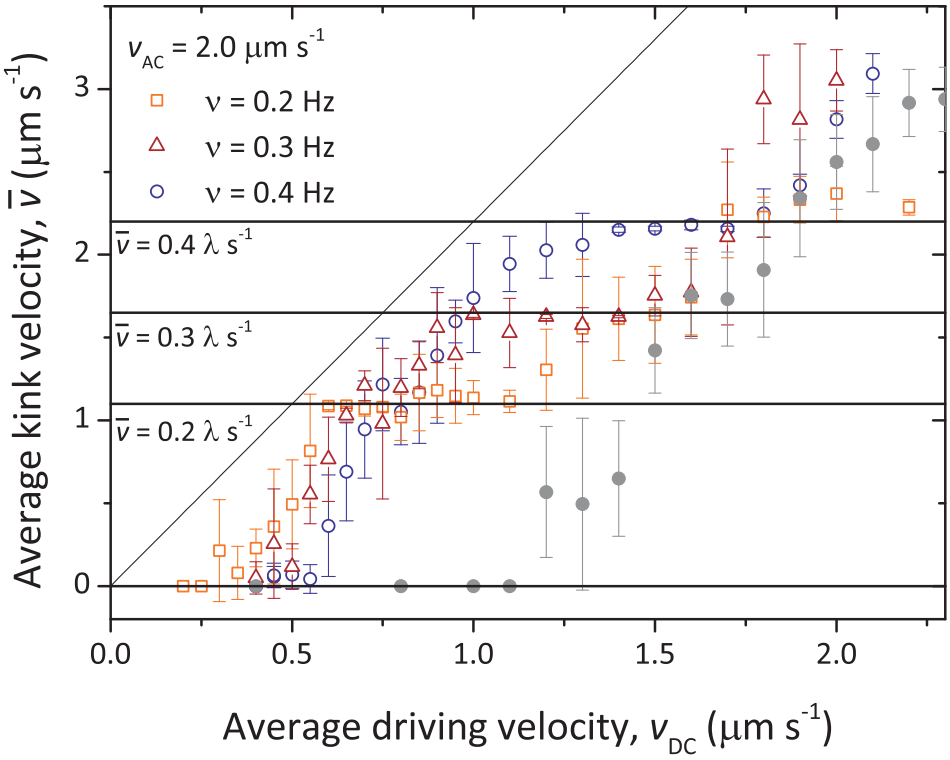
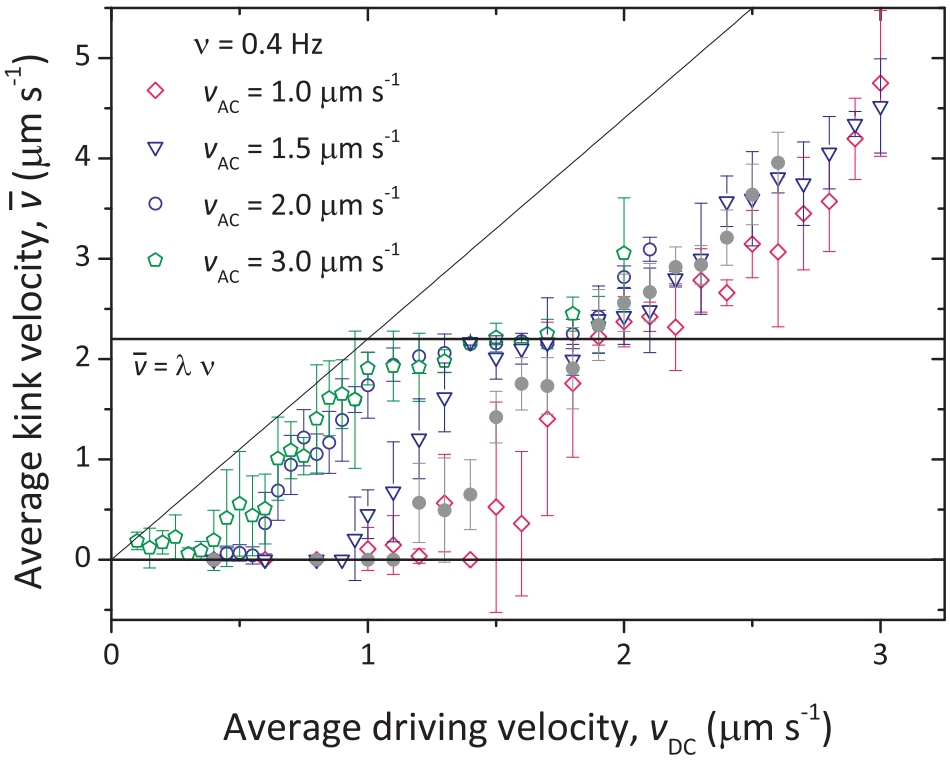


Figure 6.9: Mode locking of a kink driven with constant and modulated drive, at v_{AC} = 2.0 μm s^{-1} and ν = 0.2 Hz. (a) Four points on the staircase. (b) Simple kink trajectories, $x(t)$. (c) Single periods of the oscillation for points on step 1 (B) and step 2 (D). (d-g) Phase portraits and density plots for the four selected state points: (d) v_{DC} = 0.55 μm s^{-1}, (e) v_{DC} = 1.00 μm s^{-1}, (f) v_{DC} = 1.30 μm s^{-1}, (g) v_{DC} = 1.90 μm s^{-1}.



(a)



(b)

Figure 6.10: Frequency and amplitude dependence of the average kink velocity in a chain of 16 particles in a periodic optical potential energy landscape of 15 traps spaced by $\lambda = 5.5$ µm, driven by a constant and modulated driving force, in a linear in-plane magnetic field of strength $\Gamma = 20.2\ k_B T$ ($B = 0.5$ mT). (a) Frequency dependence. (b) Amplitude dependence.

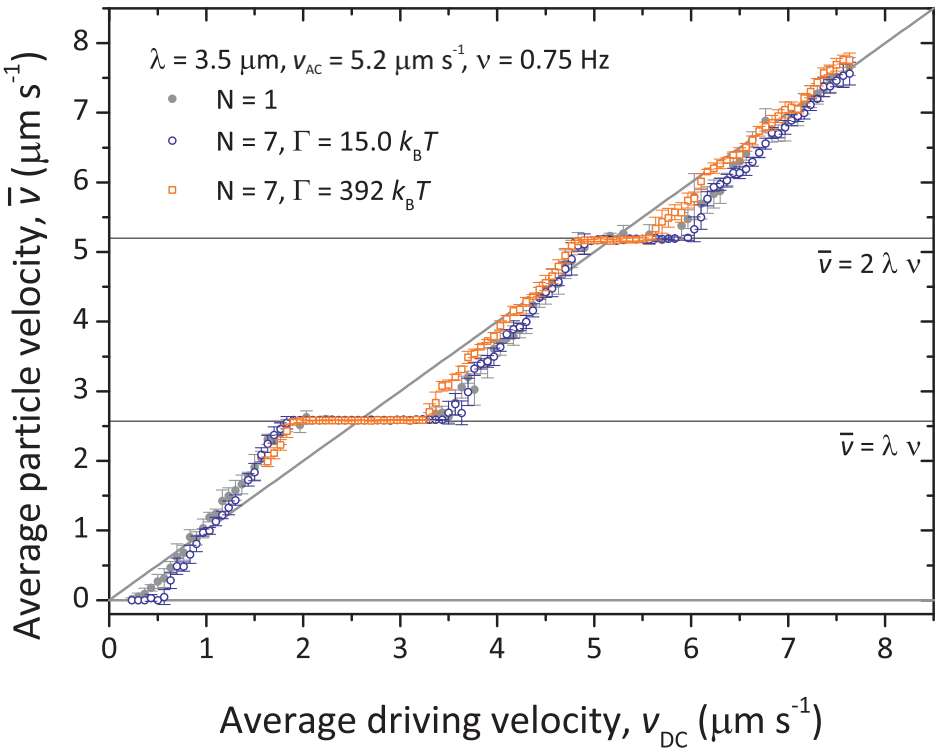
Frequency and amplitude dependence of dynamic mode locking

As for the single particle case, the nature of the mode locked steps for driven kinks depends on the frequency (see section 5.4.3) and amplitude (see section 5.4.4) of the modulated part of the driving velocity. Figure 6.10a shows the 'Devil's staircases' for three different frequencies (ν = 0.2, 0.3, 0.4 Hz) for a single amplitude of v_{AC} = 2.0 μm s^{-1}. The behaviour of the kink, although less well resolved due to its speed, shows remarkable resemblance to the case of a single particle shown in figure 5.5. The average velocity corresponding to the first step increases with the frequency, as expected, such that $\overline{v} = n\lambda\nu$. Figure 6.10b compares mode locked steps for four different amplitudes (v_{AC} = 1.0, 1.5, 2.0, 3.0 μm s^{-1}) at a frequency of 0.4 Hz. Once more, the kink reproduces the behaviour seen for a single isolated particle (see e.g. figure 5.8). The step lies at the same velocity for all of the lines, as the frequency is the same. For low amplitude, the critical driving velocity is very close to that for the case of constant drive, and the step is almost too small to resolve, but as the amplitude increases, the critical driving velocity decreases and the step width increases.

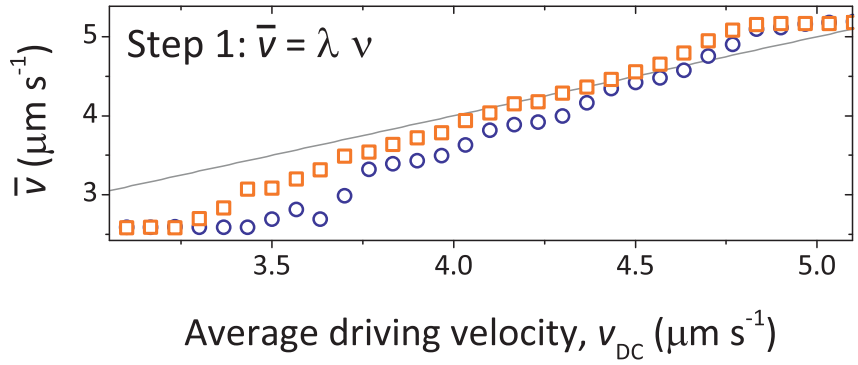
6.4.3 Dynamic mode locking of a finite mobile chain

The previous two sections have considered the pinned to sliding transition for a mobile chain, and the dynamic mode locking of a driven kink in a static chain. Here, we consider the dynamic mode locking of a finite mobile chain, driven across a sinusoidal optical potential energy landscape by constant and modulated driving velocities. Although the dipolar attraction between the particles in the chain is always sufficient to keep the cluster together as a single entity, some flexibility in the length of the chain is retained. By varying the strength of the dipolar interaction relative to the strength of the optical potential energy landscape, it is possible to control this flexibility. In this section, the effect of chain flexibility on dynamic mode locking is studied.

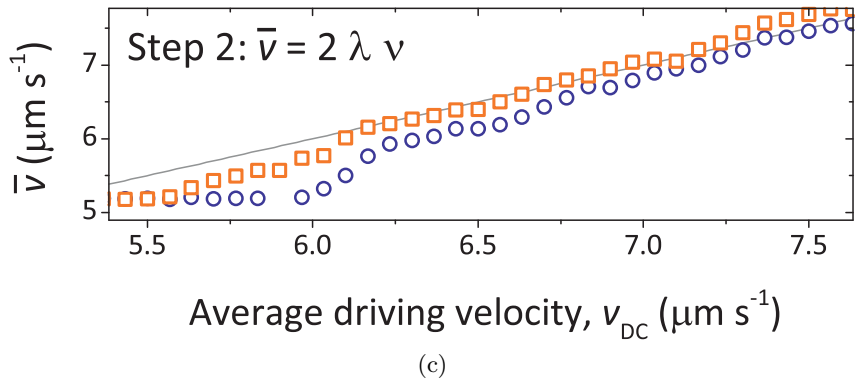
In order to probe this effect, a chain of seven particles is driven across a quasi-one-dimensional periodic optical potential energy landscape with constant and modulated driving velocities, at two different inter-particle interaction strengths. The periodic optical potential energy landscape used has a wavelength of λ = 3.5 μm. The modulated part of the driving velocity has an amplitude of v_{AC} = 5.2 μm s^{-1}, and frequency of ν = 0.75 Hz. The strength of the magnetic field was set at Γ = 15.0 $k_{\mathrm{B}}T$ (B = 0.43 mT) and Γ = 392 $k_{\mathrm{B}}T$ (B = 2.2 mT). At



(a)



(b)



(c)

Figure 6.11: (a) Dynamic mode locking for chains of N = 7 particles driven across a periodic optical potential energy landscape with a wavelength of λ = 3.5 μm, compared to the single particle case for the same modulated driving velocity, with v_{AC} = 5.2 μm s^{-1} and ν = 0.75 Hz (figure 5.3). □ N = 7, Γ = 15.0 $k_B T$ (B = 0.43 mT); ○ N = 7, Γ = 392 $k_B T$ (B = 2.2 mT); • N = 1; — no traps line from figure 2.10a. (b) and (c) show N = 7 cases at the second critical point of each step.

the higher interaction strength, the chain is completely rigid, and the inter-particle spacing is equal to the particle diameter. At the lower interaction strength, however, the chain is flexible and the spacing is on average larger than σ.

Figure 6.11 shows the average velocity of the chains as a function of driving velocity, compared to the case of a single particle (see section 5.4.1, figure 5.3). Similarly to the single particle case, dynamic mode locking steps are observed. At first glance, the lines are all identical. In all three cases, mode locked steps appear at the same average velocities, equal to integer multiples of $\lambda\nu$. However, the difference becomes clear at the second critical point of each mode locked step (see figures 5.1a and 5.3). Panels (b) and (c) on figure 6.11 show the second critical point of each of the two mode locked steps, and it is seen that for both of the steps, the flexible chain (Γ = 15.0 $k_{\mathrm{B}}T$) exits the step at a higher average driving velocity than the stiffer chain (Γ = 392 $k_{\mathrm{B}}T$). No effect on the first critical points is seen. The narrower step width of the stiffer chain implies that it more easily passes the transition from a locked to an unlocked state. The flexible chain, however, is able to persist in a frequency locked mode over a significantly larger range of driving velocities, making the steps ~ 0.33 μm s^{-1} wider than those of the stiff chain. This suggests that the flexibility enhances the mode locking, by increasing the second critical velocity. This may be expected, as in a flexible chain, more of the particles are able to lie lower on the landscape, making the particle separation more commensurate with the wavelength of the potential energy landscape, thus increasing the force required to overcome the barrier to a transition to an unlocked state (see section 6.4.1).

In order to understand this effect, the single particle dynamics of the clusters are analysed in detail. For simplicity, a single point on each of the two mode locked steps is examined for the stiff and flexible chains. The average driving velocities of the points on the steps are v_{DC} = 2.500 μm s^{-1} (step 1) and v_{DC} = 5.233 μm s^{-1} (step 2). Figures 6.12a,b (stiff chain) and 6.13a,b (flexible chain) show the particle trajectories for all seven particles in the chain for the first and second steps. The bottom right insets in figures 6.12a,b (stiff chain) and 6.13a,b show the corresponding chain centre trajectories for single periods of the oscillation, and the top left insets show phase portraits. Because mode locked states have been chosen, the trajectories are periodically repeating, and the phase portraits show closed loops, corresponding to 1(1,0) and 2(2,0) modes. Chain centre trajectories, however, cannot show the collective dynamics responsible for the step width difference seen in figure 6.11.

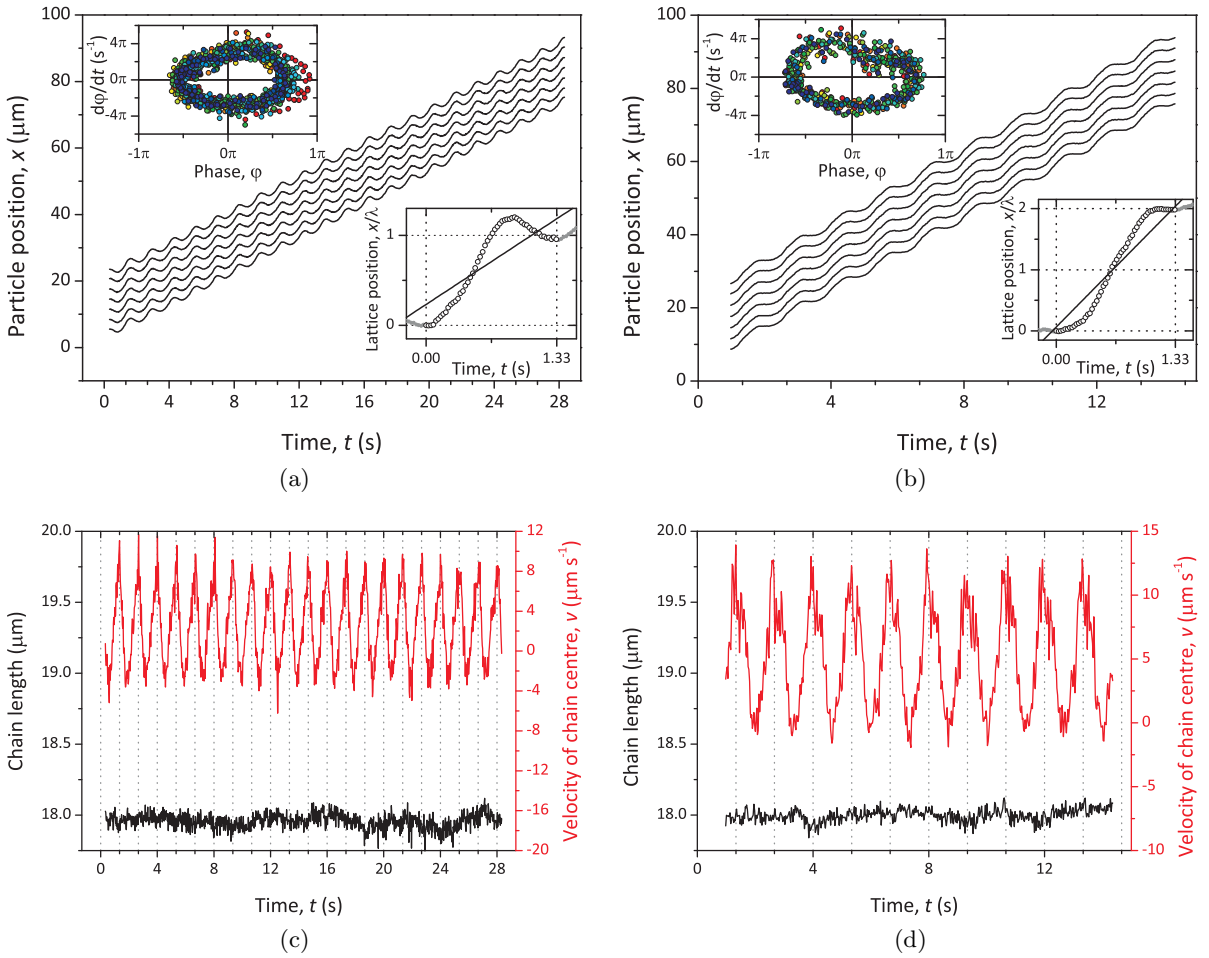


Figure 6.12: Chain of 7 particles in a magnetic field of strength $\Gamma = 392 k_B T$ ($B = 2.2$ mT), driven by a stage velocity of: (a,c) $v_{DC} = 2.500$ μm s^{-1}, (b,d) $v_{DC} = 5.233$ μm s^{-1}. (a,b) Trajectories for all 7 chain particles. Top left inset: phase portrait for the chain centre. Bottom right inset: single period of the oscillation of the chain centre. (c,d) Chain length (— bottom), and chain centre velocity (— top).

The easiest probe of the collective dynamics within the chain is to measure its length. Panels (c) and (d) of figures 6.12 and 6.13 compare the length of the chain over time to the instantaneous velocity of the chain centre. The length of the stiff chain at high magnetic field strength for both steps (figure 6.12c,d) thermally fluctuates around ~ 18 μm, which corresponds to $(N-1)\sigma$, implying that generally all particles are touching. Importantly, there is no correlation between the chain length and the instantaneous velocity. When the chain is flexible, however, the story is quite different (see figure 6.13). Here the chain length is found to distinctly fluctuate. For the first step (figure 6.13c), the fluctuations are on the order of 0.75 μm, around ~ 18.5 μm. Strikingly, they occur at exactly the frequency of the cluster velocity fluctuations, but exactly out of phase, such that the chain is at its maximum length when it is travelling at its minimum velocity. The chain is generally stretched by the landscape to be longer than 18 μm, and is

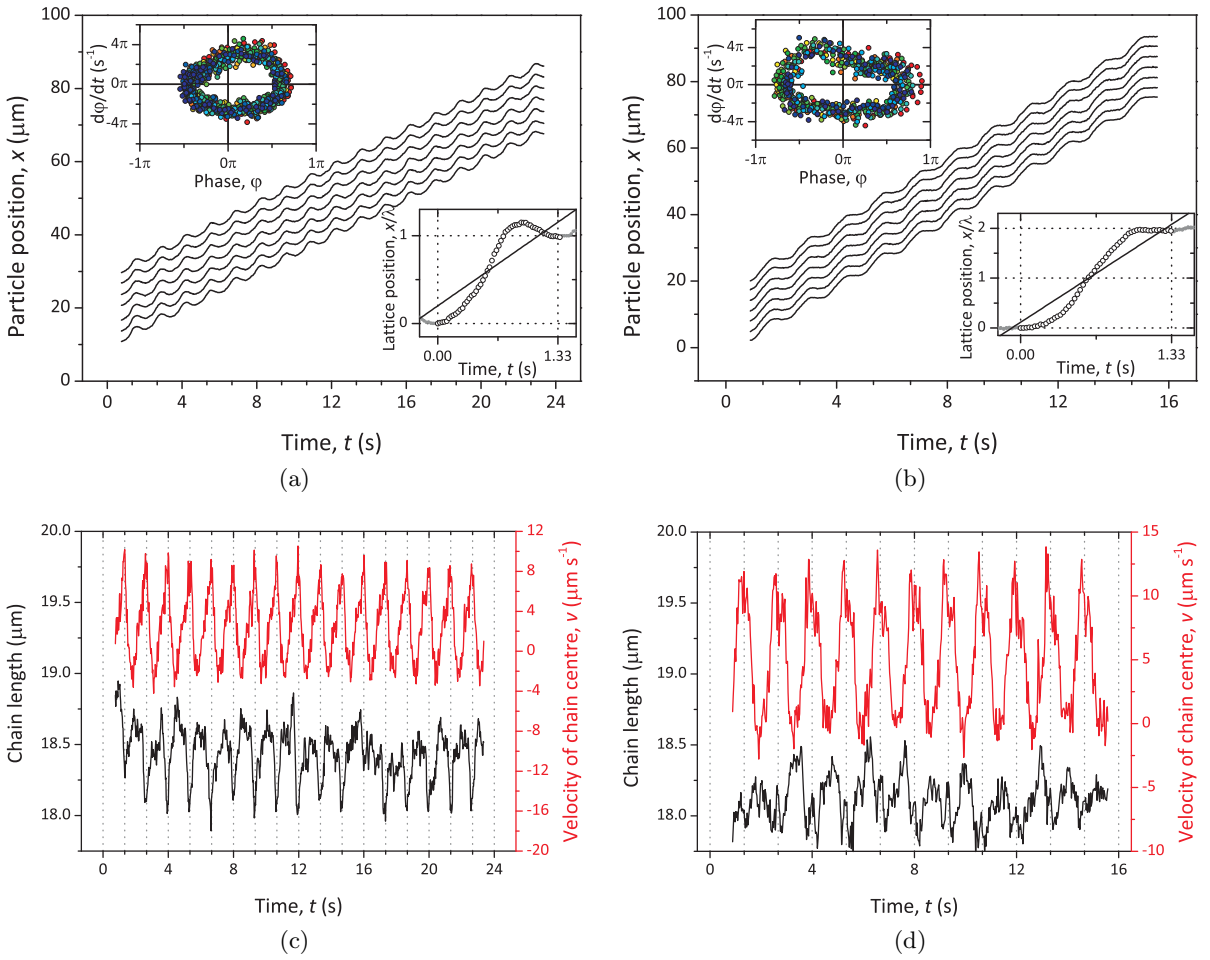


Figure 6.13: Chain of 7 particles in a magnetic field of strength $\Gamma = 15.0 k_B T$ ($B = 0.43$ mT), driven by a stage velocity of: (a,c) $v_{DC} = 2.500$ μm s^{-1}, (b,d) $v_{DC} = 5.233$ μm s^{-1}. (a,b) Trajectories for all 7 chain particles. Top left inset: phase portrait for the chain centre. Bottom right inset: single period of the oscillation of the chain centre. (c,d) Chain length (— bottom), and chain centre velocity (— top).

only the minimum length when the chain is moving at maximum velocity. The fluctuations for the second step (figure 6.13d) are generally slightly smaller, and centred closer to ~ 18 μm, but still clearly correlated to the instantaneous chain centre velocity. This is because at driving velocities far from the critical driving velocity, the particles will feel the pinning of the potentials less strongly.

The fact that the chain is shortest when travelling at a high velocity suggests that motion is driven by the back of the chain, pushing on the front, reminiscent of a breathing mode [7]. Although the measurements presented here cannot resolve the mechanism of this effect, it is likely that the breathing mode is related to a density wave travelling from the back of the chain to the front, allowing the front particles to overcome the potential energy barrier. The stiff chain is more incommensurate, and therefore has lower second critical points, and smaller steps.

The flexible chain experiences higher pinning as a result of its greater commensurability. This correlates with the results in section 6.4.1, where the critical driving velocity (the second critical point of the zeroth step) was found to be higher for lower fields.

6.5 Conclusions

In this chapter, clusters of multiple magnetically coupled colloidal particles have been driven by constant and modulated forces on periodic optical potential energy landscapes. The first aspect of this coupled system probed is the influence of the number of particles and the magnetic field strength on the critical driving velocity under constant drive. Increases in both the number of particles and the magnetic field strength are shown to result in a decrease in the critical driving velocity, due to the increase in the incommensurability of the chain relative to the fixed optical substrate potential, which is reminiscent of the Aubry transition in the Frenkel-Kontorova model. The surprising increase in critical driving velocity found for very small clusters is likely to be a hydrodynamic effect. Secondly, the case of a static chain with the number of particles incommensurate with the number of traps in the landscape is considered. The incommensurability causes the formation of local area of high density, or kink. This kink has been driven using constant and modulated drive, and found to behave as a quasi-particle. The dynamic behaviour, including mode locking, closely resembles that seen for single particles. The third and final system considered is that of a single mobile chain driven by a modulated drive. Clear dynamic mode locking has been observed, and it has been shown that the flexibility in a chain at low magnetic field causes an enhancement of the mode locking effect relative to that seen in a stiff chain at high magnetic field. This causes the mode locked steps to extend over a larger range of driving velocities, which is related to a breathing mode in flexible chains.

Acknowledgements

This work was done in collaboration with Arthur Straube and Dirk Aarts. Alice Thorneywork and Lia Verhoeff are thanked for useful discussions.

Bibliography

[1] H. M. Jaeger and A. J. Liu. Far-from-equilibrium physics: An overview. *arXiv:1009.4874v1*, 2010.

[2] W. Götze. Structural arrest and the dynamics of the liquid glass-transition. *Physica Scripta*, 34(1):66–76, 1986.

[3] M. Marder and J. Fineberg. How things break. *Physics Today*, 49(9):24–29, 1996.

[4] V. L. Popov. *The Prandtl-Tomlinson Model for Dry Friction*. Springer-Verlag, Berlin, 2010.

[5] J. M. Carpinelli, H. H. Weitering, E. W. Plummer, and R. Stumpf. Direct observation of a surface charge density wave. *Nature*, 381(6581):398–400, 1996.

[6] N. Kokubo, R. Besseling, V. M. Vinokur, and P. H. Kes. Mode locking of vortex matter driven through mesoscopic channels. *Physical Review Letters*, 88(24), 2002.

[7] O. M. Braun and Y. S. Kivshar. *The Frenkel-Kontorova Model; Concepts, Methods, and Applications*. Texts and Monographs in Physics. Springer, Berlin, 2010.

[8] M. Gitterman. *The Noisy Pendulum*. World Scientific Publishing, Singapore, 2008.

[9] W. B. Russel, D. A. Saville, and W. R. Schowalter. *Colloidal Dispersions*. Cambridge Monograophs on Mechanics and Applied Mathematics. Cambridge University Press, Cambridge, 1989.

[10] J. B. Perrin. Discontinuous structure of matter, 1926.

[11] A. van Blaaderen, R. Ruel, and P. Wiltzius. Template-directed colloidal crystallization. *Nature*, 385(6614):321–324, 1997.

[12] U. Gasser, E. R. Weeks, A. Schofield, P. N. Pusey, and D. A. Weitz. Real-space imaging of nucleation and growth in colloidal crystallization. *Science*, 292(5515):258–262, 2001.

[13] J. Newman, H. L. Swinney, and L. A. Day. Hydrodynamic properties and structure of fd virus. *Journal of Molecular Biology*, 116(3):593–603, 1977.

[14] S. Sacanna, W. T. M. Irvine, P. M. Chaikin, and D. J. Pine. Lock and key colloids. *Nature*, 464(7288):575–578, 2010.

[15] S. J. Ivell, R. P. A. Dullens, S. Sacanna, and D. G. A. L. Aarts. Emerging structural disorder in a suspension of uniformly dimpled colloidal particles. *Soft Matter*, 9(39):9361–9365, 2013.

[16] C. I. Zoldesi, C. A. van Walree, and A. Imhof. Deformable hollow hybrid silica/siloxane colloids by emulsion templating. *Langmuir*, 22(9):4343–4352, 2006.

[17] L. Rossi, S. Sacanna, W. T. M. Irvine, P. M. Chaikin, D. J. Pine, and A. P. Philipse. Cubic crystals from cubic colloids. *Soft Matter*, 7(9):4139–4142, 2011.

[18] A. Kuijk, A. van Blaaderen, and A. Imhof. Synthesis of monodisperse, rodlike silica colloids with tunable aspect ratio. *Journal of the American Chemical Society*, 133(8):2346–2349, 2011.

[19] H. Shpaisman, D. B. Ruffner, and D. G. Grier. Light-driven three-dimensional rotational motion of dandelion-shaped microparticles. *Applied Physics Letters*, 102(7), 2013.

[20] D. F. Evans and H. Wennerström. *The Colloidal Domain*. Wiley-VCH, USA, 2nd edition, 1999.

[21] R. Brown. A Brief Account of Microscopical Observations, Made in the Months of June, July and August, 1827, on the particles contained in the pollen of plants; and on the general existence of active molecules in organic and inorganic bodies., 1827.

[22] R. J. Hunter. *Foundations of Colloid Science*. Oxford University Press, New York, 2 edition, 2001.

[23] W. Poon. Colloids as big atoms. *Science*, 304(5672):830–831, 2004.

[24] P. N. Pusey and W. van Megen. Phase-behavior of concentrated suspensions of nearly hard colloidal spheres. *Nature*, 320(6060):340–342, 1986.

[25] H. Löwen. Introduction to colloidal dispersions in external fields. *European Physical Journal-Special Topics*, 222(11):2727–2737, 2013.

[26] M. Woerdemann. *Introduction to Optical Trapping*, pages 5–26. Springer-Verlag, Berlin, 2012.

[27] A. Ashkin. Acceleration and trapping of particles by radiation pressure. *Physical Review Letters*, 24:156–159, 1970.

[28] R. Won and A. Ashkin. How it all began. *Nature Photonics*, 5(6):316–317, 2011.

[29] K. C. Neuman and S. M. Block. Optical trapping. *Review of Scientific Instruments*, 75:2787, 2004.

[30] K. Sasaki, M. Koshioka, H. Misawa, N. Kitamura, and H. Masuhara. Pattern-formation and flow-control of fine particles by laser-scanning micromanipulation. *Optics Letters*, 16(19):1463–1465, 1991.

[31] K. Visscher, S. P. Gross, and S. M. Block. Construction of multiple-beam optical traps with nanometer-resolution position sensing. *IEEE Journal of Selected Topics in Quantum Electronics*, 2(4):1066–1076, 1996.

[32] Y. Tanaka, S. Tsutsui, and H. Kitajima. Design of hybrid optical tweezers system for controlled three-dimensional micromanipulation. *Optical Engineering*, 52(4), 2013.

[33] E. R. Dufresne and D. G. Grier. Optical tweezer arrays and optical substrates created with diffractive optics. *Review of Scientific Instruments*, 69(5):1974–1977, 1998.

[34] E. Martin-Badosa, M. Montes-Usategui, A. Carnicer, J. Andilla, E. Pleguezuelos, and I. Juvells. Design strategies for optimizing holographic optical tweezers set-ups. *Journal of Optics A-Pure and Applied Optics*, 9(8):S267–S277, 2007.

[35] T. Bohlein, J. Mikhael, and C. Bechinger. Observation of kinks and antikinks in colloidal monolayers driven across ordered surfaces. *Nature Materials*, 11:126–130, 2012.

[36] K. Dholakia and T. Cizmar. Shaping the future of manipulation. *Nature Photonics*, 5(6):335–342, 2011.

[37] J. Dobnikar, A. Snezhko, and A. Yethiraj. Emergent colloidal dynamics in electromagnetic fields. *Soft Matter*, 9(14):3693–3704, 2013.

[38] A. Jonas and P. Zemanek. Light at work: The use of optical forces for particle manipulation, sorting, and analysis. *Electrophoresis*, 29(24):4813–4851, 2008.

[39] M. J. Padgett and R. Di Leonardo. Holographic optical tweezers and their relevance to lab on chip devices. *Lab on a Chip*, 11:1196–1205, 2011.

[40] J. M. Sancho and A. M. Lacasta. The rich phenomenology of Brownian particles in nonlinear potential landscapes. *The European Physical Journal Special Topics*, 187(1):49–62, 2010.

[41] F. Evers, R. D. L. Hanes, C. Zunke, R. F. Capellmann, J. Bewerunge, C. Dalle-Ferrier, M. C. Jenkins, I. Ladadwa, A. Heuer, R. Castaneda-Priego, and S. U. Egelhaaf. Colloids in light fields: Particle dynamics in random and periodic energy landscapes. *European Physical Journal-Special Topics*, 222(11):2995–3009, 2013.

[42] C. Bechinger, M. Brunner, and P. Leiderer. Phase behavior of two-dimensional colloidal systems in the presence of periodic light fields. *Physical Review Letters*, 86:930–934, 2001.

[43] S. Bleil, H. H. von Grünberg, J. Dobnikar, R. Castaneda-Priego, and C. Bechinger. Strain-induced domain formation in two-dimensional colloidal systems. *Europhysics Letters*, 73(3):450–456, 2006.

[44] T. Bohlein and C. Bechinger. Experimental observation of directional locking and dynamical ordering of colloidal monolayers driven across quasiperiodic substrates. *Physical Review Letters*, 109:058301, 2012.

[45] W. T. M. Irvine, A. D. Hollingsworth, D. G. Grier, and P. M. Chaikin. Dislocation reactions, grain boundaries, and irreversibility in two-dimensional lattices using topological tweezers. *Proceedings of the National Academy of Sciences of the United States of America*, 110(39):15544–15548, 2013.

[46] L. Zaidouny, T. Bohlein, R. Roth, and C. Bechinger. Light-induced phase transitions of colloidal monolayers with crystalline order. *Soft Matter*, 9(38):9230–9236, 2013.

[47] R. R. Brau, J. M. Ferrer, H. Lee, C. E. Castro, B. K. Tam, P. B. Tarsa, P. Matsudaira, M. C. Boyce, R. D. Kamm, and M. J. Lang. Passive and active microrheology with optical tweezers. *Journal of Optics A: Pure and Applied Optics*, 9:S103–S112, 2007.

[48] M. Tassieri, G. M. Gibson, R. M. L. Evans, A. M. Yao, R. Warren, M. J. Padgett, and J. M. Cooper. Measuring storage and loss moduli using optical tweezers: Broadband microrheology. *Physical Review E*, 81:026308, 2012.

[49] P. T. Korda, M. B. Taylor, and D. G. Grier. Kinetically locked-in colloidal transport in an array of optical tweezers. *Physical Review Letters*, 89:128301, 2002.

[50] K. Ladavac, K. Kasza, and D. G. Grier. Sorting mesoscopic objects with periodic potential landscapes: Optical fractionation. *Physical Review E*, 70:010901, 2004.

[51] M. P. MacDonald, G. C. Spalding, and K. Dholakia. Microfluidic sorting in an optical lattice. *Nature*, 426:421–424, 2003.

[52] G. Milne, D. Rhodes, M. MacDonald, and K. Dholakia. Fractionation of polydisperse colloid with acousto-optical generated potential energy landscapes. *Optics Letters*, 32:1144–1146, 2000.

[53] Y. Roichman, V. Wong, and D. G. Grier. Colloidal transport through optical tweezer arrays. *Physical Review E*, 75(1), 2007.

[54] K. Xiao and D.G. Grier. Sorting colloidal particles into multiple channels with optical forces: Prismatic optical fractionation. *Physical Review E*, 82:051407, 2010.

[55] E. M. Furst and A. P. Gast. Micromechanics of dipolar chains using optical tweezers. *Physical Review Letters*, 82(20):4130–4133, 1999.

[56] N. Kiesel, F. Blaser, U. Delic, D. Grass, R. Kaltenbaek, and M. Aspelmeyer. Cavity cooling of an optically levitated submicron particle. *Proceedings of the National Academy of Sciences of the United States of America*, 110(35):14180–14185, 2013.

[57] I. A. Martinez, E. Roldan, J. M. R. Parrondo, and D. Petrov. Effective heating to several thousand kelvins of an optically trapped sphere in a liquid. *Physical Review E*, 87(3), 2013.

[58] D. B. Phillips, G. M. Gibson, R. Bowman, M. J. Padgett, S. Hanna, D. M. Carberry, M. J. Miles, and S. H. Simpson. An optically actuated surface scanning probe. *Optics Express*, 20(28):29679–29693, 2012.

[59] F. Evers, C. Zunke, R. D. L. Hanes, J. Bewerunge, I. Ladadwa, A. Heuer, and S. U. Egelhaaf. Particle dynamics in two-dimensional random-energy landscapes: Experiments and simulations. *Physical Review E*, 88(2), 2013.

[60] R. D. L. Hanes, C. Dalle-Ferier, M. Schmiedeberg, M. C. Jenkins, and S.U. Egelhaaf. Colloids in one dimensional random energy landscapes. *Soft Matter*, 8:2714–2723, 2012.

[61] J. K. G. Dhont. *An Introduction to Dynamics of Colloids*, volume II of *Studies in Interface Science*. Elsevier, Amsterdam, 1996.

[62] K. A. Dill, S. Bromberg, and D. Stigter. *Molecular Driving Forces*. Garland Science, New York, 2002.

[63] K. H. Lan, N. Ostrowsky, and D. Sornette. Brownian dynamics close to a wall studied by photon-correlation spectroscopy from an evanescent wave. *Physical Review Letters*, 57(1):17–20, 1986.

[64] J. Happel and H. Brenner. *Low Reynolds Number Hydrodynamics*. Kluwer Academic Publishers, Dordrecht, The Netherlands, 1983.

[65] J. Leach, H. Mushfique, S. Keen, R. Di Leonardo, G. Ruocco, J. M. Cooper, and M. J. Padgett. Comparison of faxns correction for a microsphere translating or rotating near a surface. *Physical Review E*, 79:026301, 2009.

[66] H. M. Lindsay and P. M. Chaikin. Elastic properties of colloidal crystals and glasses. *Journal of Chemical Physics*, 76(7):3774–3781, 1982.

[67] H. M. Lindsay and P. M. Chaikin. Shear elasticity and viscosity in colloidal crystals and liquids. *Journal De Physique*, 46(C3):269–280, 1985.

[68] D. A. Weitz, W. D. Dozier, and P. M. Chaikin. Periodic structures in driven colloidal crystals. *Journal De Physique*, 46(C3):257–268, 1985.

[69] J. M. di Meglio, D. A. Weitz, and P. M. Chaikin. Competition between shear-melting and Taylor instabilities in colloidal crystals. *Physical Review Letters*, 58(2):136–139, 1987.

[70] J. Zhao, P. Papadopoulos, M. Roth, C. Dobbrow, E. Roeben, A. Schmidt, H. J. Butt, G. Auernhammer, and D. Vollmer. Colloids in external electric and magnetic fields: Colloidal crystals, pinning, chain formation, and electrokinetics. *European Physical Journal-Special Topics*, 222(11):2881–2893, 2013.

[71] D. Guu, J. K. G. Dhont, and M. P. Lettinga. Dispersions and mixtures of particles with complex architectures in shear flow. *European Physical Journal-Special Topics*, 222(11):2739–2755, 2013.

[72] T. O. E. Skinner, H. M. Martin, D. G. A. L. Aarts, and R. P. A. Dullens. Frustrated crystallisation and melting in two-dimensional pentagonal confinement. *Soft Matter*, 9(44):10586–10591, 2013.

[73] T. Sanchez, D. T. N. Chen, S. J. DeCamp, M. Heymann, and Z. Dogic. Spontaneous motion in hierarchically assembled active matter. *Nature*, 491(7424):431, 2012.

[74] J. A. Weiss, A. E. Larsen, and D. G. Grier. Interactions, dynamics, and elasticity in charge-stabilized colloidal crystals. *Journal of Chemical Physics*, 109(19):8659–8666, 1998.

[75] D. J. Griffiths. *Introduction to Electrodynamics*. Prentice-Hall, Upper Saddle River, 3rd edition, 1999.

[76] R. Haghgooie and P. S. Doyle. Transition from two-dimensional to three-dimensional behavior in the self-assembly of magnetorheological fluids confined in thin slits. *Physical Review E*, 75(6), 2007.

[77] D. Vossen. *Optical tweezers in concentrated colloidal dispersions*. PhD thesis, Universiteit Utrecht, 2004.

[78] Y. Harada and T. Asakura. Radiation forces on a dielectric sphere in the Rayleigh scattering regime. *Optics Communications*, 124:529–541, 1996.

[79] Dynal(R). Dynabeads, 2005.

[80] I. S. Khattab, F. Bandarkar, M. A. A. Fakhree, and A. Jouyban. Density, viscosity, and surface tension of water+ethanol mixtures from 293 to 323k. *Korean Journal of Chemical Engineering*, 29(6):812–817, 2012.

[81] Invitrogen(TM) Dynal(R). Dynabeads(r) M-270 Carboxylic Acid, 2007.

[82] F. Ebert. *Dynamics and structure of a colloidal glass former in two dimensions*. PhD thesis, Universität Konstanz, 2008.

[83] J. H. E. Promislow, A. P. Gast, and M. Fermigier. Aggregation kinetics of paramagnetic colloidal particles. *Journal of Chemical Physics*, 102(13):5492–5498, 1995.

[84] T. Skinner. *Two-dimensional colloidal systems: grain boundaries and confinement*. PhD thesis, University of Oxford, 2012.

[85] J. C. Crocker and D. G. Grier. Methods of digital video microscopy for colloidal studies. *Journal of Colloid and Interface Science*, 179:198–310, 1996.

[86] E. Weeks. Particle tracking using IDL, http://www.physics.emory.edu/ weeks/idl/.

[87] E. Gnecco, R. Bennewitz, T. Gyalog, Ch. Loppacher, M. Bammerlin, E. Meyer, and H.-J. Güntherodt. Velocity dependence of atomic friction. *Physical Review Letters*, 84:1172–1175, 2000.

[88] K. E. Kürten and C. Krattenthaler. Multistability and multi 2π-kinks in the Frenkel-Kontorova model: an application to arrays of Josephson Junctions. *Int. J. Mod. Phys. B*, 21:2324–2334, 2007.

[89] V. K. Vlasko-Vlasov, A. E. Koshelev, U. Welp, W. Kwok, A. Rydh, G. W. Crabtree, and K. Kadowaki. *Magneto-optical imaging of Josephson vortices in layered superconductors*, chapter Magneto-Optical Imaging, pages 39–46. Springer, 2004.

[90] B. Michel, A. Bernard, A. Bietsch, E. Delamarche, M. Geissler, D. Juncker, H. Kind, J.-P. Renault, H. Rothuizen, H. Schmid, P. Schmidt-Winkel, R. Stutz, and H. Wolf. Printing meets lithography: Soft approaches to high-resolution patterning. *IBM Journal of Research & Development*, 45:697–719, 2001.

[91] D. J. Harris, J. C. Conrad, and J. A. Lewis. Evaporative lithographic patterning of binary colloidal films. *Philosophical Transactions of the Royal Society A*, 367:5157–5165, 2009.

[92] G. Zhang and D. Wang. Colloidal lithography - the art of nanochemical patterning. *Chemistry - An Asian Journal*, 4:236–245, 2009.

[93] A. J. O'Reilly, C. Francis, and N. J. Quitoriano. Gold nanoparticle deposition on Si by destabilising gold colloid with HF. *Journal of Colloid and Interface Science*, 370:46–50, 2012.

[94] X. G. Ma, P. Y. Lai, and P. G. Tong. Colloidal diffusion over a periodic energy landscape. *Soft Matter*, 9(37):8826–8836, 2013.

[95] D. Babic, C. Schmitt, I. Poberaj, and C. Bechinger. Stochastic resonance in colloidal systems. *Europhysics Letters*, 67:158–164, 2004.

[96] C. Schmitt, B. Dybiec, P. Hänggi, and C. Bechinger. Stochastic resonance vs. resonant activation. *Europhysics Letters*, 74:937–943, 2006.

[97] A. Curran, M. P. Lee, R. Di Leonardo, and J. M. Cooper M. J. Padgett. Partial synchronization of stochastic oscillators through hydrodynamic coupleing. *Physical Review Letters*, 108:240601, 2012.

[98] J. Dobnikar, M. Brunner, H. H. von Grünberg, and C. Bechinger. Three-body interactions in colloidal systems. *Physical Review E*, 69:031402, 2004.

[99] A. C. Richardson, S. N. S. Reihani, and L. B. Oddershede. Non-harmonic potential of a single beam optical trap. *Optics Express*, 2008(16):15709–15717, 2008.

[100] T. Godazgar, R. Shokri, and S. N. Reihani. Potential mapping of optical tweezers. *Optics Letters*, 36:3284–3286, 2011.

[101] M. Jahnel, M. Behrndt, A. Jannasch, E. Schäffer, and S. W. Grill. Measuring the complete force field of an optical trap. *Optics Letters*, 36:1260–1262, 2011.

[102] A. V. Arzola, K. Volke-Sepulveda, and J. L. Mateos. Force mapping of an extended light pattern in an inclined plane: Deterministic regime. *Optics Express*, 17(5):3429–3440, 2009.

[103] A. V. Straube, A. A. Louis, J. Baumgartl, C. Bechinger, and R. P. A. Dullens. Pattern formation in colloidal explosions. *Europhysics Letters*, 94:48008, 2011.

[104] A. Rohrbach. Stiffness of optical traps: Quantitative agreement between experiment and electromagnetic theory. *Physical Review Letters*, 95:168102, 2005.

[105] M. P. N. Juniper, R. Besseling, D. G. A. L. Aarts, and R. P. A. Dullens. Acousto-optically generated potential energy landscapes: potential mapping using colloids under flow. *Optics Express*, 27:28707–28716, 2012.

[106] F. Heslot, T. Baumberger, B. Perrin, B. Caroli, and C. Caroli. Creep, stick-slip, and dry-friction dynamics: Experiments and a heuristic model. *Physical Review E*, 49(6):4973–4988, 1994.

[107] P. Talkner, E. Hershkovitz, E. Pollak, and P. Hanggi. Controlling activated surface diffusion by external fields. *Surface Science*, 437(1-2):198–206, 1999.

[108] Matthew B. Pinson, Edith M. Sevick, and David R. M. Williams. Mobile rings on a polyrotaxane lead to a yield force. *Macromolecules*, 46(10):4191–4197, 2013.

[109] B. D. Josephson. Possible new effects in superconductive tunnelling. *Physics Letters*, 1(7):251–253, 1962.

[110] P. W. Anderson and J. M. Rowell. Probable observation of the josephson superconducting tunneling effect. *Physical Review Letters*, 10:230–232, 1963.

[111] A. A. Abrikosov. Nobel lecture: Type-II superconductors and the vortex lattice. *Reviews of Modern Physics*, 76(3):975–979, 2004.

[112] R. Besseling, P. H. Kes, T. Drose, and V. M. Vinokur. Depinning and dynamics of vortices confined in mesoscopic flow channels. *New Journal of Physics*, 7(Feb 25), 2005.

[113] R. Besseling. *Depinning and Dynamics of the Vortex Lattice in Thin Films and Narrow Channels*. PhD thesis, Universiteit Leiden, 2001.

[114] G. Grüner. The dynamics of charge-density waves. *Reviews of Modern Physics*, 60(4):1129–1181, 1988.

[115] L. Ya Vinnikov, J. Karpinski, S. M. Kazakov, J. Jun, J. Anderegg, S. L. Budko, and P. C. Canfield. Vortex structure in MgB_2 single crystals observed by the bitter decoration technique. *Physical Review B*, 67(9):092512, 2003.

[116] A. E. Koshelev and V. M. Vinokur. Dynamic melting of the vortex lattice. *Physical Review Letters*, 73(26):3580–3583, 1994.

[117] C. Reichhardt, C. J. Olson, and F. Nori. Dynamic phases of vortices in superconductors with periodic pinning. *Physical Review Letters*, 78(13):2648–2651, 1997. PRL.

[118] C. J. Olson, C. Reichhardt, and F. Nori. Nonequilibrium dynamic phase diagram for vortex lattices. *Physical Review Letters*, 81(17):3757–3760, 1998. PRL.

[119] A. A. Abrikosov. On the magnetic properties of superconductors of the second group. *Soviet Physics Journal of Experimental and Theoretical Physics - USSR*, 5(6):1174–1183, 1957.

[120] P. Martinoli. Static and dynamic interaction of superconducting vortices with a periodic pinning potential. *Physical Review B*, 17(3):1175–1194, 1978.

[121] V. Gotcheva and S. Teitel. Depinning transition of a two-dimensional vortex lattice in a commensurate periodic potential. *Physical Review Letters*, 86(10):2126–2129, 2001.

[122] K. Harada, T. Matsuda, J. Bonevich, M. Igarashi, S. Kondo, G. Pozzi, U. Kawabe, and A. Tonomura. Real-time observation of vortex lattices in a superconductor by electron-microscopy. *Nature*, 360(6399):51–53, 1992.

[123] C. Reichhardt and C. J. O. Reichhardt. Crossover from intermittent to continuum dynamics for locally driven colloids. *Physical Review Letters*, 96(2), 2006.

[124] V. Blickle, T. Speck, C. Lutz, U. Seifert, and C. Bechinger. Einstein relation generalized to nonequilibrium. *Physical Review Letters*, 98(21), 2007.

[125] A. I. Shushin. External force affected escape of Brownian particles from a potential well. *Journal of Physical Chemistry A*, 113(32):9065–9074, 2009.

[126] P. Reimann, C. Van den Broeck, H. Linke, P. Hnggi, J. M. Rubi, and A. Prez-Madrid. Diffusion in tilted periodic potentials: Enhancement, universality, and scaling. *Physical Review E*, 65(3):031104, 2002.

[127] M. Siler and P. Zemanek. Particle jumps between optical traps in a one-dimensional (1d) optical lattice. *New Journal of Physics*, 12, 2010.

[128] C. Dalle-Ferrier, M. Kruger, R. D. L. Hanes, S. Walta, M. C. Jenkins, and S. U. Egelhaaf. Dynamics of dilute colloidal suspensions in modulated potentials. *Soft Matter*, 7(5):2064–2075, 2011.

[129] G. Costantini and F. Marchesoni. Threshold diffusion in a tilted washboard potential. *Europhysics Letters*, 48(5):491–497, 1999.

[130] K. Lindenberg, A. M. Lacasta, J. M. Sancho, and A. H. Romero. Transport and diffusion on crystalline surfaces under external forces. *New Journal of Physics*, 7, 2005.

[131] M. Evstigneev, O. Zvyagolskaya, S. Bleil, R. Eichhorn, C. Bechinger, and P. Reimann. Diffusion of colloidal particles in a tilted periodic potential: Theory versus experiment. *Physical Review E*, 77(4), 2008.

[132] S. H. Lee and D. G. Grier. Giant colloidal diffusivity on corrugated optical vortices. *Physical Review Letters*, 96(19), 2006.

[133] P. Reimann, C. Van den Broeck, H. Linke, P. Hanggi, J. M. Rubi, and A. Perez-Madrid. Giant acceleration of free diffusion by use of tilted periodic potentials. *Physical Review Letters*, 87(1), 2001.

[134] A. V. Straube. Dynamics of driven colloids in optically created landscapes. Personal communication, 2014.

[135] H. A. Kramers. Brownian motion in a field of force and the diffusion model of chemical reactions. *Physica*, 7(4):284, 1940.

[136] E. Hershkovitz, P. Talkner, E. Pollak, and Y. Georgievskii. Multiple hops in multidimensional activated surface diffusion. *Surface Science*, 421(1-2):73–88, 1999.

[137] A. Pikovsky, M. Rosenblum, and J. Kurths. *Synchronization A universal concept in Nonlinear Sciences*. Cambridge Nonlinear Science Series. Cambridge University Press, Cambridge, 2001.

[138] T. Birch. *The history of the Royal Society of London*. 1756.

[139] M. Bennett, M. F. Schatz, H. Rockwood, and K. Wiesenfeld. Huygens's clocks. *Proceedings of the Royal Society A-Mathematical Physical and Engineering Sciences*, 458(2019):563–579, 2002.

[140] Deepak K. Agrawal, Jim Woodhouse, and Ashwin A. Seshia. Observation of locked phase dynamics and enhanced frequency stability in synchronized micromechanical oscillators. *Physical Review Letters*, 111(8):084101, 2013.

[141] L. Fredrickson-Hemsing, S. Ji, R. Bruinsma, and D. Bozovic. Mode-locking dynamics of hair cells of the inner ear. *Physical Review E*, 86(2), 2012.

[142] Z. Neda, E. Ravasz, Y. Brechet, T. Vicsek, and A. L. Barabasi. The sound of many hands clapping - tumultuous applause can transform itself into waves of synchronized clapping. *Nature*, 403(6772):849–850, 2000.

[143] Z. Neda, E. Ravasz, T. Vicsek, Y. Brechet, and A. L. Barabasi. Physics of the rhythmic applause. *Physical Review E*, 61(6):6987–6992, 2000.

[144] S. C. Nicolis, J. Fernndez, C. Prez-Penichet, C. Noda, F. Tejera, O. Ramos, D. J. T. Sumpter, and E. Altshuler. Foraging at the edge of chaos: Internal clock versus external forcing. *Physical Review Letters*, 110(26):268104, 2013.

[145] X. L. Feng, C. J. White, A. Hajimiri, and M. L. Roukes. A self-sustaining ultrahigh-frequency nanoelectromechanical oscillator. *Nature Nanotechnology*, 3(6):342–346, 2008.

[146] D. Antonio, D. H. Zanette, and D. Lopez. Frequency stabilization in nonlinear micromechanical oscillators. *Nature Communications*, 3, 2012.

[147] S. B. Shim, M. Imboden, and P. Mohanty. Synchronized oscillation in coupled nanomechanical oscillators. *Science*, 316(5821):95–99, 2007.

[148] M. Zalalutdinov, K. L. Aubin, M. Pandey, A. T. Zehnder, R. H. Rand, H. G. Craighead, J. M. Parpia, and B. H. Houston. Frequency entrainment for micromechanical oscillator. *Applied Physics Letters*, 83(16):3281–3283, 2003.

[149] M. A. Zhang, G. S. Wiederhecker, S. Manipatruni, A. Barnard, P. McEuen, and M. Lipson. Synchronization of micromechanical oscillators using light. *Physical Review Letters*, 109(23), 2012.

[150] N. Kokubo, R. Besseling, and P. H. Kes. Dynamic ordering and frustration of confined vortex rows studied by mode-locking experiments. *Physical Review B*, 69(6), 2004.

[151] A. B. Kolton, D. Dominguez, and N. Gronbech-Jensen. Mode locking in AC-driven vortex lattices with random pinning. *Physical Review Letters*, 86(18):4112–4115, 2001.

[152] I. V. Grigorieva. Magnetic-flux decoration of type-II superconductors. *Superconductor Science & Technology*, 7(4):161–176, 1994.

[153] M. Kvale and S. E. Hebboul. Theory of Shapiro steps in Josephson-Junction arrays and their topology. *Physical Review B*, 43(4):3720–3723, 1991.

[154] S. E. Burkov. Magnetization curves for thin-films of layered type-II superconductors, Kolmogorov-Arnold-Moser theory, and the devils staircase. *Physical Review B*, 44(6):2850–2852, 1991.

[155] C. C. Grimes and S. Shapiro. Millimeter-wave mixing with Josephson Junctions. *Physical Review*, 169(2):397, 1968.

[156] S. Aubry. *The New Concept of Transitions by Breaking of Analyticity in a Crystallographic Model*, pages 264–277. Springer Series in Solid-State Sciences. Springer-Verlag, Berlin, 1978.

[157] N. W. Ashcroft and N. D. Mermin. *Solid State Physics*. Thomson Learning, USA, 1976.

[158] M. Eichberger, H. Schafer, M. Krumova, M. Beyer, J. Demsar, H. Berger, G. Moriena, G. Sciaini, and R. J. D. Miller. Snapshots of cooperative atomic motions in the optical suppression of charge density waves. *Nature*, 468(7325):799–802, 2010.

[159] A. Simon and A. Libchaber. Escape and synchronisation of a Brownian particle. *Physical Review Letters*, 68(23):3375–3378, 1992.

[160] D. Hennig, A. D. Burbanks, and A. H. Osbaldestin. Directing particle transport in a two-dimensional periodic potential landscape. *Chemical Physics*, 375(2-3):492–502, 2010.

[161] J. Hasnain, S. Jungblut, and C. Dellago. Dynamic phases of colloidal monolayers sliding on commensurate substrates. *Soft Matter*, 9(25):5867–5873, 2013.

[162] D. McDermott, J. Amelang, L. M. Lopatina, C. J. O. Reichhardt, and C. Reichhardt. Domain and stripe formation between hexagonal and square ordered fillings of colloidal particles on periodic pinning substrates. *Soft Matter*, 9(18):4607–4613, 2013.

[163] C. L. Wang, J. Tekic, W. S. Duan, Z. G. Shao, and L. Yang. Ratchet effect and amplitude dependence of phase locking in a two-dimensional Frenkel-Kontorova model. *Journal of Chemical Physics*, 138(3), 2013.

[164] M. Pelton, K. Ladavac, and D. G. Grier. Transport and fractionation in periodic potential-energy landscapes. *Physical Review E*, 70(3), 2004.

[165] N. Shi and V. M. Ugaz. Entropic stochastic resonance enables trapping under periodic confinement: A Brownian-dynamics study. *Physical Review E*, 89:012138, 2014.

[166] D. Reguera, P. Reimann, P. Hanggi, and J. M. Rubi. Interplay of frequency-synchronization with noise: Current resonances, giant diffusion and diffusion-crests. *Europhysics Letters*, 57(5):644–650, 2002.

[167] J. Tekic and B. Hu. Noise-induced Bessel-like oscillations of Shapiro steps with the period of the AC force. *Physical Review B*, 78(10), 2008.

[168] Alejandro V. Arzola, Karen Volke-Seplveda, and Jos L. Mateos. Dynamical analysis of an optical rocking ratchet: Theory and experiment. *Physical Review E*, 87(6):062910, 2013.

[169] S. Herrera-Velarde and R. Castaneda-Priego. Superparamagnetic colloids confined in narrow corrugated substrates. *Physical Review E*, 77(4), 2008.

[170] K. Lichtner, A. Pototsky, and S. H. L. Klapp. Feedback-induced oscillations in one-dimensional colloidal transport. *Physical Review E*, 86(5), 2012.

[171] J. X. Chen and Z. K. Jiao. Mode-locking behaviour in driven colloids with random pinning. *Chinese Physics Letters*, 24(4):1095–1098, 2007.

[172] A. V. Straube and P. Tierno. Synchronous vs. asynchronous transport of a paramagnetic particle in a modulated ratchet potential. *Europhysics Letters*, 103(2):28001, 2013.

[173] J. C. Cotteverte, F. Bretenaker, and A. Lefloch. Vectorial nonlinear dynamics in lasers with one or 2 stable eigenstates. *Physical Review A*, 49(4):2868–2880, 1994.

[174] W. W. Chow, J. Geabanacloche, L. M. Pedrotti, V. E. Sanders, W. Schleich, and M. O. Scully. The ring laser gyro. *Reviews of Modern Physics*, 57(1):61–104, 1985.

[175] C. Reichhardt, R. T. Scalettar, G. T. Zimanyi, and N. Gronbech-Jensen. Shapiro steps in driven vortex lattices interacting with periodic pinning arrays. *Physica C*, 332(1-4):1–4, 2000.

[176] A. V. Straube. High frequencies: some notes concerning the approximation. Personal communication, 2014.

[177] B. Hu and J. Tekic. Amplitude and frequency dependence of the Shapiro steps in the DC- and AC-driven overdamped Frenkel-Kontorova model. *Physical Review E*, 75(5), 2007.

[178] F. C. Frank and J. H. Vandermerwe. One-dimensional dislocations 1: Static theory. *Proceedings of the Royal Society of London Series a-Mathematical and Physical Sciences*, 198(1053):205–216, 1949.

[179] A. G. Naumovets. Collective surface diffusion: An experimentalist's view. *Physica a-Statistical Mechanics and Its Applications*, 357(2):189–215, 2005.

[180] S. C. Ying. Structure and dynamics of a submonolayer film adsorbed on solid surfaces. *Physical Review B*, 3(12):4160, 1971.

[181] J. V. Barth. Transport of adsorbates at metal surfaces: From thermal migration to hot precursors. *Surface Science Reports*, 40(3-5):75–149, 2000.

[182] A. Vanossi and O. M. Braun. Driven dynamics of simplified tribological models. *Journal of Physics-Condensed Matter*, 19(30), 2007.

[183] M. D. Chinn and S. C. Fain. Structural phase-transition in epitaxial solid krypton monolayers on graphite. *Physical Review Letters*, 39(3):146–149, 1977.

[184] A. Guinier and P. Jacquet. Striated structure of age-hardened alloys. *Nature*, 155(3945):695–695, 1945.

[185] I. M. Tolic-Norrelykke, E. L. Munteanu, G. Thon, L. Oddershede, and K. Berg-Sorensen. Anomalous diffusion in living yeast cells. *Physical Review Letters*, 93(7), 2004.

[186] A. Benassi, A. Vanossi, and E. Tosatti. Nanofriction in cold ion traps. *Nature Communications*, 2, 2011.

[187] A. Vanossi, N. Manini, and E. Tosatti. Static and dynamic friction in sliding colloidal monolayers. *Proceedings of the National Academy of Sciences of the United States of America*, 109(41):16429–16433, 2012.

[188] V. L. Popov and J. A. T. Gray. Prandtl-Tomlinson model: History and applications in friction, plasticity, and nanotechnologies. *Zamm-Journal of Applied Mathematics and Mechanics*, 92(9):683–708, 2012.

[189] M. Larcher, M. Modugno, and F. Dalfovo. Localization in momentum space of ultracold atoms in incommensurate lattices. *Physical Review A*, 83(1), 2011.

[190] F. Falo, L. M. Floria, P. J. Martinez, and J. J. Mazo. Unlocking mechanism in the AC dynamics of the Frenkel-Kontorova model. *Physical Review B*, 48(10):7434–7437, 1993.

[191] L. M. Floria and J. J. Mazo. Dissipative dynamics of the Frenkel-Kontorova model. *Advances in Physics*, 45(6):505–598, 1996.

[192] O. M. Braun and Y. S. Kivshar. Nonlinear dynamics of the Frenkel-Kontorova model. *Physics Reports-Review Section of Physics Letters*, 306(1-2):1–108, 1998.

[193] J. Tekic, D. D. He, and B. B. Hu. Noise effects in the AC-driven Frenkel-Kontorova model. *Physical Review E*, 79(3), 2009.

[194] J. Tekic and B. Hu. Properties of the Shapiro steps in the AC driven Frenkel-Kontorova model with deformable substrate potential. *Physical Review E*, 81(3), 2010.

[195] X. Y. Gao, X. R. Hong, C. L. Wang, and W. S. Duan. The dynamic characters of excitations in a one-dimensional Frenkel-Kontorova model. *Chinese Physics B*, 17(9):3378–3386, 2008.

[196] S. Stoyanov and H. Mullerkrumbhaar. Resonance-induced cluster-mobility - dynamics of a finite Frenkel-Kontorova model. *Surface Science*, 159(1):49–68, 1985.

[197] M. M. Lin, W. S. Duan, and J. M. Chen. Friction phenomena in a two-dimensional Frenkel-Kontorova model. *Chinese Physics B*, 19(2), 2010.

[198] M. M. Lin. The effect of AC-driven force on superlubricity in a two-dimensional Frenkel-Kontorova model. *Physica Scripta*, 82(2), 2010.

[199] S. R. Sharma and B. Bergersen. Aubry transition in a finite modulated chain. *Physical Review B*, 29(11):6335–6340, 1984.

[200] R. Besseling, N. Kokubo, and P. H. Kes. Dynamic melting of confined vortex matter. *Physical Review Letters*, 91(17), 2003.

[201] C. Reichhardt and C. J. O. Reichhardt. Cooperative behavior and pattern formation in mixtures of driven and nondriven colloidal assemblies. *Physical Review E*, 74(1), 2006.

[202] S. Herrera-Velarde and R. Castaneda-Priego. Structure and dynamics of interacting Brownian particles in one-dimensional periodic substrates. *Journal of Physics-Condensed Matter*, 19(22), 2007.

[203] D. Hennig, A. D. Burbanks, and A. H. Osbaldestin. Directed transport of two interacting particles in a washboard potential. *Physica D-Nonlinear Phenomena*, 238(23-24):2273–2281, 2009.

[204] Pietro Tierno, Tom H. Johansen, and J. M. Sancho. Unconventional dynamic hysteresis in a periodic assembly of paramagnetic colloids. *Physical Review E*, 87(6):062301, 2013.

[205] D. Hennig, C. Mulhern, A. D. Burbanks, and L. Schimansky-Geier. Nonlinear response of a linear chain to weak driving. *Physical Review E*, 89:012906, 2014.

[206] D. Speer, R. Eichhorn, M. Evstigneev, and P. Reimann. Dimer motion on a periodic substrate: Spontaneous symmetry breaking and absolute negative mobility. *Physical Review E*, 85(6), 2012.

[207] A. Libal, B. M. Csiki, C. J. O. Reichhardt, and C. Reichhardt. Colloidal lattice shearing and rupturing with a driven line of particles. *Physical Review E*, 87(2), 2013.

[208] L. Gao, M. A. Tahir, L. N. Virgin, and B. B. Yellen. Multiplexing superparamagnetic beads driven by multi-frequency ratchets. *Lab on a Chip*, 11(24):4214–4220, 2011.

[209] P. Tierno. Depinning and collective dynamics of magnetically driven colloidal monolayers. *Physical Review Letters*, 109(19), 2012.

[210] J. T. Padding and A. A. Louis. Hydrodynamic interactions and Brownian forces in colloidal suspensions: Coarse-graining over time and length scales. *Physical Review E*, 74(3), 2006.

[211] N. D. Mermin. Topological theory of defects in ordered media. *Reviews of Modern Physics*, 51(3):591–648, 1979.

[212] A. Kwasniewski, P. Machnikowski, and P. Magnuszewski. Kink dynamics in finite discrete sine-Gordon chains. *Physical Review E*, 59(2):2347–2354, 1999.

List of publications

To date the following publications based on work in this thesis have been submitted or are in preparation:

Michael P. N. Juniper, Rut Besseling, Dirk G. A. L. Aarts, and Roel P. A. Dullens. *Acousto-optically generated potential energy landscapes: potential mapping using colloids under flow*, Optics Express, **20**, 28707-28716 (2012) (Chapter 3)

Michael P. N. Juniper, Arthur V. Straube, Dirk G. A. L. Aarts, and Roel P. A. Dullens. *Depinning transition of finite coupled colloidal systems in potential energy landscapes*, In preparation (Chapters 4 & 6)

Michael P. N. Juniper, Arthur V. Straube, Rut Besseling, Dirk G. A. L. Aarts, and Roel P. A. Dullens. *Imaging the microscopic dynamics of synchronisation using driven colloids*, In preparation (Chapters 5 & 6)

Michael P. N. Juniper, Arthur V. Straube, Urs Zimmermann, Rut Besseling, Dirk G. A. L. Aarts, Hartmut Löwen, and Roel P. A. Dullens. *Dynamic mode locking in a driven colloidal system: Experiments, theory, and simulations*, In preparation (Chapters 4, 5 & 6)

Acknowledgements

Roel, I do not know what to say. "Thank you" hardly seems adequate. You gave me the opportunity that nobody else would have given to me, and you believed in me when I did not believe in myself. Your tireless enthusiasm for science has kept me going. I hope that over the past years I have repaid you for your faith; we've done some good science.

I must extend my sincere thanks to Arthur, for not only having power over maths, but also for being able to patiently explain it to me. Also to Rut, without whom I would never have had the excitement of seeing the Shapiro Steps for the first time, and to Dirk, who is always interested in whatever science is going on.

I am incredibly grateful to all of the denizens of 13-07 for putting up with the sarcasm, rants, and ever-increasing jungle. I especially thank Tom, for showing me how everything worked, letting me make my own mistakes (and then fixing them for me), and demonstrating that a filing cabinet can make an excellent wardrobe. Lia and Arran, with whom I have shared the lab of late, deserve my grateful appreciation for all of their assistance, and for tolerating my intolerance of vibrations, temperatures $T \neq 298$ K, and disordered Allen keys.

The Dullens/Aarts conurbation have made this a rich environment in which to work. Liz (who showed me how things worked at the Beginning), Paola (who has tried all of the other desks in the time I have been sitting at this one), Oli (for whom the journey IS the destination), and Julia (who has an exquisitely tuned cake-radar) deserve particular mention.

Special thanks go to Alice, my cake-baking, coffee-drinking co-conspirator, confidante, and feminist collaborator. Congratulations, on being the first person, to reach the end, of this (T/t)hesis. We will make Science Work, right?

Sam, it's been a long road since we first considered the ethics of cannibalism. Thank you for 7.5 years, 8 chemistry dinners, innumerable explanations of quantum mechanics, and organic writing Blissters... and that was before the science even really started. We got here in the end.

I am eternally grateful to my mother, for making me into a scientist, and to my father for his endless support, sympathy, and messages about cricket. Finally, I would like to thank Hannah, without whom this thesis would not have been completed. For the wake-up calls, the weekend walks, the tireless encouragement, and for asking different questions to everybody else.